



Universidade Estadual de Campinas

Instituto de Física Gleb Wataghin (IFGW)

Vladimir Roger Miranda La Hera

Optical Properties of Wurtzite Phase
InAsP/InP Heterostructure Nanowires

Propriedades ópticas de Nanofios de InAsP/InP
heteroestruturados na fase Wurtzita

Campinas

2015

Vladimir Roger Miranda La Hera

Optical Properties of Wurtzite Phase InAsP/InP Heterostructure Nanowires

Propriedades ópticas de Nanofios de InAsP/InP heteroestruturados na fase Wurtzita

Dissertação apresentada ao
Instituto de Física "Gleb Wataghin"
da Universidade Estadual de
Campinas como parte dos
requisitos exigidos para a obtenção
do título de Mestre em Física.

Supervisor: Prof. Fernando Iikawa

Co-supervisor: Prof. Odilon Divino Damasceno Couto Jr.


Fernando Iikawa

ESTE EXEMPLAR CORRESPONDE À VERSÃO
FINAL DE DISSERTAÇÃO DEFENDIDA PELO
ALUNO VLADIMIR ROGER MIRANDA LA
HERA, E ORIENTADA PELO PROF. DR.
FERNANDO IIKAWA

Campinas

2015

Agência(s) de fomento e nº(s) de processo(s): CAPES, 1247651/2013

Ficha catalográfica
Universidade Estadual de Campinas
Biblioteca do Instituto de Física Gleb Wataghin
Lucimeire de Oliveira Silva da Rocha - CRB 8/9174

M672o Miranda La Hera, Vladimir Roger, 1988-
Optical properties of wurzite phase InAsP/InP heterostructure nanowires /
Vladimir Roger Miranda La Hera. – Campinas, SP : [s.n.], 2015.

Orientador: Fernando Iikawa.
Coorientador: Odilon Divino Damasceno Couto Junior.
Dissertação (mestrado) – Universidade Estadual de Campinas, Instituto de Física Gleb Wataghin.

1. Nanofios semicondutores. 2. Heteroestruturas - Propriedades óticas. 3. Semicondutores - Propriedades óticas. 4. Materiais nanoestruturados. I. Iikawa, Fernando, 1960-. II. Couto Junior, Odilon Divino Damasceno, 1979-. III. Universidade Estadual de Campinas. Instituto de Física Gleb Wataghin. IV. Título.

Informações para Biblioteca Digital

Título em outro idioma: Propriedades óticas de nanofios de InAsP/InP heteroestruturados na fase wurzita

Palavras-chave em inglês:

Semiconductors nanowires
Heterostructures - Optical properties
Semiconductors - Optical properties
Nanostructured materials

Área de concentração: Física

Titulação: Mestre em Física

Banca examinadora:

Fernando Iikawa [Orientador]
Evaldo Ribeiro

Kleber Roberto Pirola

Data de defesa: 17-12-2015

Programa de Pós-Graduação: Física



MEMBROS DA COMISSÃO JULGADORA DA DISSERTAÇÃO DE MESTRADO DE **VLADIMIR ROGER MIRANDA LA HERA - RA 151599** APRESENTADA E APROVADA AO INSTITUTO DE FÍSICA “GLEB WATAGHIN”, DA UNIVERSIDADE ESTADUAL DE CAMPINAS, EM 17 / 12 / 2015.

COMISSÃO JULGADORA:

- Prof. Dr. Fernando Iikawa – Orientador - DFMC/IFGW/UNICAMP
- Prof. Dr. Evaldo Ribeiro – DF/UFPR
- Prof. Dr. Kleber Roberto Pirota – DFMC/IFGW/UNICAMP

OBS.: Informo que as assinaturas dos respectivos professores membros da banca constam na ata de defesa já juntada no processo vida acadêmica do aluno.

CAMPINAS
2015

Acknowledgments

Prof. Fernando Iikawa, thank for the patient guidance, useful advices and dedication time, opportunity and orientation on me in this journey.

Prof. Odilon Couto, for the optical measurements, supervising the development of this research and the countless useful discussions with valuable and constructive suggestions.

Prof. Mônica A. Cotta and her PhD student **Douglas S. Oliveira**, and **Helio Obata**, for the growth and supply of samples. Apart from the growth parameter discussion.

Prof. Luiz F. Zagonel and his Master student **Bruno Cesar**, for the electron microscopy analysis of our samples and the discussion of the results. LNNano for the TEM and SEM measurements.

Milton Tanabe, for the technical support and help in several experimental details.

All group colleagues, Miguel, Rodrigo, and Angela, for the friendship and help in the optical measurements.

Coordination for the Improvement of Higher Education Personnel (**Capes**), for the financial support.

Cryogenic sector of the Physics Institute for the liquid nitrogen and helium supply.

Family and friends, who always are helping and supporting me in each step I make, you are always in mi mind.

Abstract

In this work, we studied the optical properties of wurtzite phase InAsP alloy nanowires (NWs) and InAsP/InP heterostructure nanowires grown by Vapor-Liquid-Solid (VLS) method in a Chemical Beam Epitaxy (CBE) system. The optical measurements were carried out by photoluminescence spectroscopy in ensemble and single NWs by macro and micro-photoluminescence techniques. The interest for InAsP alloys is that they present gap energy in the near infra-red, a spectral range commonly used for the telecommunication technology as well as for harmful carbon compounds detection sensors, since their optical absorption is in the same energy range. Furthermore, the InAsP in nanoscale structures, in particular, in NWs, in addition to the stable cubic phase, which occurs in all other phosphide and arsenide III-V compounds, hexagonal wurtzite phase is also observed. Most of the properties of their wurtzite structure has not been investigated in details yet. The heterostructure NWs containing InAsP and InP in wurtzite phase are not deeply known as well. The main purpose of this dissertation is, therefore, to investigate the optical properties of this compounds in NW forms, which present wurtzite phase, and to study the optical emission from the heterostructures, where the quantum confinement effect can also be used to tune the emission wavelength. We investigated InAsP alloy NWs with three compositions changing the arsine and phosphine flux and they are grown using three sizes of *Au*-nanoparticle (*Au*-NP) catalyst, 2, 5 and 20 nm. We note that the NW shape depends on the *Au*-NP size. For small size, a tower-like shape was observed, while for large one, the needle-like one. The *P* content of the samples is around the 50 % estimated by the photoluminescence and by Energy-Dispersive X-ray spectroscopy. The optical emission is around 1.5 μm , appropriate for telecommunication device applications. For InAsP/InP heterostructure NWs, we investigated samples with different InAsP time deposition (2, 5, 10, 20 and 40 s) onto the InP and they were grown with different *Au*-NP size (2, 5 and 20 nm) used as catalyst. In these samples, all nanowires present needle-like shape. The macro and micro-photoluminescence spectra show strong optical emissions in 800-1000 nm range attributed to the InAsP layer emissions. The emission energy depends on the amount of InAsP according to the quantum confinement effect. We observed several sharp lines in the micro-photoluminescence spectra of single NWs attributed to the localized states of the InAsP layers. They come from two regions, one of them from the axial catalyst InAsP layer and second one, from the lateral InAsP epitaxial growth layer. The result shows that the InAsP/InP heterostructures NWs grown by VLS method in the CBE system present high crystal quality and are promising structure for optical device applications.

Resumo

Neste trabalho foram estudadas as propriedades ópticas de nanofios (NWs) semicondutores InAsP/InP na fase Wurtzita, crescidos pelo método *Vapor-Liquid-Solid* (VLS) no sistema *Chemical Beam Epitaxy* (CBE). As medidas ópticas foram realizadas por espectroscopia de fotoluminescência em *ensembles* e nanofios individuais, por macro e micro-fotoluminescência. O interesse pelas ligas de InAsP é que elas apresentam energia do *gap* na faixa de infravermelho próximo, uma faixa espectral utilizada para a tecnologia de telecomunicações bem como em fabricação de detetores de compostos de carbono nocivos, pois eles apresentam absorção óptica nessa mesma faixa. Além disso, InAsP na forma de estruturas na escala nanométrica, em particular, em NWs, além de ter a fase cúbica estável, que ocorre em todos os fosfetos e arsenetos de compostos III-V, a fase hexagonal wurtzita é também observada. A maioria de suas propriedades na estrutura wurtzita ainda não foi investigada em detalhes. Os nanofios heteroestruturados contendo InAsP e InP na fase wurtzita não são bem conhecidos também. O ponto principal desta tese é, portanto, investigar as propriedades ópticas desses compostos na forma de nanofios, que estão na fase wurtzita, e estudar a emissão óptica destas heteroestruturas, onde envolve o efeito de confinamento quântico, o qual pode ser utilizado para sintonizar o comprimento de onda da emissão. Investigamos NWs de ligas de InAsP com três composições diferentes, mudando o fluxo de arsina e fosfina, que foram crescidos usando três tamanhos de nanopartículas de catalizadores de Au diferentes de 2, 5 e 20 nm. Observamos que a forma do nanofio depende do tamanho de nanopartículas de Au. Para menores tamanhos, obteve-se uma forma de torre, enquanto que para o maior, a forma de agulha. A concentração de P é de cerca de 50% estimada por espectroscopia de fotoluminescência e de energia dispersiva de raios-X. A emissão óptica é de cerca de 1.5 μm , adequada para aplicação em dispositivos de telecomunicações. Nos NWs heteroestruturados de InAsP/InP, investigamos as amostras com tempos de inclusão diferentes de InAsP (2, 5, 10, 20 e 40 s) no InP, e elas foram crescidas com diferentes tamanhos de nanopartículas de Au (2, 5 e 20 nm) utilizadas como catalisador. Nessas amostras, todos os nanofios apresentam a forma de uma agulha. Os espectros de macro e micro-fotoluminescência mostram fortes emissões ópticas atribuídas à camada de InAsP e variam entre 800-1000 nm. A energia de emissão depende da quantidade de InAsP de acordo com o efeito de confinamento quântico. Também, observamos várias linhas estreitas nos espectros de micro-fotoluminescência de nanofios individuais atribuídos aos estados localizados das camadas InAsP. Essas linhas são provenientes de duas regiões, sendo uma delas da camada de InAsP axial catalisado e uma segunda, da camada lateral

de InAsP devido ao crescimento epitaxial. Este resultado mostra que os NWs de InAsP/InP apresentam alta qualidade cristalina e são sistemas promissores para a aplicação em dispositivos ópticos.

List of figures

Figure 1	Diagram of growth process assisted by <i>Au</i> -NPs of III-V semiconductor nanowires components (InP) by VLS method. (a) <i>Au</i> -NPs are deposited on the substrate. (b) The <i>Au</i> -NPs act as ideal sinks for the vapor supplied species (precursor gases are provided (TMI $-(CH_3)_3In$), phosphine (PH_3) and arsine (AsH_3)) of III – V group leading to formation of an eutectic alloy between the <i>Au</i> -NPs with the semiconductor constituents, the particles liquefy when absorb them. (c) With the supersaturation, the III-V materials begins the deposition at the interface NPs-substrate giving rise to the growth of the NW. (d) The growth of the NW continues until the supply of the gas ceases, then the <i>Au</i> -NPs solidify remaining on top of the NW.	21
Figure 2	Diagram representing the both axial and lateral growth assisted by <i>Au</i> -NPs of semiconductor nanowires by VLS method.	23
Figure 3	Arrangement of atoms (a) along the [111] direction of the Zinc Blende structure, and (b) along the [0001] direction of the Wurtzite structure.	24
Figure 4	Brillouin zones for a) Zinc Blende and b) Wurtzite atomic structures. Where Γ is at the center of the Brillouin zones.	25
Figure 5	Diagram of energy levels at the L and Γ points in ZB and the Γ points in WZ, with and without spin-orbit coupling [24].	25
Figure 6	Band structure for a typical III-V semiconductor around $k = 0$ in parabolic approximation for a) Zinc Blende and b) Wurtzite semiconductors [15].	26
Figure 7	Schematic diagram of the potential profile of the InP/InAsP quantum well. The blue solid lines correspond to the InP layer, while the red one, the InAsP layer. The black lines in the wells are subband edges of CB and VB.	27
Figure 8	Schematic spatial confinement impact and density of states function. a) Bulk Semiconductor Material, b) Quantum Well, c) Quantum Wire and d) Quantum Dot	28
Figure 9	NW structure and its potential profiles of our heterostructure NWs. (a) Schematic diagram of a needle-like NW; (b) Transversal cut in top of the NW, respectively, around the catalyst InAsP layer (red color), (c) Transversal cut close to the bottom region, respectively, where the lateral cylindrical InAsP layer (red color) is present. (d) Potential profile along radial direction of the b) - region. (e) Potential profile along radial direction of the c) - region. Blue and red color represent the InP and InAsP regions respectively.	29
Figure 10	Hydrogen-like bound state of electron and hole (Coulomb attraction) in an InAsP Quantum Well.	30
Figure 11	Shallow donor (D) and acceptor (A) levels in a semiconductor. The arrow indicates the D-A recombination.	31
Figure 12	Schematic representation of potential profile V_{conf} for two cases. When a) $K_{BT} <$ average localized states energy, the carriers remains localized in shallow wells. b) $K_{BT} >$ average localized states energy, the carriers are thermally excited and migrate to deeper wells. Filled circles represent the localized excitons, while the white circles represent the delocalized carriers. ξ_1 and ξ_2 represent the potential barrier heights.	33
Figure 13	Schematic representation of the T-dependent PL peak position (red dashed lines and symbols) and the band-gap variation with temperature (solid lines). E_{SD} represents the energy deviation between both lines. The red line s-type curve is attributed to emission from localized excitonic states.	34

Figure 14	Heterojunction between two materials with different lattice parameter. (a) Epitaxial layer with red circles (atoms) and substrate with blue circles in natural (unstrained) lattice. (b) Pseudomorphic epitaxial layer, where it is under compressive strain.	35
Figure 15	Potential profile of a QW. The long blue and pink arrows represent the absorption and emission process, respectively. While the short blue arrows represent the relaxation of the electron or hole into the QW energy levels.	37
Figure 16	Cone-like structure of the InAsP/InP NW. The regions A and B represent the transversal cut around the top and bottom, respectively.	40
Figure 17	SEM image of a NW, which presents a needle-like shape.	42
Figure 18	Schematic diagram of the macro-photoluminescence technique.	42
Figure 19	Schematic diagram of a micro-PL setup.	44
Figure 20	SEM images for samples A grown with Au-NPs of (a) 2, (b) 5 and (c) 20 nm for different magnifications	47
Figure 21	SEM images for samples B grown with Au-NPs of (a) 2, (b) 5 and (c) 20 nm for different magnifications.	48
Figure 22	SEM images for samples C grown with Au-NPs of (a) 2, (b) 5 and (c) 20 nm for different magnifications.	49
Figure 23	Spectra at 8K of alloy samples NWs carried out with laser power of 50 mW. (a) 2 nm (b) 5 nm and (c) 20 nm of Au-NPs. The number on each figure indicates the size of the Au-NPs used as catalyst, while the A, B and C on each peak correspond to the different samples CBE3109, CBE3110, and CBE3111, respectively.	50
Figure 24	PL spectra at 8K of samples (a) A (b) B and (c) C as a function of the laser excitation intensity, for the three different Au-NPs sizes. Blue vertical lines corresponds the PL-peak at 0.68, 0.81 and 0.86 eV for samples A, B and C respectively.	51
Figure 25	PL spectra vs temperature carried out with laser power of 50 mW for (a) A, (b) B and (c) C samples with three different Au-NPs sizes. Blue vertical lines corresponds the PL-peak at 0.68, 0.81 and 0.86 eV for samples A, B and C respectively.	52
Figure 26	PL spectra carried out with laser power of 50 mW and at 8 K for (a) A, (b) B and (c) C samples with three different Au-NPs sizes. Blue, red and orange numbers and arrows represent the different P concentration situated in different peaks.	54
Figure 27	PL spectra at 8K of samples A1, B1 and C1 carried out with excitation intensity of 500 μ W. Samples with (a) 2 nm (b) 5 nm and (c) 20 nm of Au-NPs are presented. Orange and blue solid vertical lines corresponds to donor – acceptor (D-A) and bound exciton (BX) recombination positions of InP-WZ, respectively.	57
Figure 28	PL spectra at 8K of samples (a) A1 (b) B1 and (c) C1 as a function of the laser excitation intensity	59
Figure 29	PL spectra of the sample (a) A1 (b) B1 and (c) C1 as a function of the temperature.	60
Figure 30	Energy Peak vs temperature of the PL spectra shown in Figs. 26-28. (a) A1, (b) B1 and (c) C1 samples for 2, 5 and 20 nm Au-NPs. The solid lines represent the theoretical Varshni equation for InP and the symbols are the experimental data.	61
Figure 31	PL spectra at 10K of samples A2 (10s), B2 (20s) and C2 (40s) grown with Au-NPs acquired in (left) 2011 and (right) 2013, using an excitation intensity of 100 μ W. Vertical solid lines, orange and blue, represent the D-A and bound exciton recombination in InP.	62

Figure 32	PL spectra at 8K of samples A2, B2 and C2 as a function of the laser power. All spectra are normalized with the maximum intensity. Left panel a) shows the spectra for samples grown with Au-NP acquired in 2011, and the right one, b) in 2013. The laser power increases from top to bottom.	63
Figure 33	Normalized PL spectrum at 100 μ W of heterostructure NWs measured at different temperatures. (a) A2, B2 and C2 with Au-NPs of 5nm/2011, (b) A2, B2 and C2 with Au-NPs of 5nm/2013.	64
Figure 34	PL peak energy vs temperature of samples A2, B2 and C2 with (a) Au-NPs 5 nm/2011 (b) Au-NPs 5 nm/2013. The data from sample C1 were also included. The solid lines represent the theoretical Varshni equation for InP and the symbols are the experimental data.	64
Figure 35	Typical optical microscopy images of our samples used in m-PL experiments. The green point indicates the laser spot.	66
Figure 36	Schematic diagram of a single NW. The InAsP layer represented by the red color is only illustrative diagram, since the actual spatial InAsP distribution is not known. Green solid lines represent the laser spot positions.	66
Figure 37	Spatial dependence of micro-PL spectra at 11 K and under 600 nW of excitation of four single NWs from sample C1 with Au-NPs (5 nm-2013) catalyst of (a-b) 2 nm and (c-d) 20 nm.	68
Figure 38	μ -PL spectra vs position measured of heterostructure NWs with Au-NPs catalyst of 5 nm. (a) Sample A2 at 15 K with 100 nW excitation intensity. (b) Sample B2 at 15 K with 80 nW excitation intensity. (c) Sample C2 at 11 K with 85 nW excitation intensity. The increment of the laser spot displacement is 1 μ m.	69
Figure 39	μ -PL spectra vs position measured at 15 K and at 80 nW of A2 (a) NW2 (c) NW3 and (d) NW 4. 2D intensity projection of (b) NW2 (d) NW3 and (f) NW4.	70
Figure 40	(a) μ -PL spectra vs position measured at 15 K and at 80 nW of B2 NW2, and (b) 2D intensity projection	72
Figure 41	(a) μ -PL spectra vs position measured at 15 K and at 80 nW of B2 NW3, and (b) 2D intensity projection	74
Figure 42	(a) μ -PL spectra vs position measured at 15 K and at 80 nW of C2 NW2, and (b) 2D intensity projection	75
Figure 43	(a) μ -PL spectra vs position measured at 15 K and at 80 nW of C2 NW3 and (b) 2D intensity projection.	76

List of tables

Table 1	<i>Energies for InP [15] and InAs [25].</i>	26
Table 2	<i>Values of typical α and β for InP, InAs and GaAs for ZB.</i>	32
Table 3	<i>List of InAsP-alloy nanowire samples grown with different PH_3 and AsH_3 flux. In each alloy, three other different NWs with Au-NPs size of 2, 5 and 20 nm were grown.</i>	41
Table 4	<i>List of nanowire samples of InAsP/InP heterostructures grown with different deposition times of InAsP. The alloy concentration is equivalent to the sample CBE3110. Similar to the 1st set, for each deposition time of the alloy three different Au-NPs sizes of 2, 5 and 20 nm were used.</i>	41
Table 5	<i>List of nanowire samples of InAsP/InP heterostructures grown with different deposition times of InAsP. The alloy concentration is equivalent to the sample CBE3110. For each deposition time of the alloy two different source of Au-NPs were used with 5 nm size, bought in 2011 and 2013.</i>	41
Table 6	<i>P concentration in % of the InAsP alloys, obtained from the EDS graphs (not shown here) for the three samples A, B and C with the Au-NPs of 5 nm only.</i>	48
Table 7	<i>PL peak wavelength and energy and P concentration x of the InAsP alloys.</i>	53

List of abbreviations

AsH₃	Arsine
Al	Aluminum
Au	Denote chemical compound gold
A.U. (a.u.)	Arbitrary units
CBE	Chemical Beam Epitaxy
CB	Conduction Band
D-A	Donor-Acceptor <u>Recombination</u>
DFA	Department of Applied Physics
DOS	Density of States
EDS	X-ray spectroscopy
FCC	Face Centered Cubic
GPO	Group of optical properties of matter
HCP	Hexagonal Closed Packet
HH	Heavy Hole
IFGW	Institute of Physics "Gleb Wataghin"
InP	Indium phosphide
InAs	Indium arsenide
InAsP	Ternary alloy compound of InAs and InP
LH	Light Hole
MBE	Molecular Beam Epitaxy
MOCVD	Metal Organic Chemical vapor deposition
NP(s)	Nanoparticle(s)

NW(s)	Nanowire(s)
PH₃	Phosphine
PL	Photoluminescence
QD(s)	Quantum Dot(s)
QW(s)	Quantum Well(s)
SEM	Scanning electron microscope
Si	Silicon
SF(s)	Stacking Fault(s)
TEM	Tunneling electron microscopy
TMI	Trimethylindium
μ-PL	Micro-Photoluminescence
VB	Valence Band
VLS	Vapor-Liquid-Solid phases
WZ	Wurtzite
ZB	Zinc Blende

Contents

Chapter 1	17
Introduction	17
Chapter 2	20
Theory.....	20
2.1 VLS (Vapor-Liquid-Solid) Growth of Semiconductor Nanowires	20
2.2 The crystal structure.....	23
2.3 Band structure of semiconductors.....	24
2.4 Semiconductor heterostructure	26
2.5 Semiconductor Nanowires	28
2.6 Exciton	30
2.7 Donor and acceptors	30
2.8 Thermal effect on semiconductor	31
2.8.1 Temperature dependent band gap.....	31
2.8.2 Carrier dynamics of localized states	32
2.9 Carrier density.....	34
2.10 Strain mismatch lattice.....	34
2.11 Photoluminescence process	36
Chapter 3	39
Sample preparation and Experimental Setup.....	39
3.1 Samples description	39
3.2 Photoluminescence Spectroscopy	42
3.2.1 Macro-Photoluminescence	42
3.2.2 Confocal micro-photoluminescence (μ -PL)	43

Chapter 4	45
Results and Discussion	45
4.1 PL in Alloy Samples	45
4.2 PL in Heterostructure Samples	57
4.3 μ -PL in Heterostructure Samples.....	65
 Conclusions	77
References	78

Chapter 1

Introduction

Semiconductor Nanowires (NWs) have attracted an increasing attention of the scientific and technology community in recent years due to their emerging applications to nanoscale and microelectronics devices industry, such as gas sensors [1], solar cells [2], electronic devices (field effect transistors) [3] and opto-electronic devices (detectors, lasers) [4]. Under fundamental point of view, for instance, the semiconductor NWs can be used as an alternative system to study *individual* low dimensional structures, such as single quantum wires (QWRs) and quantum dots (QDs). In addition, we can mechanically transfer NWs from one growth substrate to another, and subsequently integrate them to a given electronic circuit depending on the different objectives.

It is well known that phosphite and arsenite of III-V compounds (GaAs, InP, InAs, AlAs, and their alloys) present cubic crystal structure, Zinc Blende (ZB), [5] since it is the most stable phase. However, NWs with a diameter in nanometer scale show a hexagonal Wurtzite (WZ) phase [6, 7], which is a typical structure observed in nitrides [8]. The WZ phase is usually observed in NWs grown by vapor-liquid-solid (VLS) method and it occurs because the nucleation energy of some crystal plane of WZ phase, in certain growth condition, is lower than for ZB structure [7]. Despite several works report on the WZ phase phosphite and arsenite NWs, the physical properties of homo and heterostructure NWs are not deeply investigated.

In this work, we present our contributions on the experimental investigations of optical properties of InAsP/InP heterostructure NWs in WZ phase. The InAsP alloys, in particular, present optical emission around the telecommunication wavelength bands, 1.3 and 1.55 μm (InAs to InP), which are the minimum of the optical fiber attenuation [9].

Recently, several works have reported optical properties of WZ InAsP/InP heterostructures NWs, when they are grown by VLS method assisted by Au-NPs catalysis and implemented in the Molecular Beam Epitaxy (MBE) [9], Metalorganic Vapor Phase Epitaxy (MOVPE) [10-14], and Chemical Beam Epitaxy (CBE) [13] systems, obtaining different results. Despite significant advances in NW growth, the quality of the stacking nanowires results difficult to control. For example, by adjusting the growth parameter (e.g. chemical compounds concentration, temperature of growth, and size of the Au-NPs), the NWs structure changes, consequently the optical and physical properties also change. For instance, the photoluminescence (PL) wavelength can be tunable by varying the *As* or *P* insertion time [10-12] as well as the flux of V/III ratio [9]. Furthermore, it is known that in addition to the axial catalyst growth [13], a radial or lateral epitaxial growth is also occurs [11], resulting additional emissions in the PL spectra for heterostructures. In fact, sharp narrows and strong emissions are observed in InAsP/InP NWs attributed to the emission from two regions. Several other structures have been investigated, such as, in single [10, 13] and multiple [9, 10] QDs, and the possibility of tuning the QD size as well [14].

Other effects that are usually observed in NWs are, e.g., the Stacking Faults (SF) effect [9, 10, 13], polytypism with WZ/ZB alternated structure [14] and twin defects [4]. These effects, naturally, affect the optical emissions and for technological application excellent physical properties are required. Despite these effects, InP/InAsP NWs is a promise system for opto-electronics materials.

This dissertation was also motivated by previous works of the group on the investigations of the optical properties of InP [15, 16] and InAs [17, 18] NWs. In those works, they measured the energy of the band gap and the valence band splitting and optical phonon modes in WZ phase InP and InAs NWs. Due to the high quality of samples it seemed opportune to investigate heterostructures in NWs, which is the main focus of this thesis. The NWs are grown by the VLS method in a CBE system at the Applied Physics Department of the Institute of Physics of Unicamp by Prof. Mônica Alonso Cotta and her student.

In recent years, InAsP alloy and InAsP/InP heterostructure NWs both in WZ phase have been successfully synthesized and their physics properties have been investigated [9-14]. The summary of main results will be describe below:

The authors of ref. 9 and 11 synthesized high quality InAsP/InP NWs with a high *As* concentration [9, 11]. They showed that adjusting the InAsP amount and tuning the *As*

concentration it is possible to obtain a emission at $\sim 1.3 \mu\text{m}$, promising for infrared light emitting devices. Additionally a PL at room temperature was also measured [11]. Zwiller et al. [13] investigated very short InP NWs including InAsP segments, less than 10 nm. The single NWs presented a sharp emission linewidth, as sharp as $\sim 30 \mu\text{eV}$, attributed to the InAsP quantum dots (QDs). Tchernycheva et al [9], in addition, demonstrated the functionality of multiple insertions of InAsP into InP NWs. For 2 insertions case the $\mu\text{-PL}$ spectra present the full width at half maximum as small as $\sim 120 \mu\text{eV}$ and this linewidth can be even narrower depending on the number of InAsP insertions. Tateno et al [10] demonstrated a detailed work of growth conditions under V/III flux variation, where according to the conditions NWs can obtain a different morphology. The $\mu\text{-PL}$ spectra of single NWs show the multiple peaks that come from two regions: from lateral and radial InAsP insertions along the NWs.

In the present work, two different samples are studied by optical measurements, the first one is InAsP alloy NWs and the second one, InAsP/InP heterostructure NWs, both are grown by VLS method in a CBE machine. The samples are similar to those reported in previous works, however, the InAsP alloy and heterostructures in WZ phase are not well known and they require optimization of the growth condition in order to obtain high quality samples. We observed relatively strong optical emission from all samples indication of high quality samples for optical properties investigations. We also observed strong sharp peaks from the InAsP/InP NWs around $0.9\text{-}1.0 \mu\text{m}$ of wavelength attributed to the emissions from two regions, axial growth layer and lateral growth one. However, in contrast to the previous works, these two emissions are not in the different spectral range.

The dissertation is organized in the following way. Chapter 2 briefly describes the VLS crystal growth method, theoretical background of semiconductors, and optical properties used to analyze experimental results. Chapter 3 shows the experimental details, including samples characteristics and experimental setup. Chapter 4 presents the experimental results and analysis of macro-PL measurements of ensemble of InAsP NWs and InAsP/InP heterostructure NWs under different experimental conditions, such as changing the sample temperature, excitation intensity, and different positions along the wire. Additionally the P concentration and morphology of InAsP NWs are compared with EDS and SEM measures. Finally, a brief conclusion is presented.

Chapter 2

Theory

2.1 VLS (Vapor-Liquid-Solid) Growth of Semiconductor Nanowires

The most common way to grow semiconductor nanowires is the *Vapor-Liquid-Solid* (VLS) method. Wagner and Ellis proposed it in 1964, who suggested an explanation for the *Si* whiskers with the existence of liquid gold on the top of the substrate when the *Si* vapor is present in the atmosphere [19]. The name of the growth mechanism came from the three phases appearing simultaneously during the growth process: it uses precursor gases (*Vapor*) and a liquid metal-alloy (*Au+Si*) droplet-catalyzed (*Liquid*) to form the nanowire (*Solid*).

The NW growth by the VLS method has been performed in several growth systems, e.g. chemical beam epitaxy (*CBE*) [20], molecular beam epitaxy (*MBE*) [21], and metalorganic chemical vapor deposition (*MOCVD*) [22]. In this work, we used the CBE growth system. The CBE system consists of the chemical precursor sources for deposition, desorption and surface diffusion of atoms of the material to be grown up over the substrate. The CBE allows growing the atomic monolayers of the crystal on a substrate. We can also grow multi-layers of different materials (heterostructures), with the same or different crystalline structures,

The chemical precursor gases used in our work are trimethyl indium (TMI – $(\text{CH}_3)_3\text{In}$), for III-compound, phosphine (PH_3) and arsine (AsH_3), for V-compound, which allow the growth of InP, InAs and their ternary alloy InAsP compounds. The V-compound gas (*In* source) suffers pyrolysis when they come into the vacuum CBE chamber and upon contact with the heated substrate, while the TMI gases suffer pyrolysis only through the contact with the substrate. Consequently, they release the constituent atoms on the substrate surface and diffuse on the surface and grow the epitaxial layer.

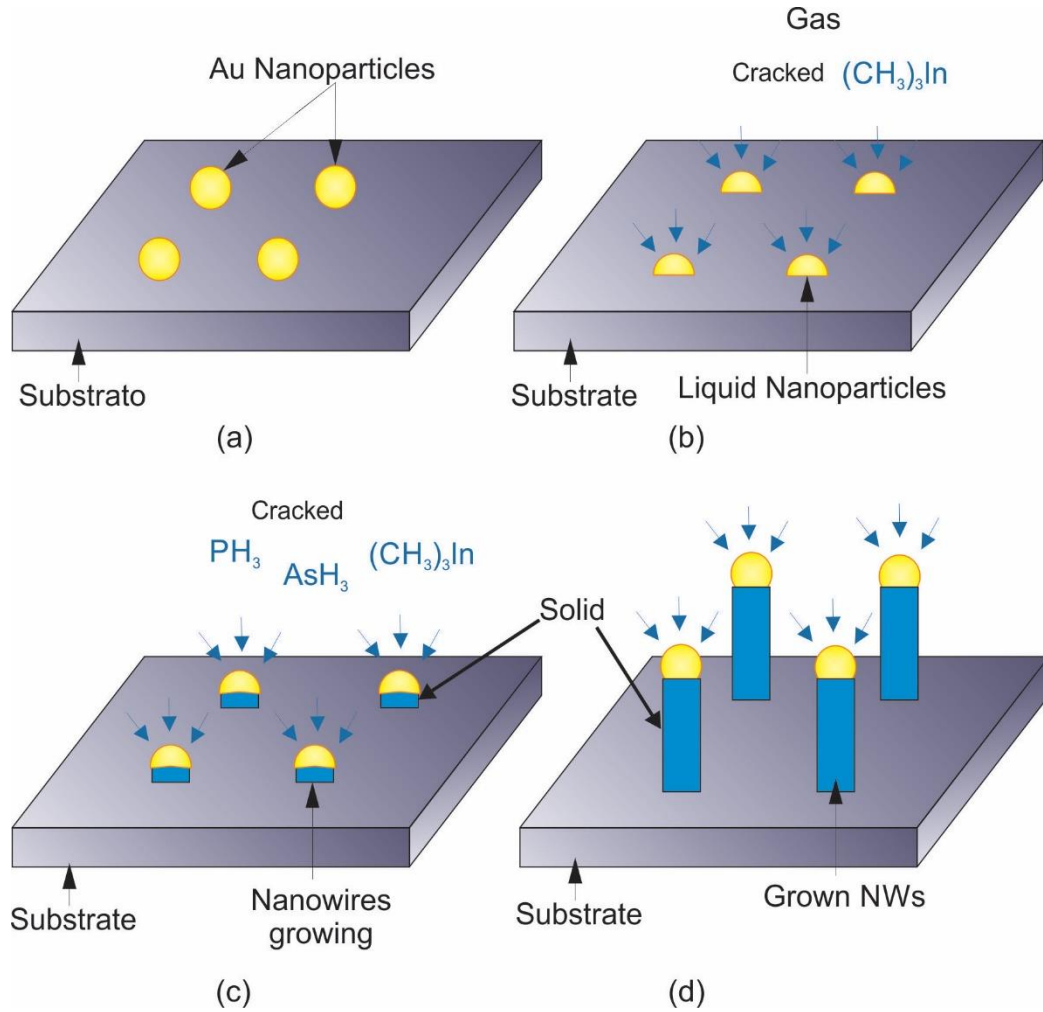


Figure 1. Diagram of growth process assisted by Au-NPs of III-V semiconductor nanowires components (InP) by VLS method. (a) Au-NPs are deposited on the substrate. (b) The Au-NPs act as ideal sinks for the vapor supplied species (precursor gases are provided (TMI - $(CH_3)_3In$), phosphine (PH_3) and arsine (AsH_3)) of III - V group leading to formation of an eutectic alloy between the Au-NPs with the semiconductor constituents, the particles liquefy when absorb them. (c) With the supersaturation, the III-V materials begins the deposition at the interface NPs-substrate giving rise to the growth of the NW. (d) The growth of the NW continues until the supply of the gas ceases, then the Au-NPs solidify remaining on top of the NW.

The procedures of the NW growth by VLS method can be summarized in four steps sketched in Figure 1. Before starting the growth process, firstly, the surface of the substrate must be deoxidize by heating up, and spread the drops of water or alcohol, containing metal (catalyst) nanoparticles such as gold and silver onto the (111)B substrate deoxidized. Then, place the substrate with the metallic droplets into the growth chamber (CBE chamber) and the growth procedure starts, heating the substrate and applying the precursor gases. Figure 1(a) depicts the first step of the VLS method. After that, the precursor gases (from the III and V group) trimethyl indium (TMI - $(CH_3)_3In$), phosphine (PH_3) and arsine (AsH_3) (where PH_3 and AsH_3 previously suffer pyrolysis) are injected in a system with low pressure in vapor state,

where TMI gas is cracked, and the elements III and V are diffused into Au-NPs to form a liquid as shown in Figure 1(b). The pyrolysis of element III occurs at both the substrate surface and at the Au-NPs, as well as at the surface of the nanowires. Those atoms that are on the substrate surface can move freely and eventually move toward the catalyst drops, according to the diffusion length that they possess, and when they reach the Au-NPs these are adsorbed and diffused into the NPs. When the mixed system (atoms + *Au*) achieves the supersaturation it becomes liquid and the NW growth starts.

In general, the working temperatures are lower than the melting point of the bulk *Au* (~1064 °C). However, its NPs form a eutectic alloy melting at lower temperature after diffusion of the III and V elements. The alloys containing *Au* with the semiconductor elements (III-V in this case) become supersaturated at certain concentration of the III-V elements and change the phase to liquid. For instance, *In* has a low melting point around 400 – 500 °C, but mixed with *Au* and creating the eutectic alloy will result in a low melting point of ~454 °C, which is closer to the temperatures where the CBE operates. When the growth achieves a supersaturation regime it promotes fast local precipitation and gives rise to the nucleation at the interface between the droplets and the substrate, as shown in Figure 1(c), up to ceasing the supply of the precursor gases (Figure 1(d)). Finally, the sample is cooled down under V-element vapor to avoid the surface degradation.

In addition to the catalyst growth discussed above, lateral growth also occurs. Figure 2 shows the schematic diagram of two distinct growths along axial and lateral directions. The growth along the lateral direction is the similar of the epitaxial layer mode grown directly on the substrate surface and its growth rate is usually slower than the catalyst one when the atomic diffusion length is larger than the NW length. This process is also used to cover the NW with other materials to passivate the surface or to design different heterostructures, as our samples [9].

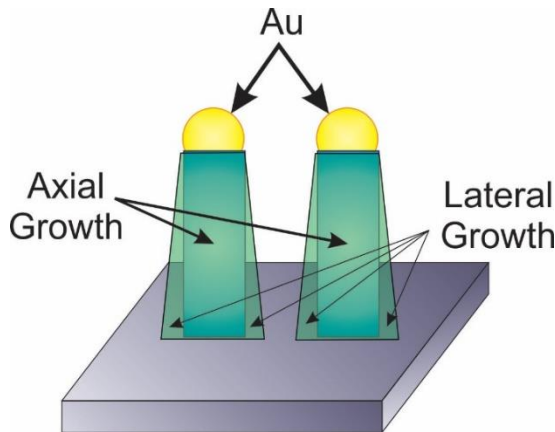


Figure 2. Diagram representing the both axial and lateral growth assisted by gold (Au) NPs of semiconductor nanowires by VLS method.

2.2 The crystal structure

In Fig. 3, we present the unit cells and the stacking of atoms in the ZB and WZ phases. We mentioned above that in the bulk form of III-V materials (e.g., arsenides and phosphides) it is more common to find the Zinc Blende (ZB) crystal structure, since this phase is the most stable. However, for nanoscale volumes, the hexagonal WZ structure is also observed. Since the angles and distances between the different atoms are changed for the different crystal structures, the nucleation energy of some crystal planes can be lower in the WZ than in the ZB phase.

The ZB crystal is formed by two interpenetrating face-center-cubic (FCC) Bravais lattices (each of two different atomic species), therefore, it is formed by two atoms per unit cell, whereas the WZ structured is constructed from two interpenetrating hexagonal close-packed (HCP) lattices, i.e., 4 atoms per unit cell. When comparing the ZB and WZ crystal structures, the crystal lattices are very much alike when we compare the $[111]$ direction of ZB with the $[0001]$ direction of WZ, but the stacking of the layers is slight distinct. The WZ stacking period is mapped as AB... (Where each letter represents atomic bilayer along the $[0001]$ direction) the period repeats each two layers, while in the ZB, it is ABC... along the $[111]$ direction and the period repeats every 3 layers.

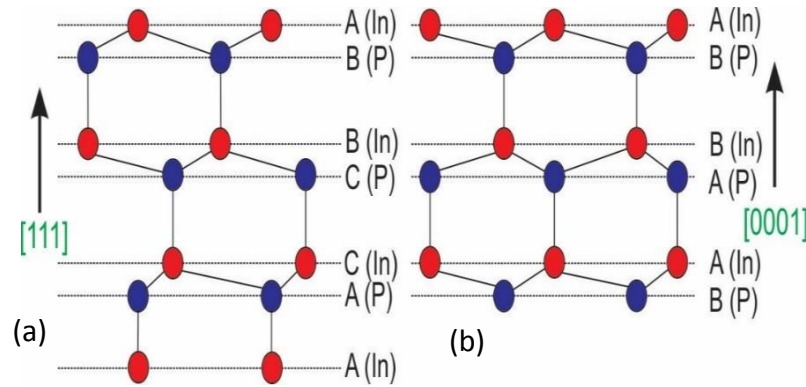


Figure 3. Arrangement of atoms (a) along the $[111]$ direction of the Zinc-Blende structure, and (b) along the $[0001]$ direction of the Wurtzite structure.

2.3 Band structure of semiconductors

Semiconductors and insulators are distinguishable from other materials for the existence of gaps in their electronic excitation spectra, however semiconductors presents smaller energy gaps. These are characterized as a covalent bonding (only IV elements semiconductors present a complete saturation of the covalent bonding) of interaction between nearest neighbor atoms and presenting full-filled valence band (VB) and empty conduction bands (CB).

In the case of our III – V compound semiconductors, e.g. the InAs and InP, they have 8 valence electrons (3 electrons of In (or As) and 5 of P) in the outer layer available to participate in chemical bonds. This results in a hybridization [23], where one electron from the s -orbital is excited into the p -orbital forming a molecular orbital sp^3 , which produces a tetrahedral configuration resulting in a ZB structure. These new orbitals are represented by the linear combination of atomic orbitals to form bonding and antibonding orbitals and this maximizes the overlap between the electronic wave functions of the atoms (e.g. InP). The bonding orbitals are at a lower energy than the antibonding orbitals, so they are the first to fill up, in the s and p -orbitals like, 2 and 6 electrons occupy the bonding orbitals respectively, forming the valence band (VB). At the center of the Brillouin zone it is mostly formed by p -orbital. In the antibonding orbitals, they form the unoccupied conduction band (CB) and it is formed mostly by s -orbitals at the zone center. The difference between the maximum of the valence and minimum of the conduction band energies is known as the band gap “ E_g ”.

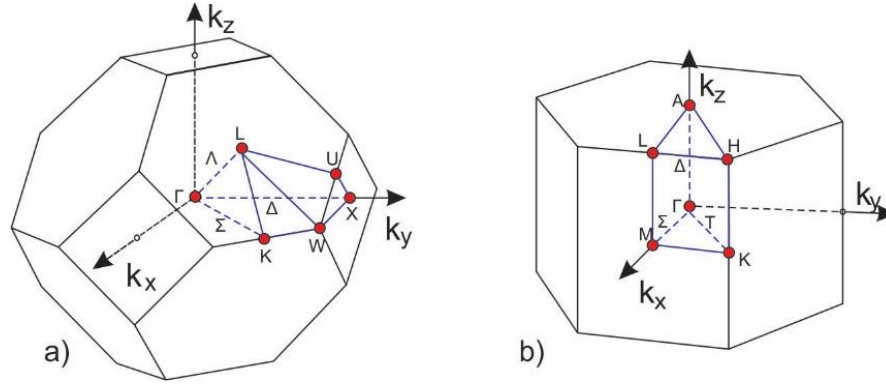


Figure 4. Brillouin zones for a) Zinc Blende and b) Wurtzite crystal structures. Where Γ is at the center of the Brillouin zones.

Due to the similarities of the two crystal phases, many of the high symmetry points in the Brillouin zones of ZB and WZ are related to each other. Both structures have a direct band gap. Figure 4 shows the relationships between the Brillouin zone center states along $\Gamma - L$ points in ZB and the corresponding $\Gamma - A$ points in WZ. The zone edge for the WZ is smaller than the ZB one in this direction, resulting approximately folding of the band structure of the latter to form the WZ band structure [24].

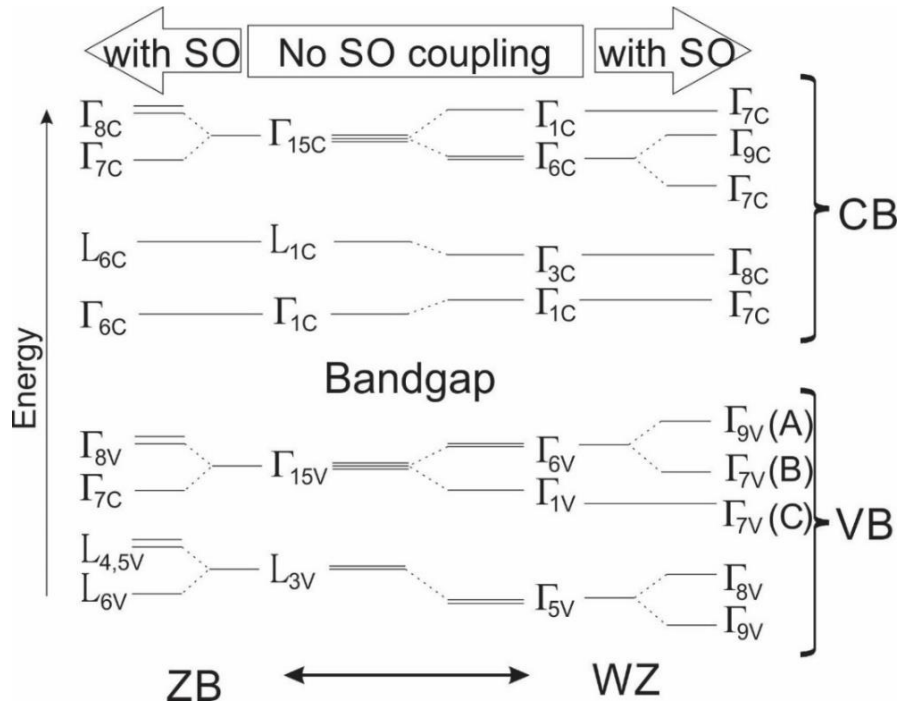


Figure 5. Diagram of energy levels at the L and Γ points in ZB and the Γ points in WZ, with and without spin-orbit coupling [24].

Due to the lower symmetry of WZ structure, in contrast to well-known ZB phase, the top of the valence band is broken. As shown in Figure 5, in the absence of the spin-orbit coupling, the hexagonal crystal field of WZ splits the p -like state of the top of the VB in Γ point (degenerate Γ_{15} in ZB case) into four-fold degenerate Γ_6 and doubly degenerate Γ_1 states. Including spin-orbit coupling, Γ_{6v} splits into the Γ_{9v} heavy-hole (called A-band) and the Γ_{7v} light-hole (called B-band). The Γ_1 becomes Γ_{7v} (called C-band). As a result, all zone center states in WZ belong to either Γ_7 , Γ_8 or Γ_9 , as shown in Fig. 5. In terms of the p -orbitals, these states are $p_x, p_y \rightarrow \Gamma_6$ and $p_z \rightarrow \Gamma_1$. Since CB has symmetric s -orbital, the interband optical transitions between CB and CB are polarized according to the polarization of the VB Bloch wave function. Bands A and B are polarized in the basal plane (p_x, p_y), while C-band is along the c -axis (p_z). In the parabolic approximation, around $k = 0$, as shown in Fig. 6, we plot the band structure of InP or InAs for ZB and WZ phases, showing the energy splitting and the band gap energies [15]. Table 1 presents the energy values for InAs and InP semiconductors.

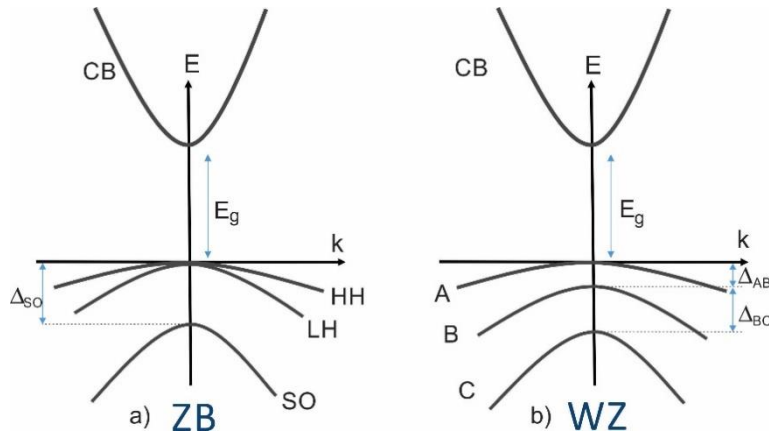


Figure 6. Band structure for a typical III-V semiconductor around $k = 0$ in parabolic approximation for a) Zinc Blende and b) Wurtzite semiconductors [15].

Table 1 - Energies for InP [15] and InAs [25].

	InP[15] [eV]	InAs[25] [eV]
Δ_{AB}	0.044	0.070
Δ_{BC}	0.143	0.294
Δ_{SO}	0.11	0.312
E_g -ZB	1.423	0.415
E_g -WZ	1.503	0.458

2.4 Semiconductor heterostructure

Bulk semiconductors are characterized by having large size and no reduced dimensionality (from 1 to more than 100 nm), because their size is bigger than the de Broglie wavelength of an electron at the Fermi level in all dimensions. For nanostructured semiconductors and, particularly, heterostructures, low dimensional systems are obtained. The combination of different materials with different band gaps, results in electrons and holes spatially confined when the size of the layers are reduced until be comparable to the thickness

of the effective exciton Bohr radius. The general classification based on the number of dimensions where carriers are confined is the following:

One-dimensional confinement (Quantum Wells, QWs): Electrons are free to move only in two directions and confined to one direction. Two dissimilar semiconductors with different band gaps can be joined to form a heterojunction. The discontinuity in both the conduction band (CB) or valence band (VB) forms the potential well, as shown in Figure 7 for the InP/InAsP semiconductor. Consequently, one material with narrower-band gap, such as ‘InAsP’ for our case, is sandwiched between two layers of a wider-band gap material, such as ‘InP’, forming a double heterojunction. The states of the electrons and holes in the quantum wells (in the InAsP region) form subbands, and the levels shown in Fig. 7 represent the subband edges and electrons and holes can move freely in a perpendicular direction of the confinement direction [26].

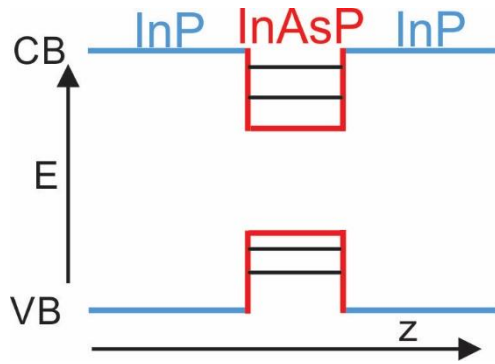


Figure 7. Schematic diagram of the potential profile of the InP/InAsP quantum well. The blue solid lines correspond to the InP layer, while the red one, the InAsP layer. The black lines in the wells are subband edges of CB and VB.

Two-dimensional confinement (Quantum Wires, QWRs): Electrons (or holes) are free to move in only one direction, so that confinement is along the other two directions. Similar to the QWs the carriers states form subbands.

Three-dimensional confinement (Quantum Dots, QDs): Since, the Quantum Dot is a nano-sized particle; the electrons are confined in all three-dimensional space and cannot move anywhere. Therefore, no energy dispersion exists for carriers, i.e., the states are discrete like atoms.

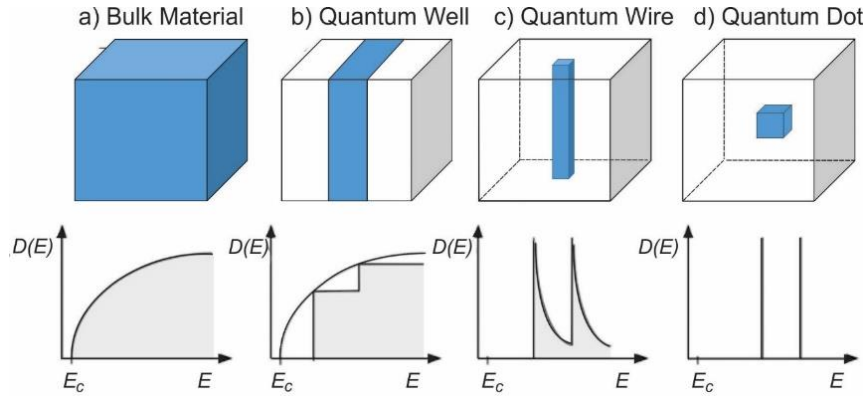


Figure 8. Schematic spatial confinement impact and density of states function. a) Bulk Semiconductor Material, b) Quantum Well, c) Quantum Wire and d) Quantum Dot

The spatial confinement produces different characteristics of density of states (DOS), determining both the electronic transport and optical properties. The DOS describes the number of available electron states within a specific energy range. Each structure possesses a different DOS. For example, referring to Fig. 8.a, the *bulk* semiconductor DOS - for parabolic approximation of the energy dispersion - has a square root energy dependence. In QWs, the DOS accompanies the subbands and at each subband the DOS is constant and represented by the step-like function, see Fig. 8b. In QWRs (Fig. 8c), the DOS of each subband depends on the inverse square root dependence, i.e., very high DOS is obtained around the $k = 0$, while in the QDs the DOS is just a series of delta functions, due to the discrete energy levels, as shown in Fig. 8d.

2.5 Semiconductor Nanowires

In contrast to the usual epitaxial growth on a substrate, NWs present advantageous possibilities to grow heterostructures, making them very attractive systems. For instance, as mentioned above in section 2.1, the growth along the axial and lateral direction allows growing heterostructures with confinement of carriers along these two different directions. They can also be manipulated to transport them along the wire with different dimensionality, as in QWR or circular QW or quantum cylinder. In addition, the WZ phase introduces a different band structure than ZB, which presents different optical properties because of different energy splitting.

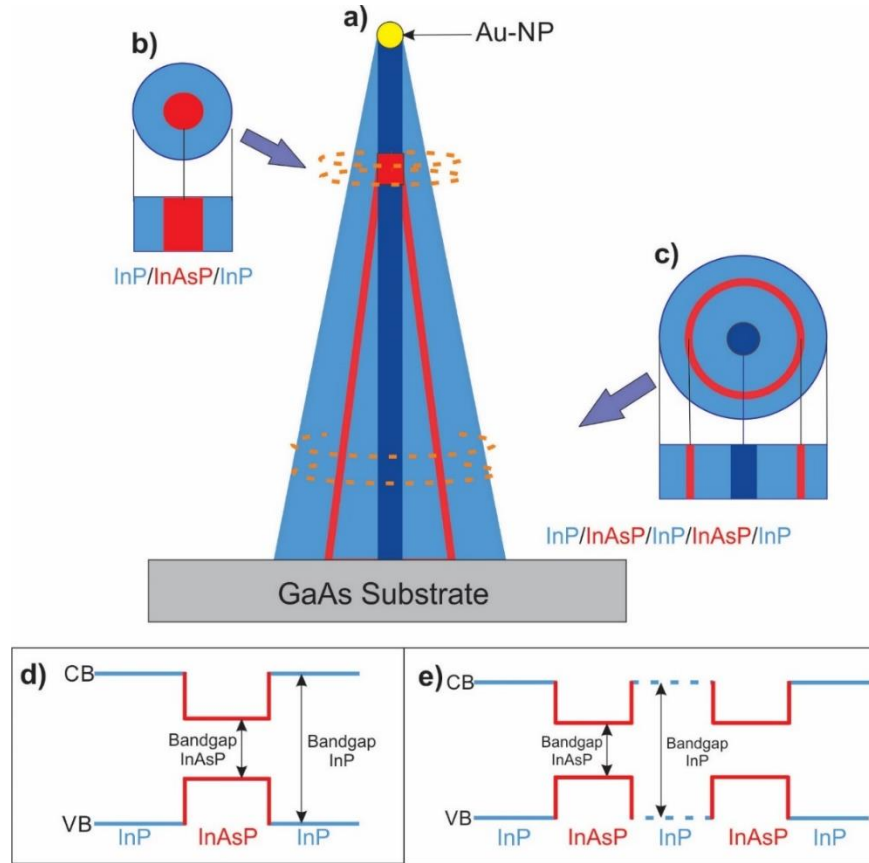


Figure 9. NW structure and its potential profiles of our heterostructure NWs. (a) Schematic diagram of a needle-like NW; (b) Transversal cut in top of the NW, respectively, around the catalyst InAsP layer (red color), (c) Transversal cut close to the bottom region, respectively, where the lateral cylindrical InAsP layer (red color) is present. (d) Potential profile along radial direction of the b) - region. (e) Potential profile along radial direction of the c) - region. Blue and red color represent the InP and InAsP regions respectively.

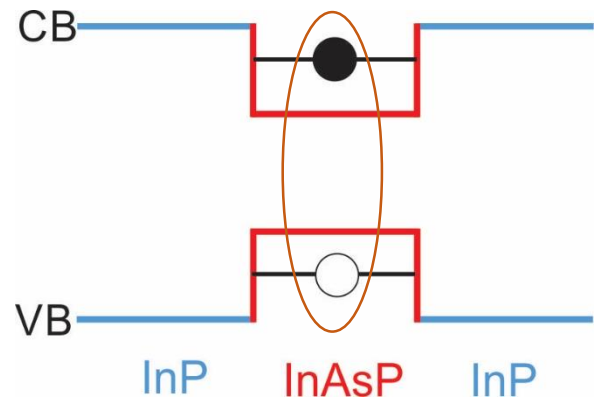
The NWs investigated in this dissertation present a type-I interface, similar to that shown in Figure 7. Since the conduction (valence) band minimum (maximum) of the InAsP is lower (higher) than the surrounding conduction (valence) band of InP, it results in lateral and radial confinement.

Figure 9 shows an illustrative diagram of the sample structure and the potential profiles. Blue and red colors represent the InP and InAsP, respectively. Figure 9.a depicts the InAsP/InP heterostructure NW. The orange dashed lines represent the transversal cut close to the top and the bottom region. The transversal cut in fig 9.b shows the catalyst InAsP core and InP shell, while Fig. 9.c shows the lateral InAsP layer between core and shell InP layers. In both cases, the electron and holes are confined in InAsP layers, which is represented by the potential profile, shown in fig 9.d and 9.e, of the minimum (maximum) of CB (VB) along the lateral direction. Both regions contribute to the optical emission.

2.6 Exciton

An electron in a semiconductor can be optically excited, being promoted from VB to the CB, leaving a hole in the VB. Due to the opposite charge between electron and hole the Coulomb attraction leads to a bound state, similar to the hydrogen atom, but in a dielectric material. The new quantum state of electron-hole pair forms a quasi-particle known as an *exciton*.

Figure 10. Hydrogen-like bound state of electron and hole (Coulomb attraction) in a InAsP Quantum Well.



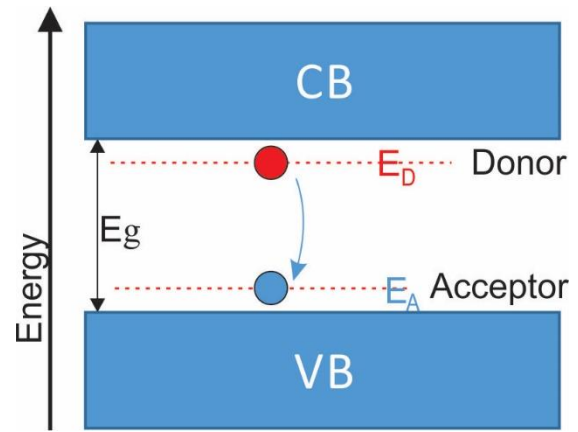
The total energy of an exciton is lowered relative to the band gap, therefore, the energy recombination of a free exciton is smaller than the band gap energy. The difference between the band gap and the exciton transition energy gives the exciton binding energy. The typical exciton binding energy is around few meV for III-V compounds, because the carrier effective mass is smaller than free electron mass and dielectric constant is around 12 times the vacuum electric permissivity; e.g., for GaAs and InP the binding energies are very similar, around ~4-5 meV, while for InAs is ~1 meV [27]. Their effective Bohr radii are around ~11 nm for GaAs and InP, and ~34 nm for InAs.

2.7 Donor and acceptors

An advantage of semiconductors compared to the metals, under point of view of the electronic transport, is their doping with foreign atoms (shallow impurities) to control the carrier density to obtain *n* or *p*-type material. For III-V compounds, the shallow impurities are easily

doped, therefore, they are usually contained even in undoped materials. The shallow levels of donors (E_D) or acceptors (E_A) are close to the respective band edge and the photo-created electron and holes are easily trapped by these levels and then recombine. If donor and acceptor are spatially very close to each other the electron and hole recombine from those levels, effect known as donor-acceptor recombination (D-A), see Fig. 11. Even binding energy depends on the distance between donor and acceptor, the transition energy is approximately around the $E_g - E_D - E_A$. This optical emission is very usual in the photoluminescence spectra of bulk semiconductors even at low concentration and it is also followed by the optical phonon replica at a lower energy range. Due to the limited impurity concentration, the D-A intensity saturates under a high excitation condition, which is used to identify it, while the excitonic recombination rather remains increasing. The D-A emission also shows slightly blue-shifted as the excitation intensity increases due to the decrease of the average distance between electron and hole.

Figure 11. Shallow donor (D) and acceptor (A) levels in a semiconductor. The arrow indicates the D-A recombination.



2.8 Thermal effect on semiconductor

2.8.1 Temperature dependent band gap

It is very usual to use the Varshni's phenomenological model to describe the band gap variation with temperature [28]. It is a simple model, but useful to understand the basic temperature dependence of the band gap. We do not discuss in details other models, because it is out of the scope of the work. In Varshni's model, two main mechanisms are considered:

- i) The relative position of the valence and conduction bands changes due to electron-lattice interaction when the temperature changes. This contribution is dominant.

ii) Changing the temperature, the thermal dilatation of the lattice change the band gap energy. This contribution is usually about 25% of the total variation in the bang gap [29].

The Varshni's relation for the temperature dependence of semiconductors band gaps is described with the following equation:

$$E_g = E_g(T = 0) - \alpha \frac{T^2}{T + \beta}$$

where $E_g(T = 0)$ is the band gap energy at absolute zero on the Kelvin scale in the given material, and α and β are material specific constants that need to be determined. As shown in Table 2 the α and β for several materials in the ZB phase, in WZ these values are unknown.

	InAs[30]	InP[5]	GaAs[5]
$\alpha(10^{-4} \frac{eV}{K})$	2.76	3.63	5.405
$\beta(K)$	93	162	204

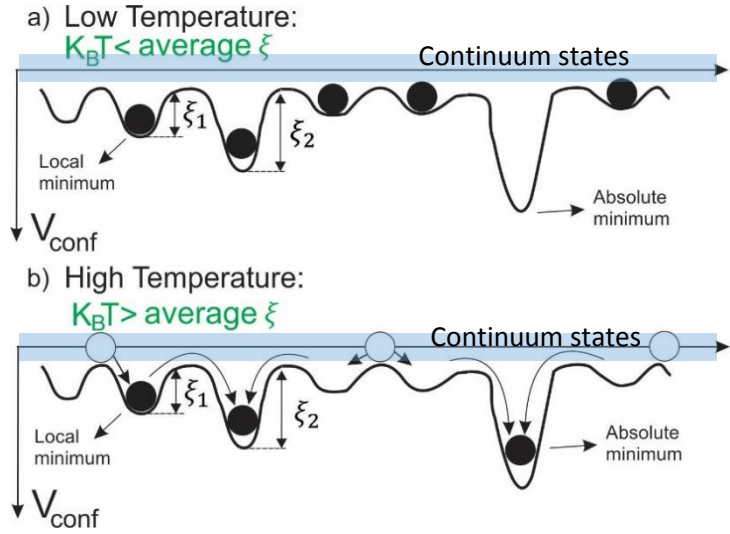
Table 2 - Values of typical α and β for InP, InAs and GaAs for ZB.

2.8.2 Carrier dynamics of localized states

As temperature increases, the probability of carriers to occupy higher-energy excited states also increases according to the Boltzmann factor, $e^{-\frac{E}{k_B T}}$. This factor describes the probability of an electron to occupy a state E at a temperature T , where k_B is the Boltzmann constant. The factor $k_B T$ (explained below) is important to understand the carrier transference between localized state in confined states, such in QW, QWRs and QDs, affecting the photoluminescence spectra (we will discuss the photoluminescence process in the next section).

Let us assume that we have localized and continuum states in a system, as shown in Fig. 12. The carriers in the continuum states can move freely, but when they are trapped in the localized states, it depends on the thermal excitation energy to promote them to the continuum states. It only occurs if thermal energy $k_B T$ is around or larger than the deepness of the localized state. This process is used to describe the red-shift observed in the photoluminescence spectra in QWs and QDs [38].

Figure 12. Schematic representation of potential profile V_{conf} for two cases. When a) $k_B T < \text{average localized states energy}$, the carriers remain localized in shallow wells. b) $k_B T > \text{average localized states energy}$, the carriers are thermally excited and migrate to deeper wells. Filled circles represent the localized excitons, while the white circles represent the delocalized carriers. ξ_1 and ξ_2 represent the potential barrier heights.



At very low temperatures (Figure 12.a), $k_B T$ is much smaller than the average localized state energy. The carriers are thermalized to local minima and all localized states have the same opportunity to be occupied by electrons, i.e., the photoluminescence must reproduce the density of states of the localized states. Increasing the temperature (Figure 12.b), the carriers in shallower wells have sufficient thermal energy to overcome the small potential barriers in the local potential (called ξ_1) to the continuous state of the system (above the barrier).

In the continuous states, the carriers can move freely and, eventually, fall to other localized states. When they drop to deeper wells, where the thermal energy is not enough to re-excite them to the continuous state, they thermalize to the local potential minimum (called ξ_2). These carriers can emit photons with lower energy than the empty shallow localized states and the total net emission energy becomes smaller than the emissions when the all localized states are occupied. The latter, the PL peak position follows practically the band gap temperature variation, while the former presents much larger energy reduction.

In Figure 13, we present the temperature-dependence of the photoluminescence peak expected for QWs or QDs systems containing strong localized states. Two black solid lines represent the band-gap variation with temperature corresponding to the average localized states energy (upper curve) and lowest localized energy (lower curve), respectively, while in red symbols represents the temperature-dependent PL peak position based on the mechanism described above. The red symbols starts matching with the solid line of upper black line at low temperature condition, reflecting the density of states of the localized states (corresponding to the average energy) as mentioned above. Increasing the temperature, the red symbols decreases

rapidly and achieve the lower black line, which is an effect of the carrier transference from the high energy states to the low energy ones via continuum states. After that, for high $k_B T$, larger than the deepness of the localized states respect to the continuum states, denoted by E_{SD} , all localized states have same probability to be occupied by carriers, therefore, the photoluminescence peak reflects the peak of the density of states, following the upper line again. Depending of the deepness of the localized states respect to the thermal energy different shape of the curve can be obtained.

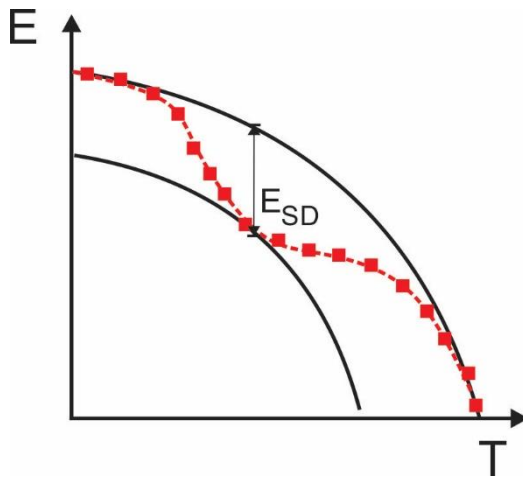


Figure 13. Schematic representation of the temperature dependent PL peak position (red symbols) and the band-gap variation with temperature (solid lines). The upper and lower lines represent the highest and lowest energy of the localized states. E_{SD} represents the energy deviation between both lines.

2.9 Carrier density

Varying the intensity of optical excitation or some electronic excitation modifies the dynamic of carriers, affecting the number of electrons and holes in the CB and VB of the potential wells. Higher number of electron and holes will increase the probability of occupying higher energy states. Consequently, higher energy recombination may be observed which follows the Fermi Statistics [39], resulting in a shift of the maximum of the photoluminescence peak towards the higher energy region, which is opposite to the thermal effect. In this analysis, we do not consider the many-carrier effects.

2.10 Strain mismatch lattice

When a heterostructure involves semiconductors with different lattice constants \mathbf{a} , the layers will be under strain effect when they are coherent or pseudomorphic. Figure 14 depicts the atoms of two different materials in two conditions, unstrained natural (a) and strained layers (b) of the material with red circles grown on the substrate with blue atoms. For an epitaxial

layer, considering that the upper layer has larger lattice parameter as compared to the lower one, as InAsP on InP case, and that the former follows the lattice parameter of the substrate, the upper layer will be under biaxial compressive strain, as shown in the Fig. 14.b [23]. The biaxial compressive strain increases the band gap energy and also breaks the degeneracy at the top of the VB splitting the HH and LH bands in the ZB crystal or changes the energy separation between A and B bands for WZ crystal.

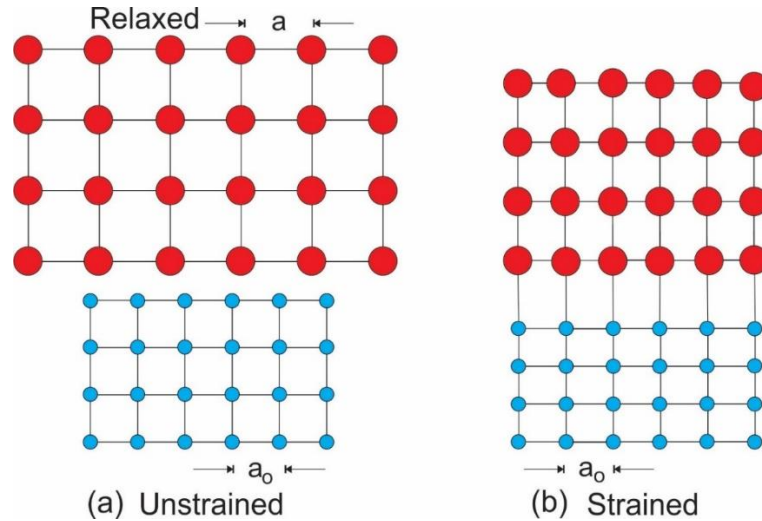


Figure 14. Heterojunction between two materials with different lattice parameter. (a) Epitaxial layer with red circles (atoms) and substrate with blue circles in natural (unstrained) lattice. (b) Pseudomorphic epitaxial layer, where it is under compressive strain.

The lattice mismatch between two different semiconductors is given by [31]:

$$\varepsilon_{xx} = \varepsilon_{yy} = \frac{a_0 - a}{a}$$

Where ε_{xx} and ε_{yy} represent the strain components along the planar x and y directions (biaxial strain), while the a and a_0 represent the lattice parameter constants of strained and natural lattices. We can estimate the lattice mismatch of the heterostructure InAsP/InP, the lattice parameter of the InAsP must be determined by linear interpolation [32] of the data of the binary materials InP and InAs, which are 4.150 and 4.283 Å [33] respectively. For two different concentration, for instance, 0.32 and 0.48 of P content, the InAsP lattice parameters are 4.24 and 4.219 Å resulting in a $\varepsilon = 2.1$ and 1.6 %, respectively. The strained layer shifts the energy gap to higher energy [34].

2.11 Photoluminescence process

The interaction of a semiconductor with an electromagnetic radiation from an excitation source, with higher photon energy than the bandgap E_g , will result in an interband optical transition between the CB and VB. An electron is promoted from the filled valence band to the empty conduction band, as shown in Fig. 15. This injects an unoccupied initial state E_i in the valence band, which is equivalent to the creation of a hole in the initial state, and an occupied final state E_f by electron in the conduction band [34].

The excitation, in our case, occurs above the InP barrier and the photocreated carriers (electrons and holes) loose their energy excess (interacting with phonons and also with other carriers) down to the edge of their respective bands, electron at the bottom of the CB and holes at the top of the VB of the InP. These carriers can either migrate to the lower energy region (in this case, the InAsP layer) or recombine in the own InP layer. In general, the diffusion time (less than a nanosecond) is shorter than the recombination time (typically ~ 1 ns). In this case, the charge transfer is more efficient than the recombination. Those falling into the potential well relax energetically (by scattering with carriers, phonons or impurities), passing through excited states and finally reaching their ground states. Usually the scattering by phonons is the most efficient process, with a scattering time of around picosecond, when the excitation intensity is relatively low, and this scattering time is smaller than the recombination time of the carriers in the excited states of the well. Therefore, the optical emission of the excited states only occurs at high temperature or at a high excitation regime when the probability of filling these states increases. When the carriers reach the ground state of the heterostructure and there are no more low energy states to loose energy, they will have enough time to recombine radiatively by emitting photons. Therefore, in heterostructures the optical emission is dominated by the lowest energy of the QW rather than the excited states and the barrier layer states.

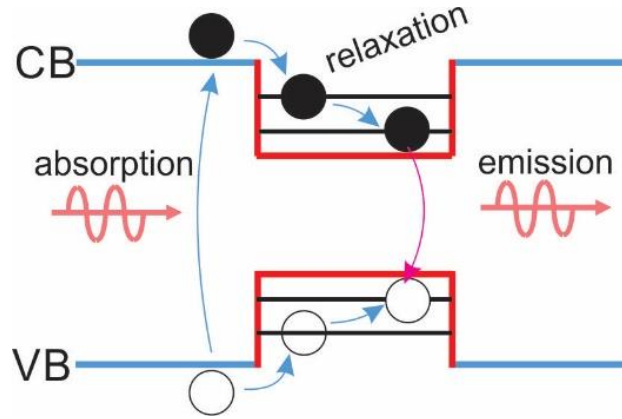


Figure 15. Potential profile of a QW. The long blue and pink arrows represent the absorption and emission process, respectively. While the short blue arrows represent the relaxation of the electron or hole into the QW energy levels.

The optical transition between the CB and VB will only be possible between these bands if the selection rules allow them. This transition can be determined by the quantum mechanical transition rate $W_{i \rightarrow f}$, for exciting an electron in an initial quantum state $|\psi_i\rangle$ to a final state $|\psi_f\rangle$, which is given by Fermi's golden rule [34]:

$$W_{i \rightarrow f} = \frac{2\pi}{\hbar} |M|^2 g(\hbar\omega)$$

The transition rate thus depends on two factors, the matrix element M and the joint-density of states $g(\hbar\omega)$. The matrix element describes the effect of the perturbation caused by the light wave on the electrons and is given by,

$$M = \langle \psi_f | H' | \psi_i \rangle ,$$

where H' is the perturbed Hamiltonian. In the envelope function approximation [35], the wave functions $|\psi_\alpha\rangle$ in heterostructures can be described as the product of an envelope function $|f_\alpha\rangle$ and a Bloch function $|u_\alpha\rangle$ having the periodicity of the crystal lattice and atomic orbital wave function, then $|\psi_\alpha\rangle = |u_\alpha\rangle |f_\alpha\rangle$. The perturbed Hamiltonian is usually described in the dipole approximation, $H' = -\hat{e} \cdot p$, where \hat{e} is the unitary vector that shows the direction of the electric field of the radiation and p is the electric dipole moment. Applying into the Fermi's golden rule to the initial and final states, and including the perturbed Hamiltonian, we finally get

$$W_{i \rightarrow f} \propto |\langle f_c | \langle u_c | \hat{e} \cdot p | u_v \rangle | f_v \rangle|^2 = |\langle u_c | \hat{e} \cdot p | u_v \rangle \langle f_c | f_v \rangle|^2$$

The c and v index, represent the CB and VB respectively. The $\langle f_c | f_v \rangle$ term is only related to the envelope function of the heterostructure known as the parity term enabling the optical transition possibilities with the same symmetry from the envelope function, i.e., electron and hole may have same parity for interband transition. The term that contains $\hat{e} \cdot p$, represent the polarized light along the different axis and coordinates (circular, linear). For III-V semiconductors, the latter reflects the Bloch function of the VB (p -orbital), since the CB states presents symmetric wave function, s -orbital. The heavy and light holes at the top of the VB in the ZB crystals present different wave function polarizations. Therefore, they depend on the direction of the electric field for appropriate heterostructures direction. Similarly, bands A, B and C of WZ crystals also present different Bloch function polarization. In principle, A and B present same wave function along the basal plane of the hexagon (p_x and p_y , see section 2.3), while the C band is along the Z -axis (p_z). Therefore, the optical transition of WZ crystal depends on the crystal orientation. In our NWs, which are supposed to be WZ crystals, the Z -axis is along the wire resulting in an optical transition of the band A and B polarized perpendicular to the wire, while C band is polarized along the wire.

Chapter 3

Sample preparation and Experimental Setup

3.1 Samples description

The samples are semiconductor nanowires grown by the VLS (*vapor-liquid-solid*) method in a CBE (*chemical beam epitaxy*) system at the DFA-IFGW by Prof. Mônica A. Cotta and her PhD student Douglas S. Oliveira. We used Au-NPs as catalysts and they were deposited onto the GaAs (001) substrate. The samples investigated in this work are InAsP alloy NWs and InAsP/InP heterostructured NWs. They were grown under high density of Au-NPs in order to have relatively large amount of nanowires to increase the photoluminescence signal for ensemble of NWs measurements, mainly for alloy NWs samples where the optical emission wavelength is longer than 1 micrometer and the detector efficient is very low. Additionally, they were grown at long deposition time to obtain large size of NWs, over hundred nanometer of diameter and several microns long. Our samples were grown in a way that favors the growth of WZ phase along the [0001] direction.

As the diameter of the nanowires used here is much larger than the Bohr excitonic radius in these materials, which is in the order of 10 nm (for *InP*) to 35 nm (for *InAs*), the confinement in the radial direction is negligible. It is important to mention that the nanowire diameter grown by VLS roughly follows the diameter of the Au-NP. However, the lateral epitaxial growth discussed above increase the diameter. Our typical Au-NP size ranges from 2 to 20 nm, and close to the NPs the diameter is around the effective Bohr radius. But far away from the top the diameter is much larger and the lateral confinement becomes negligible. This fact, on the other

hand, can be important for carrier confinement in heterostructures. It is expected that NWs have cone-like shape due to the lateral growth. We observe two regions called A and B, where the former contains catalyst InAsP layer, which is like a cylinder shape QD considering that the diameter (NP size) and height are around the Bohr radius. The latter, contains only non-catalyst InAsP epitaxial layer, which is like a lateral QW (cylindrical QW) where the InAsP thickness is a few monolayers. We would expect that the QD optical emission is a single line in the photoluminescence spectrum. In contrast, the lateral QW is a broad emission band due to the superposition of several sharp lines arising from the localized states in the QW due to the interface roughness and alloy fluctuation.

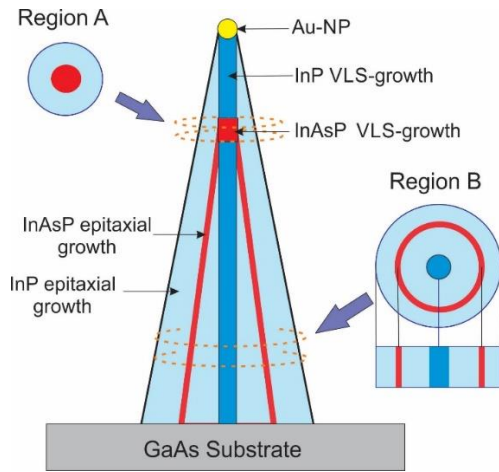


Figure 16. Cone-like structure of the InAsP/InP NW. The regions A and B represent the transversal cut around the top and bottom, respectively.

The first set of samples consists of a ternary alloy of InAsP and the growth parameters are described in Table 3. The **InAsP-alloy** is a combination of InAs and InP, whose energy gap is between the energies of these two binary (~ 0.45 to ~ 1.45 eV in the WZ phase). Table 3 shows the samples CBE3109, CBE3110 and CBE3111 with different concentrations of P or As, changing both the flux of PH_3 and AsH_3 . Also, for each alloy composition, different samples were grown changing the sizes of Au-NPs of 2, 5 and 20 nm.

The second set of samples are NWs of InAsP/InP **heterostructures**. They are shown in Table 4. The InAsP alloy was introduced into InP with three different times deposition, but simultaneously and grown with the same conditions of the sample CBE3110 of Table 3. For each InAsP growth time, we used three different NP sizes - 2, 5 and 20 nm. The third set of samples are listed in Table 5. They were grown with the same condition of the second set of

samples, but with longer InAsP growth time. For these samples we used 5nm size NPs, but bought in two different years, 2011 and 2013, and they are denoted by 2011 and 2013.

Set 1 Alloy InAs_{1-x}P_x		
CBE3109	$PH_3=30\%$	$AsH_3=5\%$
CBE3110	$PH_3=30\%$	$AsH_3=2\%$
CBE3111	$PH_3=50\%$	$AsH_3=2\%$

Table 3: List of InAsP-alloy nanowire samples grown with different PH_3 and AsH_3 flux. In each alloy, three other different NWs with Au-NPs size of 2, 5 and 20 nm were grown.

Set 2 Heterostructure InP – InAsP – InP	
CBE3115	$\Delta t=2s$
CBE3116	$\Delta t=5s$
CBE3117	$\Delta t=10s$

Table 4: List of nanowire samples of InAsP/InP heterostructures grown with different deposition times of InAsP. The alloy concentration is equivalent to the sample CBE3110. Similar to the 1st set, for each deposition time of the alloy three different Au-NPs sizes of 2, 5 and 20 nm were used. The InAsP was introduced at the time corresponding to the 2/3 of the total NW growth time.

Set 3 Heterostructure InP – InAsP – InP	
CBE3148	$\Delta t=10s$
CBE3149	$\Delta t=20s$
CBE3150	$\Delta t=40s$

Table 5: List of nanowire samples of InAsP/InP heterostructures grown with different deposition times of InAsP. The alloy concentration is equivalent to the sample CBE3110. For each deposition time of the alloy two different source of Au-NPs were used with 5 nm size, bought in 2011 and 2013. The InAsP was introduced at the time corresponding to the 1/2 of the total NW growth time.

Figure 17 depicts the typical SEM image of sample CBE3117, heterostructure NW. The NW has needle-like shape, with ~8 μm long and ~100 nm size at the bottom. The diagram of the NW shape shown in Fig. 16 is based on this image (EDS, SEM and TEM measures not shown here, are in great accordance).

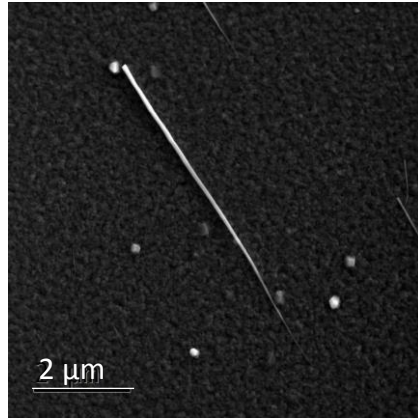


Figure 17. SEM (Scanning electron microscope) image of a NW, which presents a needle-like shape.

3.2 Photoluminescence Spectroscopy

The photoluminescence (PL) technique is a light emission process of a material, previously absorbed by a medium the incident light. The process was described in the last chapter in the optical process. For this work, we use a macro-PL and micro-PL (μ -PL) experiments, both setups were carried out in the “Group of Optical Properties” (GPO) of the Institute of Physics "Gleb Wataghin". We studied the ensemble of NWs and single NWs samples with the macro-PL and micro-PL setup correspondingly.

3.2.1 Macro-Photoluminescence

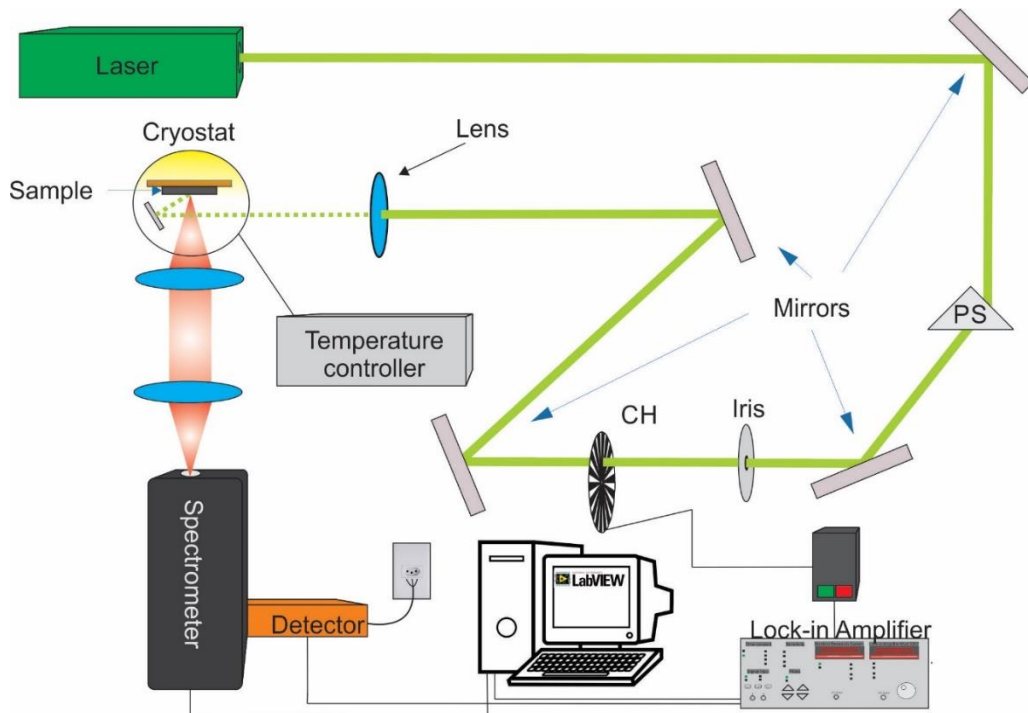


Figure 18. Schematic diagram of the macro-photoluminescence technique.

The technique of macro-PL spectroscopy or simply PL allows us to investigate optical aspects of large length scale in the samples, over several tens micrometers. In our case, this technique was used to measure ensemble of NWs. A diagram of the setup is shown in Figure 18. It includes a laser, 488 nm line, a Janis liquid helium cryostat, a spectrometer model Triax 320 Jobin-Yvon, with grating of 300, 600 and 1200 lines/mm in conjunction with a CCD Jobin Yvon Camera and InSb or Si photodetector (depending on the sample emission range), a Lock-in Amplifier Model 5302 EG&G, a chopper, an attenuation filter, an iris, a triangular prism (PS) for laser line filter and a set of mirrors and a computer for the data acquisition. The PL measurements were performed under different laser power and sample temperatures.

3.2.2 Confocal micro-photoluminescence (μ -PL)

We use the micro-PL to analyze objects with micro or nano-scale size. In our group, we use it to study single QDs and NWs, and also in a special measurement requiring high excitation intensity. A schematic diagram of a micro-PL setup is shown in Figure 19. It consists of a laser, 532 nm line, a "finger cold" helium cryostat (Cryovac) mounted on a motorized XY motion platform (Newport) controlled by computer, a homemade microscope, a $\frac{1}{2}$ m spectrometer (Andor-Shamrock, model SR500) with gratings of 300, 600 and 1200 lines/mm coupled with a Peltier cooled Si-CCD camera (Andor, model IDUS). The microscope contains a 50x NIR objective lens with a long working distance (Mitutoyo), ~ 10 mm, a CCD Sony Camera to image the sample and a filament lamp that provides white light to enable viewing the sample. Two retractable pellicle are used as beam splitter for the CCD and the lamp. The beam splitter (BS) to split the laser beam and the luminescence is a 532 nm edge-filter (Iridian). The luminescence is focused on a 200 μ m diameter multimode optical fiber to send it to the spectrometer. Therefore, the optical fiber works as a confocal micro-PL.

The samples used for micro-PL measurements are NWs transferred from the as grown sample to another substrate by mechanical process. The substrate is an Al coated GaAs where the Al thickness has several micrometers. The Al film is to increase the optical contrast between nanowire/substrate, as well as to avoid the luminescence signal from GaAs.

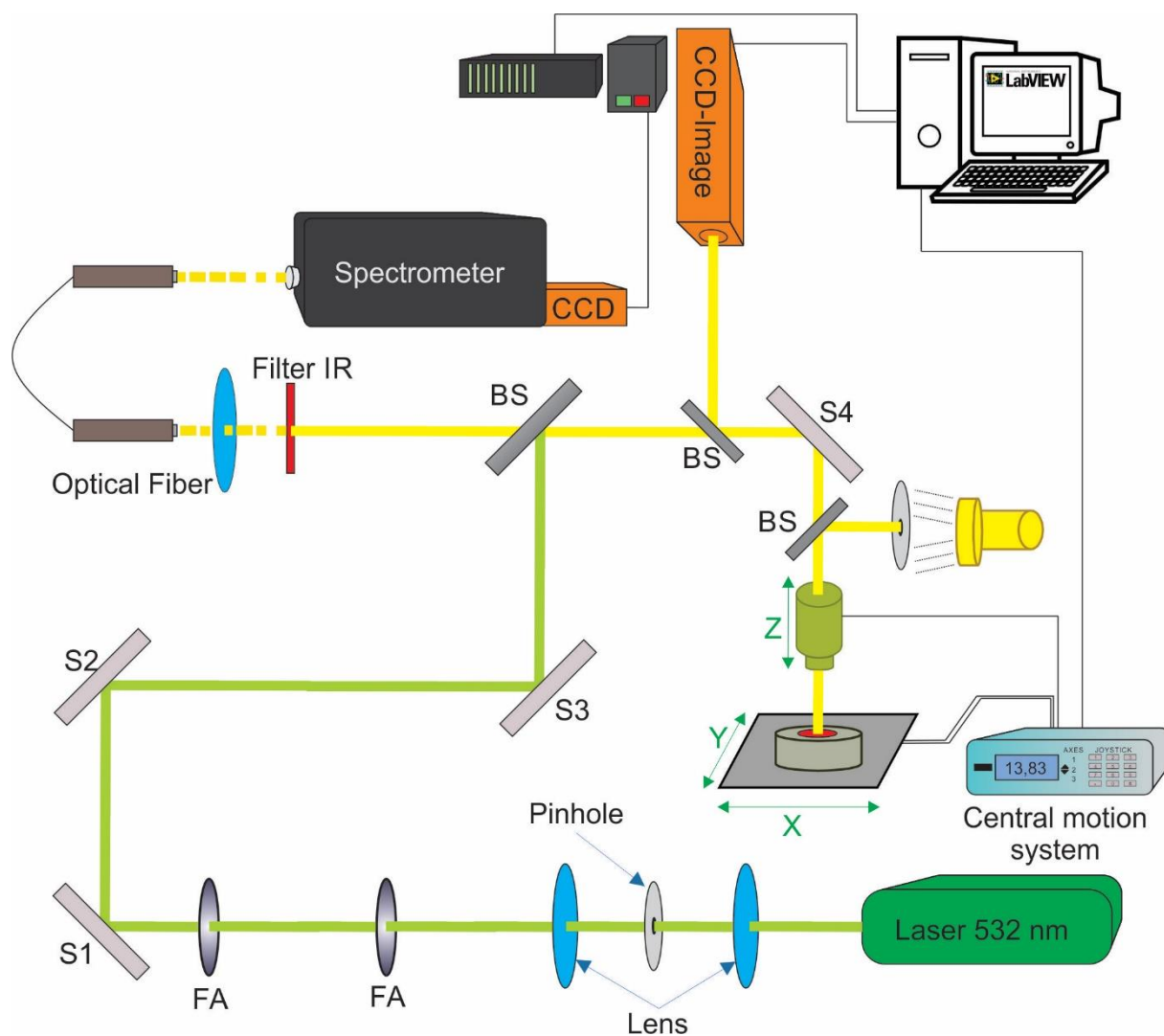


Figure 19. Schematic diagram of a micro-PL setup.

Chapter 4

Results and Discussion

In the previous section, we explained two different kinds of samples, one called the “**Alloy** samples”, and the other, the “**heterostructure** samples”. To facilitate the understanding of our results, they will be presented in the same order they were introduced and a discussion will follow each of them.

4.1 PL in Alloy Samples

We investigated three samples (A= CBE3109, B= CBE3110 and C= CBE3111) with different P (or As) compositions, changing the PH_3 and AsH_3 flux, and each sample was grown with 3 different Au-NP size, as shown in the Table 3.

Firstly, before presenting PL results we will introduce the results of structural analysis by using scanning electronic microscopy (SEM), including the measurements of the alloy composition with the energy-dispersive X-ray spectroscopy (EDS), both measurements performed by Prof. Luiz F. Zagonel and his Master Student Bruno Cesar in the LNNano Brazilian Nanotechnology National Laboratory in Campinas. The SEM images of all three samples are presented in Figures 20 – 22.

Figure 20 shows the SEM images of sample A (three different Au-NP sizes) with two different magnification. The left images are used to estimate the density of nanowires (quantity of nanowires per area), where present lower magnification or higher NW density. The images for Au-NPs with 2 nm (Fig. 20a) and 5 nm (Fig. 20b) show that the NWs present very similar morphology and, surprisingly, an unusual *tower-like* shape, while for 20 nm (Fig. 20c), a typical *needle-like* shape. In all samples, the NWs are few micrometers long, shorter than heterostructures NWs presented in Fig. 17, and the diameter size according to its scale at close

to the bottom is very similar ~ 200 nm, and they present dominantly WZ phase. In addition to the NWs, several nanostructures with ~ 200 nm size are observed at the substrate surface. They were not analyzed in details, but they are attributed to the epitaxial ZB phase nanostructure, since they are typical epitaxial growth structure. The population of NWs for each samples is quite different, for instance, the highest population for set of samples A in Fig. 20 (see right column) is for Au-NPs 5 nm with $3 - 4$ NWs/ μm^2 , while the lowest for 2 nm with $0.15-0.20$ NWs/ μm^2 , and for 20 nm samples, $0.5-1$ NWs/ μm^2 . The average length of the different NWs are ~ 1.5 μm for the Au-NPs 2 nm and ~ 2.0 μm for the 5 nm and 20 nm samples.

For sample B and C, the results are basically very similar to those for the sample A. Figures 21 and 22 show the SEM images of B and C for three Au-NPs sizes, respectively. The NWs also present peculiar tower-like morphology for Au-NP of 2 and 5 nm, however, in the samples C it is also present an additional needle at the apex. For the Au-NP of 20 nm the morphology again are in both cases a needle-like shape. The NWs population in the set of sample B has a similar result to the sample A, 2 nm sample presents low NW density, $0.1-0.5$ NWs/ μm^2 , and the highest population is also 5 nm sample, with $2-3$ NWs/ μm^2 , and the 20nm sample, $1.5-2$ NWs/ μm^2 . The average length in each case for Au-NPs of 2, 5 and 20 nm are approximately 2.0, 3.2 and 1.0 μm , respectively. For sample C (Fig. 22), 5 and 20 nm Au-NPs present the similar population density of $3 - 4$ NWs/ μm^2 , while for 2 nm, $1.5 - 2.5$ NWs/ μm^2 . The length, on the other hand, for 2 and 5 nm samples present similar values, ~ 1.5 μm , and for 20 nm sample is ~ 1.0 μm .

Additionally, using EDS measurements (not shown here) *P* concentration of the InAsP alloy for three samples is obtained. The analysis was focused only for the samples with Au-NPs of 5 nm. The *P* concentration values are presented in the Table 6. The highest *P* concentration is obtained for C sample $44 - 52$ % while the lowest is for the A sample $5 - 12$ %, as predicted by the nominal III/V flux ratio shown in Table 3.

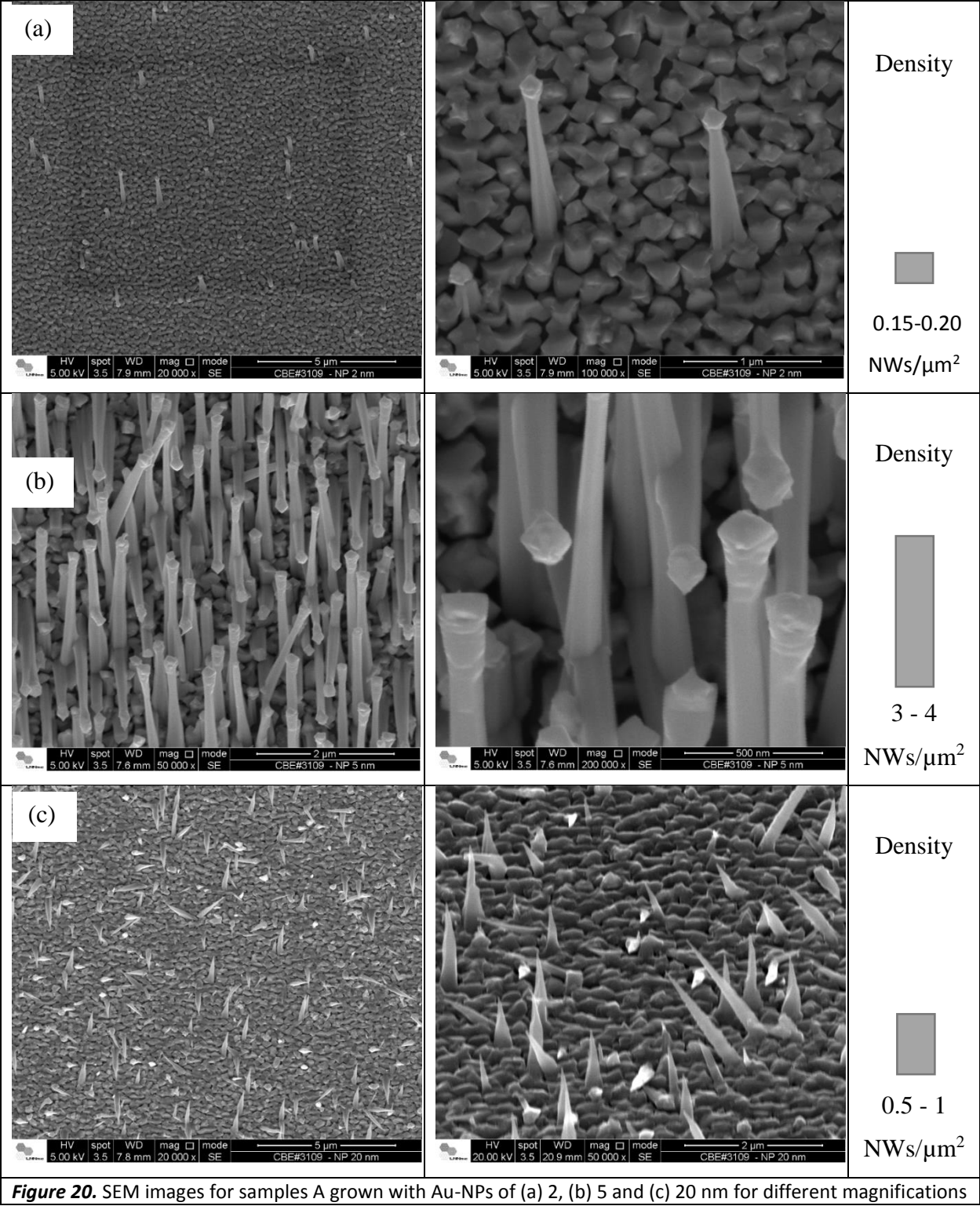
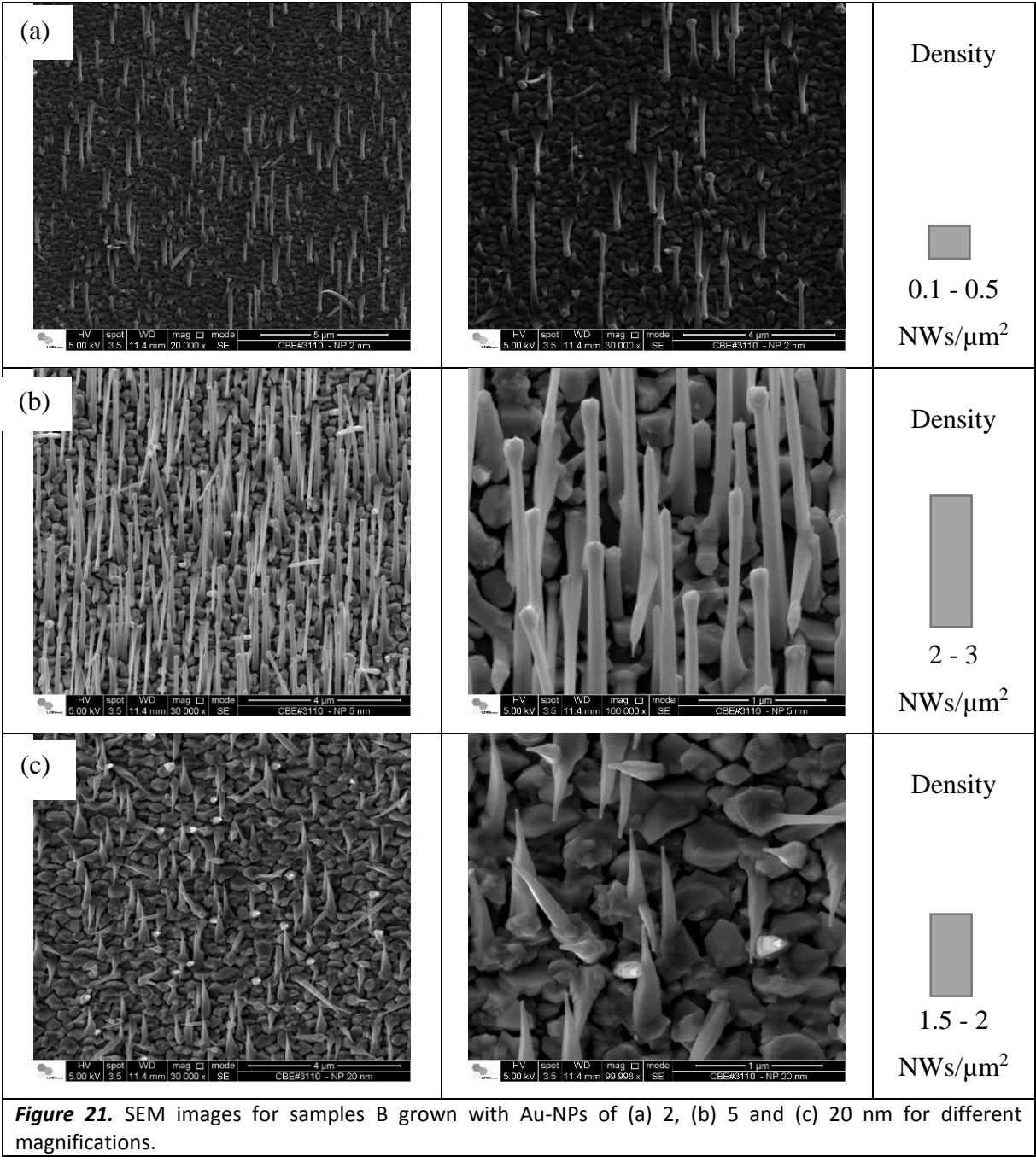


Figure 20. SEM images for samples A grown with Au-NPs of (a) 2, (b) 5 and (c) 20 nm for different magnifications



	5 nm
	$x(\%)$
A	5 - 12
B	43 - 51
C	44 - 52

Table 6: *P* concentration in % of the InAsP alloys, obtained from the EDS graphs (not shown here) for the three samples A, B and C with the Au-NPs of 5 nm.

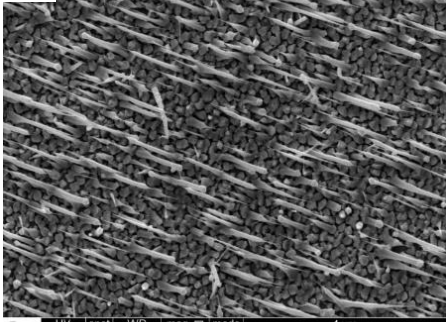
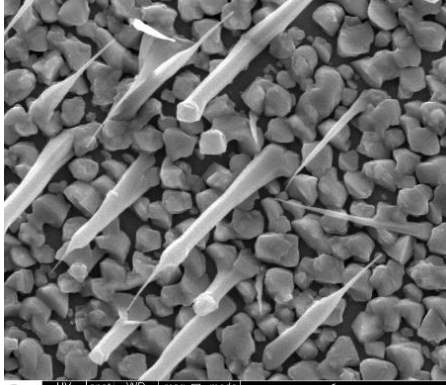

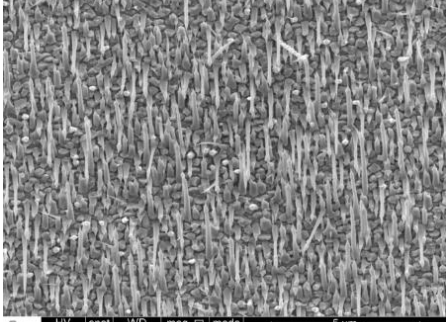
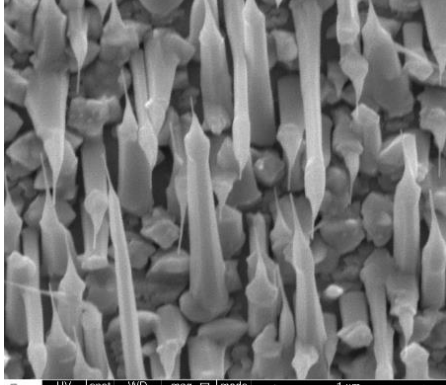

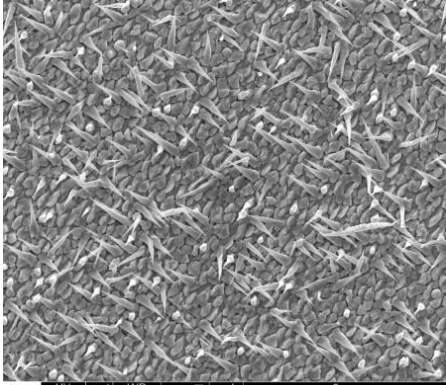
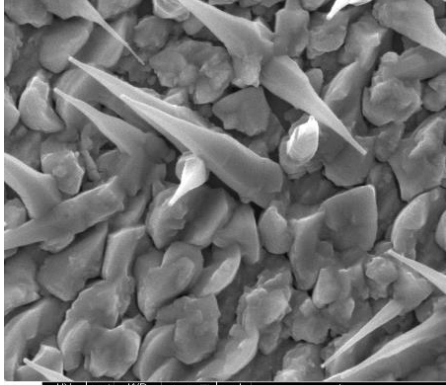

<p>(a)</p>  <p>HV 5.00 kV spot 3.5 WD 10.6 mm mag 27,518 x mode SE CBE#3111 - NP 2 nm</p>	 <p>HV 5.00 kV spot 3.5 WD 9.5 mm mag 89,017 x mode SE CBE#3111 - NP 2 nm</p>	<p>Density</p>  <p>1.5 - 2.5 NWs/μm^2</p>
<p>(b)</p>  <p>HV 5.00 kV spot 3.5 WD 10.7 mm mag 20,000 x mode SE CBE#3111 - NP 5 nm</p>	 <p>HV 5.00 kV spot 3.5 WD 10.7 mm mag 100,000 x mode SE CBE#3111 - NP 5 nm</p>	<p>Density</p>  <p>3 - 4 NWs/μm^2</p>
 <p>HV 5.00 kV spot 3.5 WD 10.7 mm mag 21,600 x mode SE CBE#3111 - NP 20 nm</p>	 <p>HV 5.00 kV spot 3.5 WD 10.7 mm mag 102,747 x mode SE CBE#3111 - NP 20 nm</p>	<p>Density</p>  <p>3 - 4 NWs/μm^2</p>

Figure 22. SEM images for samples C grown with Au-NPs of (a) 2, (b) 5 and (c) 20 nm for different magnifications.

In PL experiment, we used Ar^+ laser emission at 488 nm, He-gas continuum flow cryostat (temperature from ~ 6 to ~ 120 K), 32 cm monochromator with a diffraction grating of 300 lines/mm, whose maximum efficiency is 2 μm , coupled with an InSb detector cooled with liquid nitrogen, and the signal amplified by a lock-in amplifier. The laser beam spot on the sample is about 100 μm diameters. The PL experiments were performed in as-grown samples probing ensemble of NWs.

Based on the structural analysis discussed in previous section, the PL spectra should arise from two nanostructures, one from the catalyst WZ InAsP NWs and other from the epitaxial ZB nanoparticles grown on the substrate. Their relative PL intensity depends on the NW density that cover the nanoparticles. This fact is important to analyze PL results below.

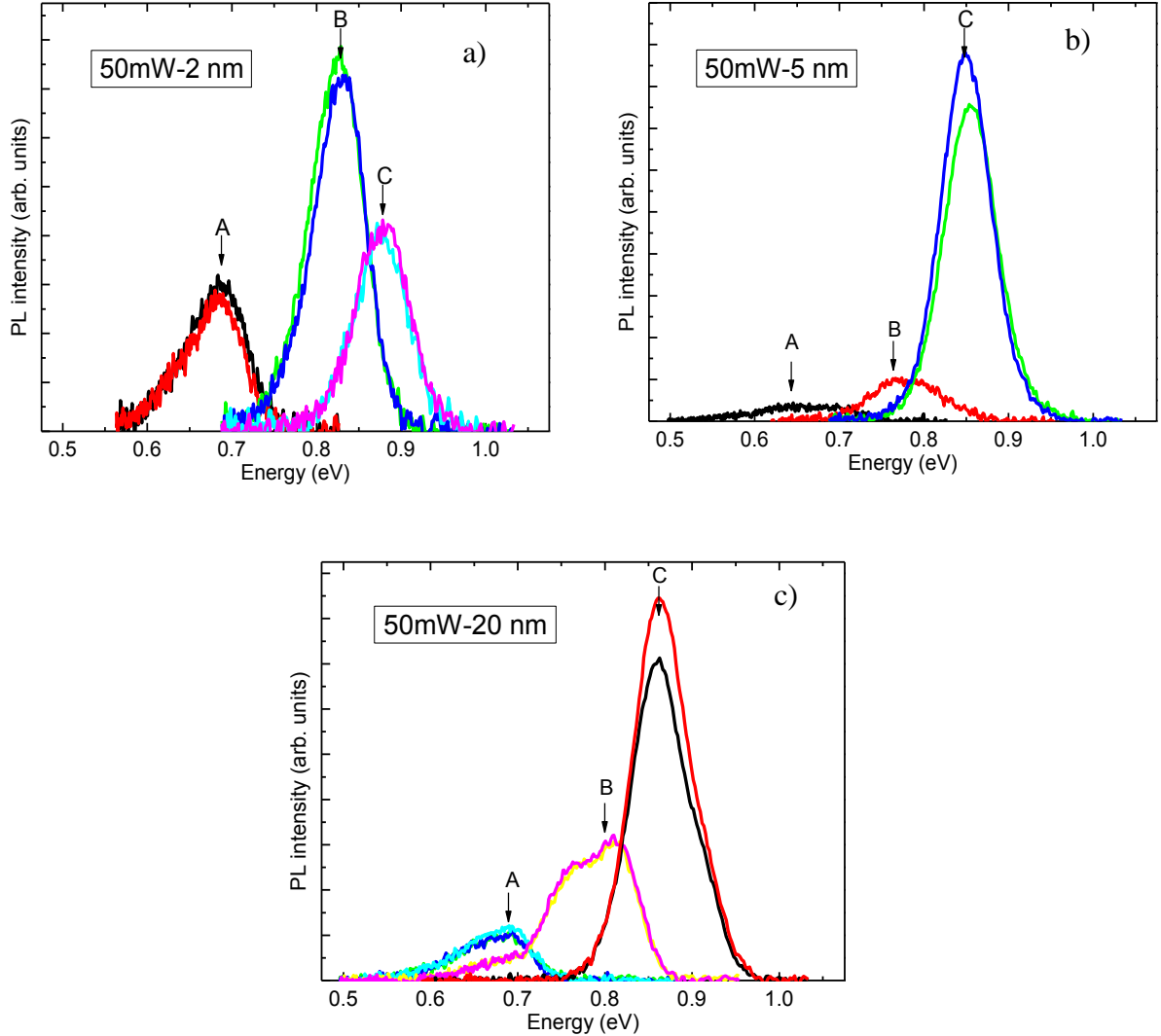


Figure 23. PL spectra at 8K of alloy NWs (samples A, B and C) carried out with laser power of 50 mW. (a) 2 nm (b) 5 nm and (c) 20 nm of Au-NPs. The number on each figure indicates the size of the Au-NPs used as catalyst, while the A, B and C on each peak correspond to the different samples CBE3109, CBE3110, and CBE3111, respectively.

Figure 23 shows typical PL spectra of the 9 (nine) samples (A, B and C and each one with Au-NPs of 2, 5 and 20 nm) using an excitation power of 50 mW. The PL spectra were organized by the Au-NP size in three figures 9a, 9b, and 9c. The PL were performed at different positions on the surface of the sample and the corresponding PL spectra of each sample are

presented in Fig. 23. We noticed very similar PL spectra in all positions, an indication that the NWs are very homogeneous.

The PL spectra of samples with different alloy compositions exhibits peaks at different energies. The PL peak, as expected, presents blue shift when we introduce more P , and it is between the InAs and InP band gap, 0.46 - 1.49 eV. The linewidth of the emission bands are very broad, around 100 meV in all samples, and in some cases it presents more than one peak, which can be related to two compositions, impurity recombination, or from two structures mentioned above, NWs and nanoparticles. The PL intensity also depends on the sample, but no systematic variation was observed, which, for instance, could be due to the NW population density variation.

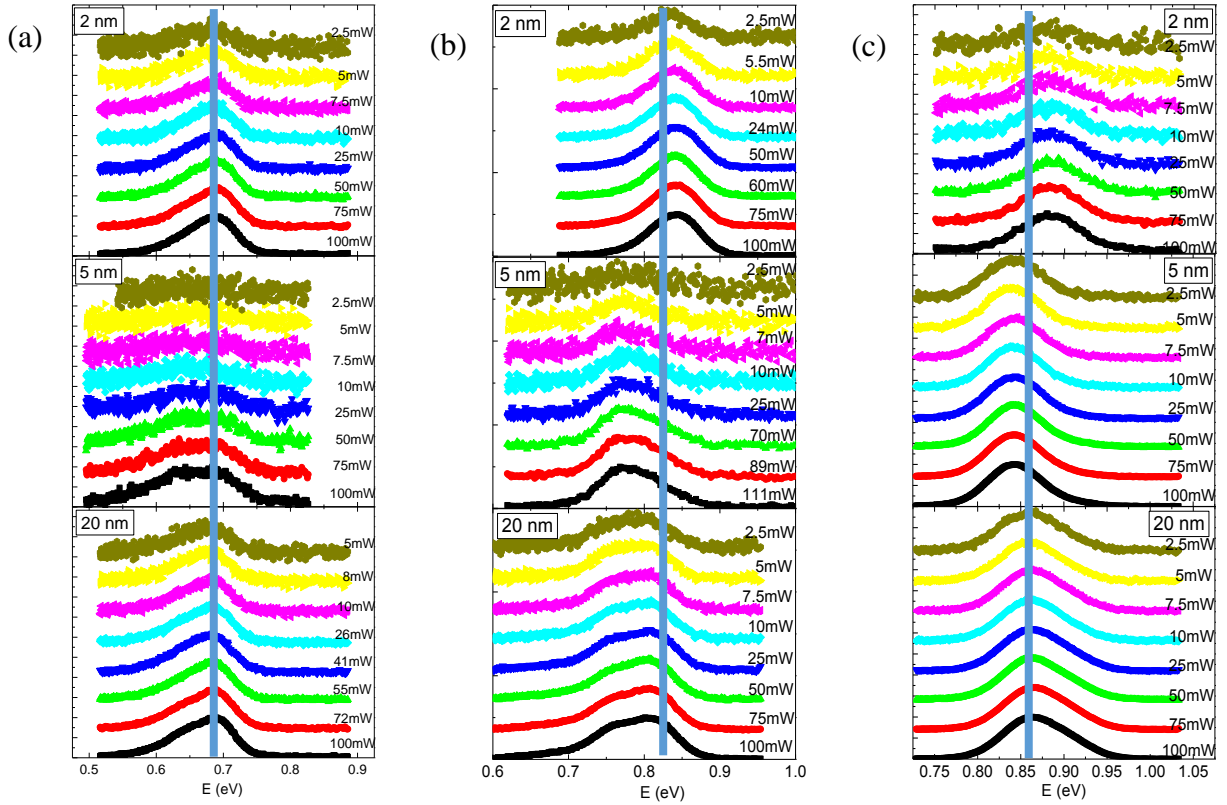


Figure 24. PL spectra at 8K of samples (a) A (b) B and (c) C as a function of the laser excitation intensity, for the three different Au-NPs sizes. Blue vertical lines corresponds the PL-peak at 0.68, 0.81 and 0.86 eV for samples A, B and C respectively.

The excitation intensity dependence of PL spectra is presented in Figure 24. The laser power was varied from 2.5 to 100 mW. The PL spectra are normalized with the peak intensity. Again, we measured all samples with different Au-NPs size, 2, 5 and 20 nm. Figure 24 presents the PL spectra in different scale ranges, because there are different emission bands peaks

position for three different alloy composition. The Fig. 24 is convenient to analyze the Au-NP size dependence of PL spectra.

For lowest P concentration sample, sample A, the PL spectra, shown in Fig. 24.a, present same main emission band at ~ 0.68 eV in all Au-NP size. In addition to this peak, all spectra show a shoulder at lower energy, which is more evident for NWs grown with 5 nm Au-NPs. Other two alloy samples, B and C, on the other hand, present distinct behavior; the peak position is different for each Au-NP size, and no systematic changing of the peak position when the Au-NP size increases. Therefore, no clear evidence of size dependence of the emission energy.

Increasing excitation intensity, the emission bands are slightly blue-shifted, less than 10 meV, and no saturation effect is observed in all emission bands, suggesting that these emission bands are not related to the impurity recombination, which usually saturates at high excitation intensity. The blue shift is likely related to the filling of the high-energy states of localized states due to the alloy potential fluctuation.

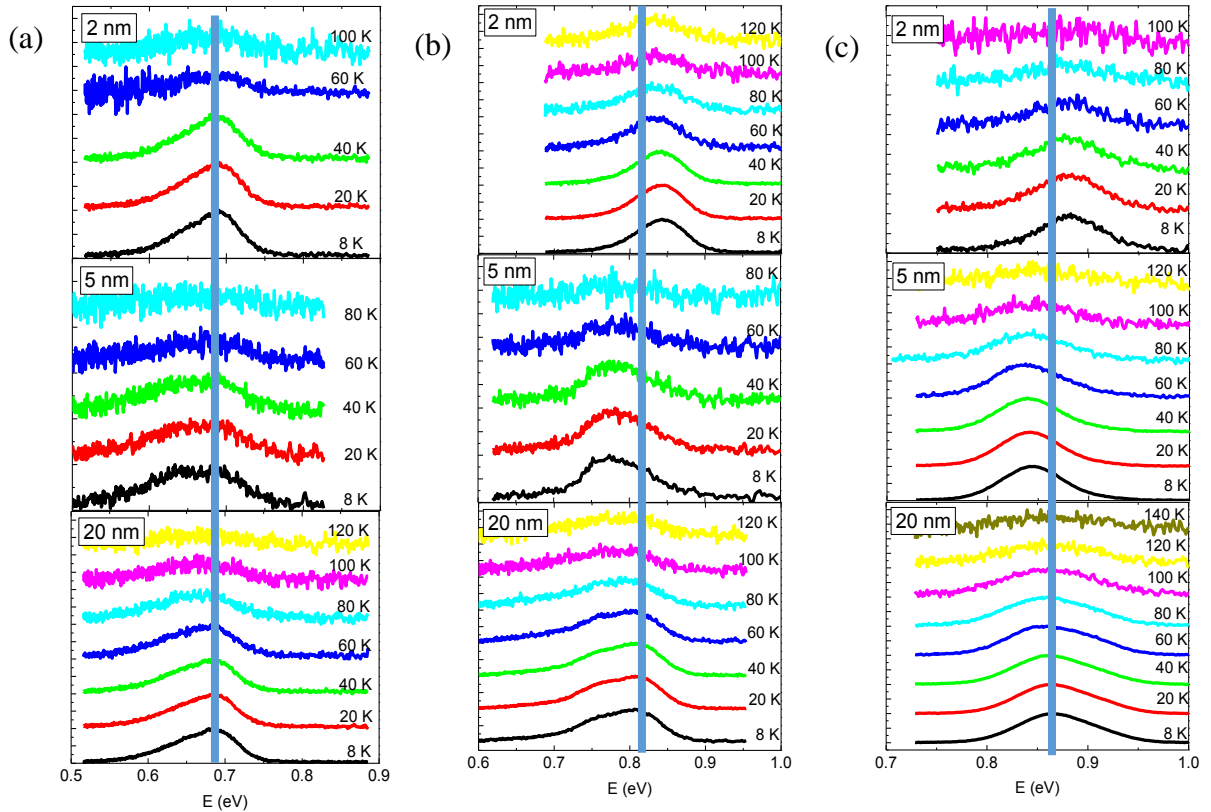


Figure 25. PL spectra vs temperature carried out with laser power of 50 mW for (a) A, (b) B and (c) C samples with three different Au-NPs sizes. Blue vertical lines corresponds the PL-peak at 0.68, 0.81 and 0.86 eV for samples A, B and C respectively.

We also investigated temperature dependence of the optical emission in these samples. The temperature was varied from 8 - 140 K (this temperature limit is where signal is less than detection sensitivity), keeping laser power of 50 mW. The normalized PL spectra are shown in Figure 25 for samples A, B and C. In all samples, the main emission bands decrease their intensity and red-shift as the temperature increases which is more evident for sample C (Fig. 25.c). The decrease of the intensity is the typical increase of the rate of the non-radiative recombination, likely, by the surface states, and the result is the decreasing of the band gap emission intensity with the increase of the temperature, as discussed in the theoretical section above.

If we assume that the main emission band is related to the band-to-band recombination of each alloy compound, we can estimate the alloy concentration based on the equation of the band gap as a function of the P concentration from the literature. Tragardh et al. [36] reported the PL peak energy versus P concentration in WZ phase InAsP alloy given by:

$$E_g(\text{InAs}_{1-x}\text{P}_x) = (1 - x)E_g(\text{InAs}) + xE_g(\text{InP}) - x(1 - x)C,$$

where E_g is the band gap, x is the P concentration and $C = 0.2 \text{ eV}$ is called bowing parameter. Using the $E_g(\text{InAs}) = 0.46 \text{ eV}$ [17] e $E_g(\text{InP}) = 1.488 \text{ eV}$ [16], the obtained values of x are presented in Table 7.

	2 nm			5 nm			20 nm		
	$\lambda [\text{\AA}]$	$E (\text{eV})$	$x(\%)$	$\lambda [\text{\AA}]$	$E (\text{eV})$	$x(\%)$	$\lambda [\text{\AA}]$	$E (\text{eV})$	$x(\%)$
A	18074	0.685	25	19269	0.643	21	18112	0.684	25
B	14683	0.844	42	15831	0.783	36	15479	0.800	38
C	14097	0.879	46	14722	0.842	42	14351	0.863	44
Table 7: PL peak wavelength and energy and P concentration x of the InAsP alloys.									

The estimated alloy composition varies from 21 to 46 %. For each sample, the composition variation for different Au-NP size is relatively small. These values can be compared with those obtained by EDS measurements shown in Tab. 6 and we noted the discrepancy between two results. In order to explain this discrepancy we take into account the

density of NWs and the presence of the epitaxial InAsP nanoparticles. We replot the PL spectra of all samples now using same scale, they are shown in Fig. 26. In the previous analysis of the PL spectra of InAsP NWs discussed above we consider that all emission bands are due to the WZ phase alloys, without considering the ZB epitaxial nanoparticles grown on the surface. For ZB InAsP alloy the composition dependent band gap energy is different than the Eq. above used for WZ phase alloy. We used here the previous work from I. V. Bodnar et al. [41] and R. L. Moon et al. [42] for ZB alloy band gap equation.

$$E_g(\text{InAs}_{1-x}\text{P}_x) = 0.410 + 0.796x + 0.200x^2,$$

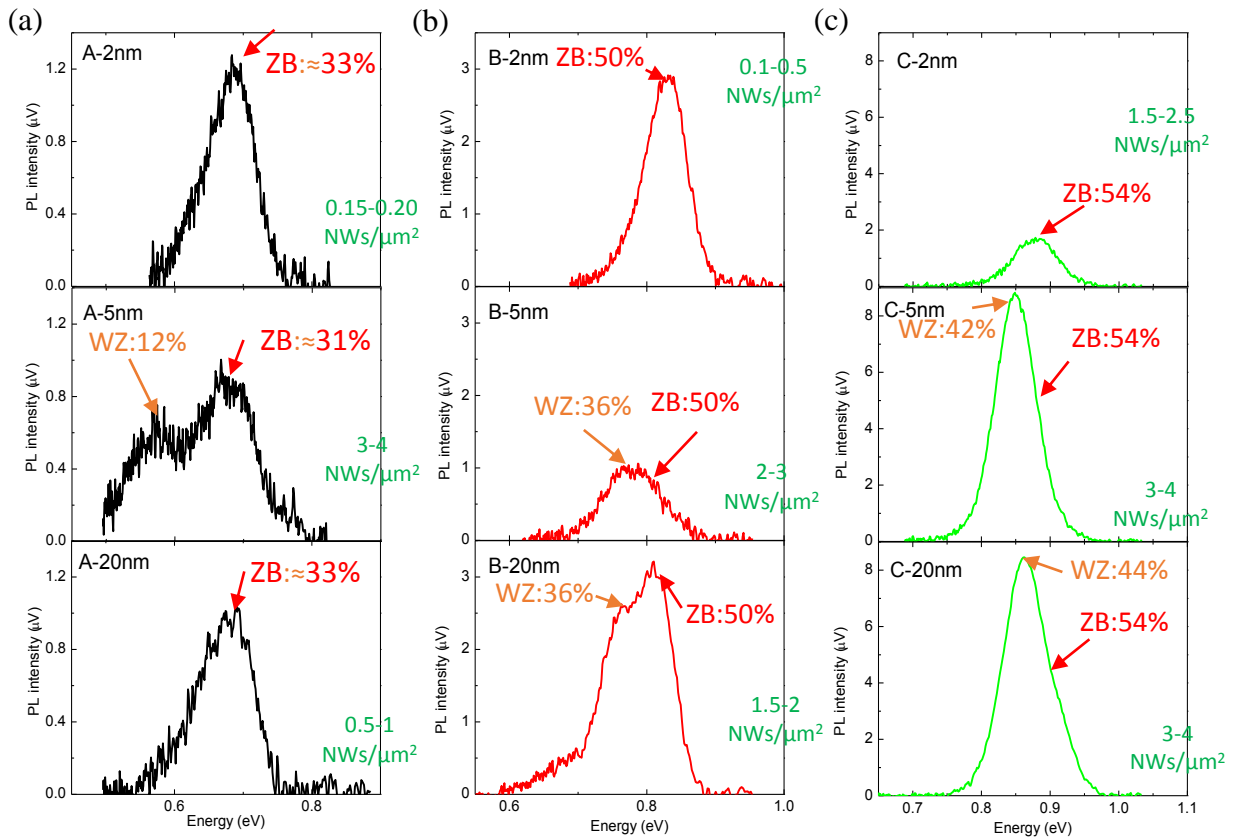


Figure 26. PL spectra carried out with laser power of 50 mW and at 8 K for (a) A, (b) B and (c) C samples with three different Au-NPs sizes. Red and orange labels and numbers represent the different P concentration situated in different peaks for WZ and ZB phase, respectively. The green numbers represent the NWs density in each sample.

Let us firstly analyze the sample A. Note that the PL spectra obtained from different Au-NPs size, shown in Fig. 26.a, present a main broad band with peak at ~0.68 eV in all three samples and a second band, at ~0.58 eV, observed only in the sample of 5nm Au-NPs. This result may be correlated to the SEM ones. For instance, the NW density (see right column of Fig. 20) is very small for 2 and 20 nm samples, below 1 NWs/ μm^2 , and relatively large for 5nm

one, 3-4 NWs/ μm^2 . Therefore, the corresponding area covered by NWs at the sample surface for 2 and 20 nm samples is much smaller than that of the epitaxial InAsP nanoparticles and for 5 nm one, the area of both is relatively similar. We are considering, in this case, only the free area of the nanoparticles that are not covered by NWs, since the presence of the NWs reduces both the optical emission and the incident beam on the nanoparticles. The PL spectra of these samples are expected contribution from both, NWs and epitaxial nanoparticles, thus the discussion based on the NW density leads to conclude that in 2 and 20 nm samples the PL spectra should be dominated by the epitaxial nanoparticles, while for 5 nm sample, by both contributions. In fact, the PL spectra of the latter show two emission bands, as expected. For the former, it is likely that the emission is related to the epitaxial nanoparticles, since the NW density is very low, as mentioned above. Moreover, the PL spectra present an asymmetry at low energy range, which is an indication of the weak emission from the NWs.

The low energy emission, at ~ 0.58 eV, can also be related to the nanoparticles with bimodal alloy composition. However, the fact that the set of sample A (2, 5 and 20 nm) was grown simultaneously, it leads to believe that all of them should have similar properties of nanoparticles, which is independent of *Au*-NPs size. Therefore, since the 2 and 20 nm samples is practically dominated by the strong emission band at ~ 0.68 eV and the 5nm sample is not, the bimodal alloy composition of nanoparticles is unlikely and the explanation that two emission bands are from WZ NWs and ZB epitaxial nanoparticles is very consistent. The quantitative analysis is also consistent, for instance, using the band gap energy equation for ZB phase alloy shown above we estimated the corresponding *P* concentration for nanoparticles shown in red color number in Fig. 26.a. for all samples, 31-33 %, and for WZ NWs in orange color corresponding to the low energy emission band for 5 nm sample, 12 %. Note that the *P* concentration of the NW alloy now is comparable to those obtained by EDS method shown in Table 6, 5-12 %.

The same analysis above is used for sample B. Similarly to the sample A, the 2 nm sample presents very low NW density (see right column of Fig. 21), 0.1-0.5 NWs/ μm^2 , suggesting that the single emission band at ~ 0.84 eV, shown in the PL spectra of Fig. 26.b, is due to the ZB epitaxial nanoparticles, where the estimated value of the corresponding *P* composition of ZB alloy is 50 % (red color in the Fig. 26.b). This also indicates that the emission band from the ZB nanoparticles in other two samples should be around 0.84 eV. Therefore, in the two emission bands shown in 20 nm sample, the highest energy one is attributed to the ZB

alloy and other lower one at ~0.77 eV to the WZ NW alloy, with estimated *P* concentration of 50 % (red color) and 36 % (orange color), respectively. On the other hand, the broad band of 5 nm sample shown in Fig. 2 makes difficult to identify precisely the ZB nanoparticle and WZ NWs. However, it may be the overlap of two type of emissions, where the ZB nanoparticle should be close to 0.84 eV and the WZ NWs at lower energy around 0.77 eV, therefore, we indicated in Fig. 26.b the same values estimated for 20 nm sample.

For the set of sample C, all PL spectra, shown in Fig. 26.c, present apparently only single emission band. Their high NW density, shown in Fig. 22, can explain this result, where the lowest one is 1.0-2.5 NWs/ μm^2 is for 2nm sample and 3-4 NWs/ μm^2 for both 5 and 20 nm samples. Note that the PL spectra of 5 and 20 nm samples present, in contrast to the samples A and B, a slight asymmetry at higher energy range, while for 2 nm sample, the shoulder is at lower energy, as observed in sample A. The shoulder at higher energy in 5 and 20 nm samples is an indication of contribution from two structures. Furthermore, the NW density of 2 nm sample is comparable to that of 20 nm sample of set B and their PL spectra are also similar. Therefore, the higher energy band of 2 nm sample and the shoulder at high energy of 5 and 20 nm samples are attributed to the ZB nanoparticle emissions, while the low energy shoulder for 2 nm sample, as well as in 5 and 20 nm ones are due to the WZ NW emissions. The corresponding *P* concentrations of them are indicated in orange and red colors in Fig. 62.c for WZ NW and ZB nanoparticles, respectively.

The PL result analysis based on the SEM result is very consistent, however, in order to identify more precisely the origin of the PL peaks further single NWs micro-PL measurements should be carried out. Nevertheless, these measurements can not be performed now in our group, since the photodetectors are not so efficient to detect the optical emissions in the large wavelength shown in these samples.

4.2 PL in Heterostructure Samples

Two groups of heterostructure NW samples were studied. The first group was grown with short InAsP deposition times (Tab. 4), while the second group, longer ones (Tab. 5).

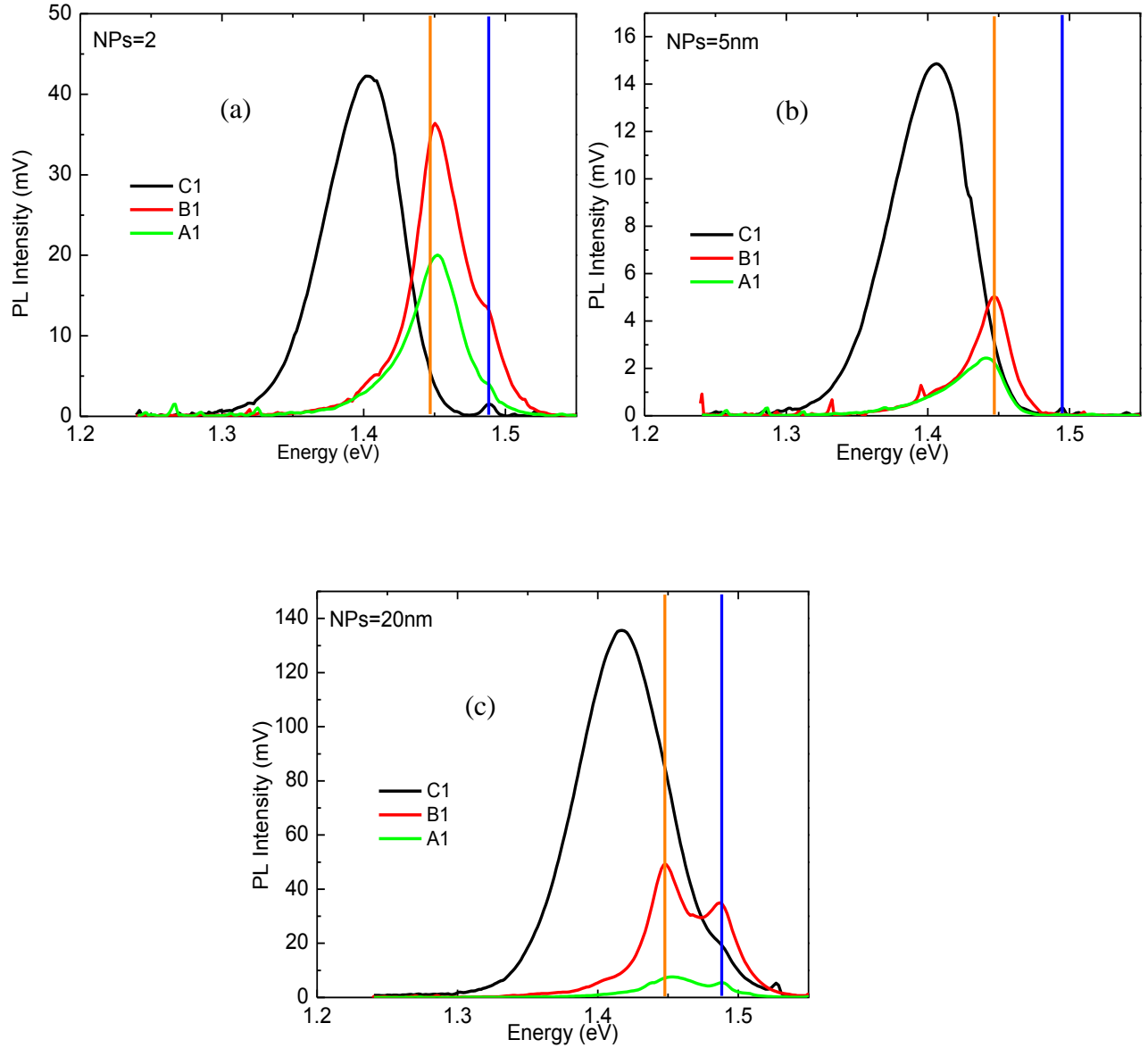


Figure 27. PL spectra at 8K of samples A1, B1 and C1 carried out with excitation intensity of 500 μ W. Samples with (a) 2 nm (b) 5 nm and (c) 20 nm of Au-NPs are presented. Orange and blue solid vertical lines corresponds to donor – acceptor (D-A) and bound exciton (BX) recombination positions of InP-WZ, respectively.

We present firstly the results for the first group of InAsP/InP heterostructure samples that are:

A1 = CBE3115 (2 s), B1 = CBE3116 (5 s) and C1 = CBE3117 (10 s).

The preliminary measurements were performed using InSb photodetector and the same setup described above for alloy NW samples in order to investigate the emission from 0.46 to 1.5 eV. However, we only observed the optical emission above ~ 1 eV, where that detector is less sensitive. Therefore, we changed the detector to LN₂ cooled Ge photodetector and using $\frac{1}{2}$ m monochromator with 600 lines/mm grating and the 442 nm line of He-Cd laser of the PL setup.

Figure 27, shows PL spectra at 8 K of three samples of first group grown with three different *Au*-NP size. In these measurements, the excitation power is 500 μ W. Basically, the PL spectra of samples grown with 2, 5 and 10 s of InAsP layer present three main peaks: one at ~ 1.49 eV, attributed to the InP WZ phase excitonic recombination; second one, at ~ 1.44 eV [15], attributed to the donor-acceptor recombination in the InP layer too [15], and the last one, at ~ 1.4 eV, attributed to the InAsP layer emission. The latter emission was only observed in the C1-sample, while in samples A1 and B1 the PL spectra of Fig. 27 do not show any emission below D-A recombination. Also, in C1-sample under low excitation intensity, broad band below it is observed, which it will be discussed later.

Figure 28 shows the PL spectra acquired at 8 K for all samples under different excitation intensity varying from 10 μ W to 2000 μ W. The PL spectra are normalized and the excitation power increases from the top to the bottom. Again, we measured samples with three *Au*-NP size. At low excitation power, as mentioned above, the PL spectra of some samples A1 and B1 also present a broad emission band below D-A recombination, apparently similar to that observed in sample C1. This emission is also close to that reported by Gadret et al. [15] attributed to the polytypism of InP NWs, i.e., presence of slabs of thin ZB layers. The ZB-WZ interface is type-II, forming a QW in the CB confining electron in the ZB layer, and its optical emission energy depends on the thickness of the ZB layer, where the typical peak position is around 1.35 - 1.45 eV, and presents large blue-shift as the excitation intensity increases, as observed in our data. Since our InP NWs were grown in the same condition to obtain mostly pure WZ phase [15], we would expect low density of ZB layers. In this case, at high excitation density this emission should saturate, as observed. Despite this band and that observed in C1 are in the same energy range, it is likely that the broad bands of A1 and B1 are related to the polytypism effect, mainly because their blue-shift (~ 30 meV results from the difference of higher and lower peaks energies) is much larger than in C1 (~ 15 meV). The small blue-shift of C1 is due to the filling effect in type I system.

When increasing the excitation intensity the optical emission is dominated by D-A and bound exciton of InP in samples A1 and B1, while in C1 we observe basically the recombination from the InAsP layer. The deeper potential well of InAsP alloy as compared to the shallow donor and acceptor levels in the InP layer explains the absence of the InP emissions in C1, since the photocreated carriers are rapidly transferred to the alloy potential well.

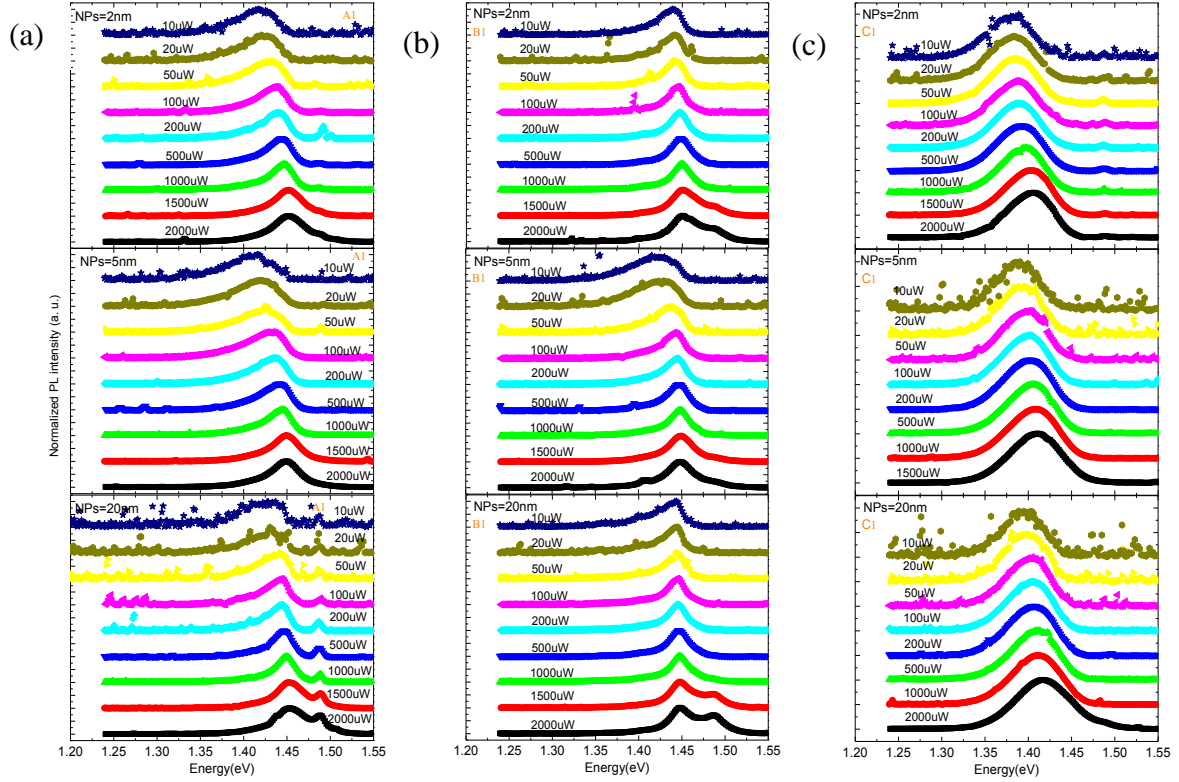


Figure 28. PL spectra at 8K of samples (a) A1 (b) B1 and (c) C1 as a function of the laser excitation intensity.

We also analyzed the optical emission of these samples at different temperatures. The results are consistent with the explanation presented above. In Fig. 29, we present the temperature dependence of the PL spectra. The emission band corresponding to the D-A and the bound exciton of InP observed in the samples A1 and B1, as expected, quench at low temperature, around 60 K. They are thermally ionized and the carriers are easily captured by the non-radiative centers such as surface states of the NWs. On other hand, the emission associated to InAsP of C1 decreases its intensity only at much higher temperatures. In this case, due to the deep potential well of InAsP layer it requires high thermal energy to excite the carriers to the InP barrier, where the carriers can move freely and be captured by non-radiative centers, such as surface states. In A1 and B1, an additional emission band appears at low energy range

than 1.4 eV at higher temperatures (≥ 60 K). For instance, this band is more evident in the sample A1 with 2 and 5 nm NPs, also in B1 20 nm NPs sample the PL possess two peaks. We believe that this emission band is related to that one observed at low excitation power in A1 and B1, discussed above.

The peak energy of all samples is red-shifted, as expected for decrease of the band gap with an increase of the temperature. However, the band attributed, e.g., to the InAsP layer of C1 is red-shifted more than the band gap variation. In Fig. 30, we plot the peak energy versus temperature obtained from the PL spectra of the Fig. 29. We also plot the band gap variation for InAsP using Varshni's model, discussed in the theoretical section 2.8.1, the values for α and β for InAsP are estimated from the linear interpolation of ZB InAs and ZB InP ones, $\alpha = 3.15 \cdot 10^{-4} \text{ eV/K}$ and $\beta = 124 \text{ K}$ (from Table 2), since for WZ materials they are not available yet. The P mean value concentration of sample B was obtained from the Fig. 26. We noticed that the theoretical band gap variation curves obtained for InAsP alloy do not so diverge as compared to those for InP for the temperature range used here.

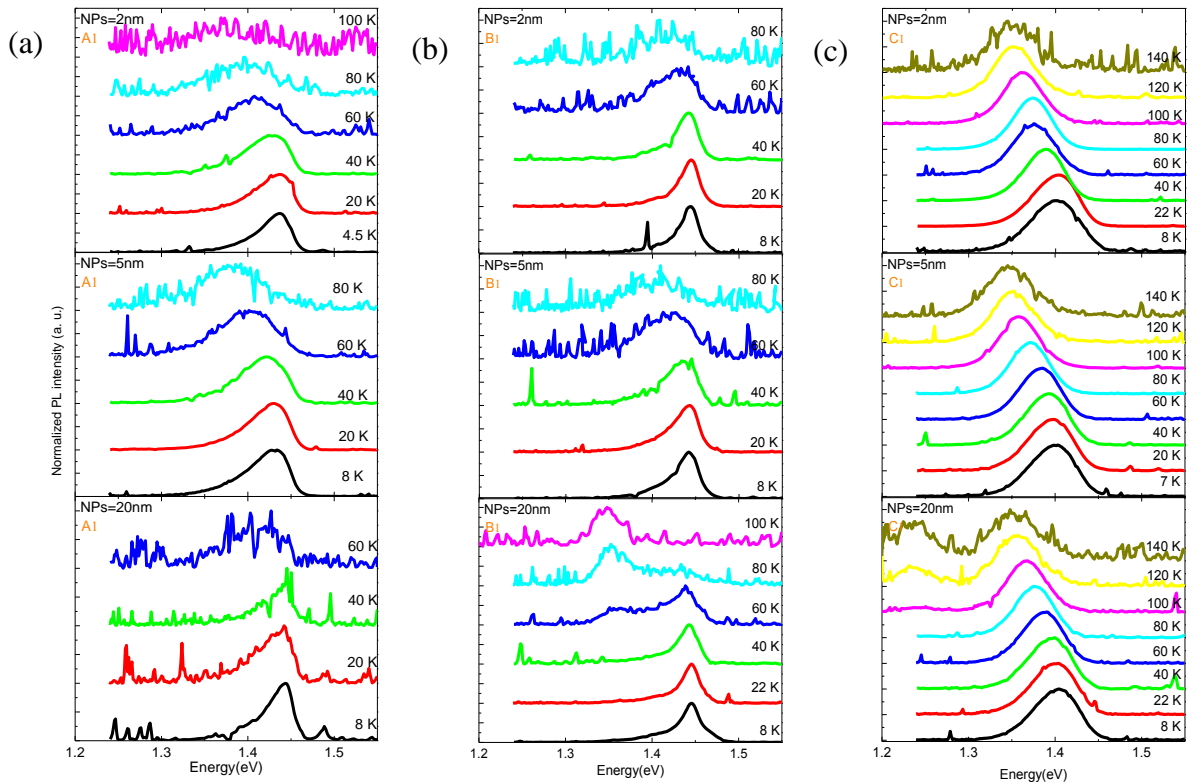


Figure 29. PL spectra of the sample (a) A1 (b) B1 and (c) C1 as a function of the temperature.

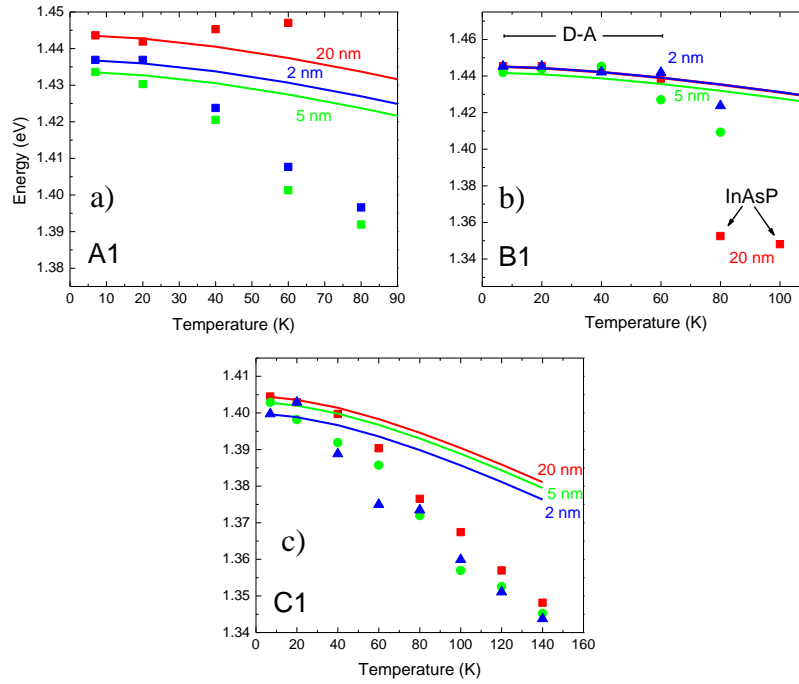


Figure 30. Energy Peak vs temperature of the PL spectra shown in Figs. 26-28. (a) A1, (b) B1 and (c) C1 samples for 2, 5 and 20 nm Au-NPs. The solid lines represent the theoretical Varshni's equation for InAsP and the symbols are the experimental data.

In Fig. 30, we plot both the D-A and InAsP-related emission peak of all samples. However, for samples A1, the PL peak positions at certain temperature are an average position due to the contribution from D-A and InAsP-related bands, where the emission bands are overlapped. The pure D-A curves for samples A1 (red curve for 20nm sample) and B1 (blue and green for 2 and 5 nm samples) follow indeed the theoretical band gap variation of InP, which is very similar curve of InAsP in this temperature range. On the other hand, the InAsP-related curves, mixed with D-A for samples A1 (2 and 5 nm) or pure for C1 (for any Au-NPs size), present larger red shift than the band gap variation, 40 meV for sample A1 (2 and 5 nm) and 55 meV for sample C1 (all three samples), which corresponds an additional variation of 35 meV from the band gap variation at 140 K for sample C1. This result will be discussed again later.

The PL spectra of **second** group of heterostructure NW samples:

A2= CBE3148, B2= CBE3149 and C2= CBE3150 (from Table 4),

are shown in Fig. 31. The samples were grown including InAsP during 10 (A2), 20 (B2) and 40 s (C2) into InP NWs. We used 5 nm Au-NP size bought in two different periods, 2011 and 2013. The samples A2 (10 s) are grown, practically, in the same condition of the sample C1 (10

s) and, indeed, PL spectra of both samples are very similar. The NWs grown at longer time of InAsP present lower peak energies, as expected, due to the confinement effect, larger volume means larger size resulting lower confinement energy. It is important to mention that the optical emission from heterostructures NWs is relatively strong, due to the relaxation of the photocreated carriers into the InAsP layer mentioned above, and it is consistent with the fact that the emission energies are between InP (1.48 eV) and InAsP alloy (~ 0.8 eV) band gap energies. This means that the emission energy can be easily tuned changing the InAsP amount or/and alloy composition and can be used for optical device application, such as for telecommunication devices.

In figure 32, PL spectra of A2, B2 and C2 samples measured at 10 K as a function of the excitation power are depicted. All spectra are normalized. For samples of A2-2011 and A2-2013 (where 2011 and 2013 indicate the acquisition period of the Au-NPs), the emission bands have a different behavior that C1 sample. When the laser power is increased, for B2 and C2 the peak position shifts to higher energy and becomes broader due to the filling effect, and in A2 ($\geq 500\mu\text{W}$) D-A (~ 1.448 eV) and bound exciton (~ 1.48 eV) of InP also appear at high laser power. While in Fig. 28, for C1 sample for higher excitation power the PL emission is only shifted to higher energies and no emission from the D-A and bound exciton of InP is observed, as for the A1 and B1 cases.

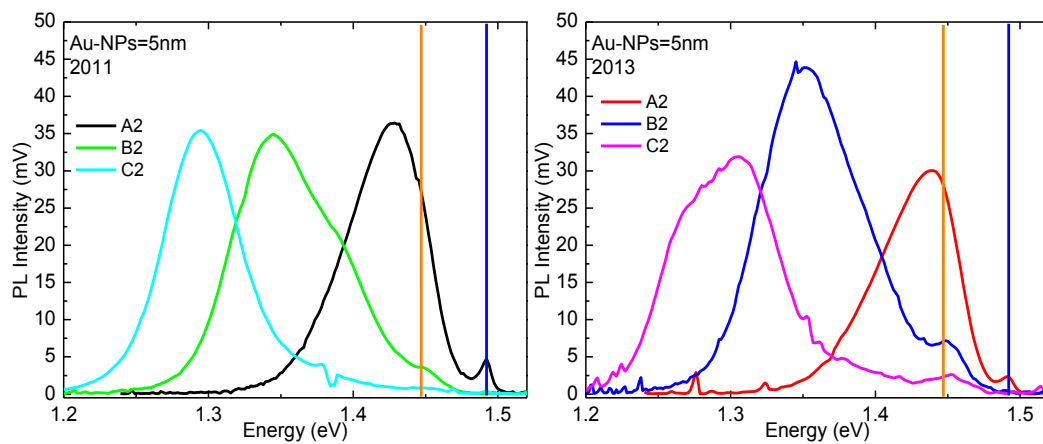


Figure 31. PL spectra at 10K of samples A2 (10s), B2 (20s) and C2 (40s) grown with Au-NPs acquired in (left) 2011 and (right) 2013, using an excitation intensity of $100\mu\text{W}$. Vertical solid lines, orange and blue, represent the D-A and bound exciton recombination in InP.

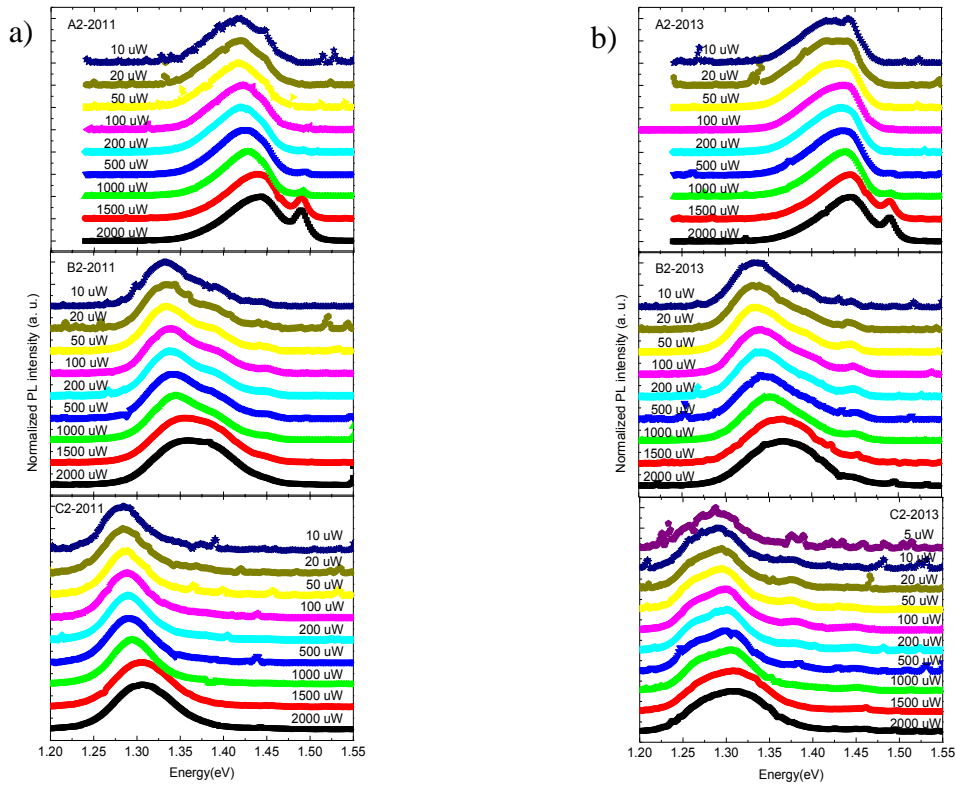


Figure 32. PL spectra at 8K of samples A2, B2 and C2 as a function of the laser power. All spectra are normalized with the maximum intensity. Left panel a) shows the spectra for samples grown with Au-NP acquired in 2011, and the right one, b) in 2013. The laser power increases from top to bottom.

Increasing the sample temperature, we observed interesting behavior due to the effect of the carrier dynamics. The PL spectra versus temperature are shown in Figure 33. The typical behavior of the PL spectra, such as red-shift and decrease of the intensity (not shown in the figure, since the spectra were normalized) when the temperature increases is observed, related to the band gap variation and the increase of the carrier capture rates by non-radiative centers, respectively. The remarkable result is more visible when we follow the PL peak energy versus temperature shown in Fig. 34. In this figure, we also included the results from the sample C1 (from first group of heterostructures samples, 10 s), to compare with the data from A2, and the theoretical curves based on the Varshni's equation [28, 29]) of the band gap energy variation with the temperature. Note that the red-shift in the samples C1 and A2 is more pronounced as compared to other two samples and also to the band gap variation. The PL peaks from the samples B2 and C2 follow practically the band gap.

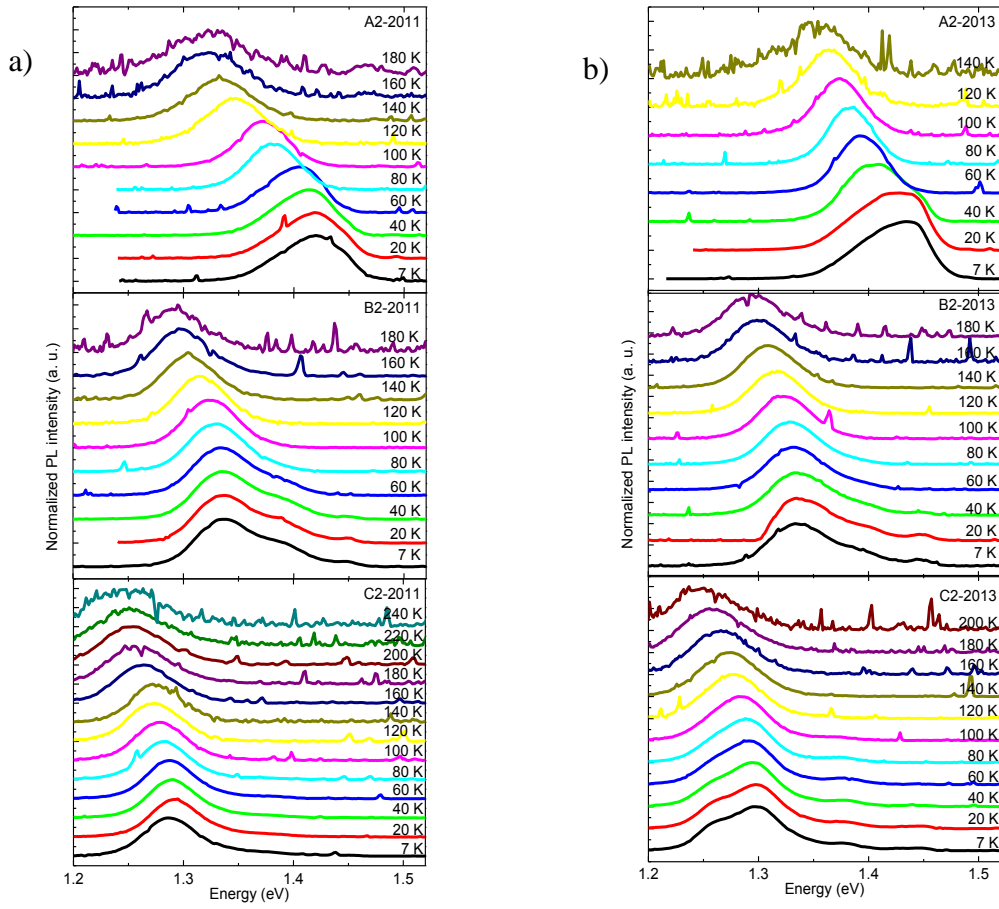


Figure 33. Normalized PL spectrum at 100 μ W of heterostructure NWs measured at different temperatures. (a) A2, B2 and C2 with Au-NPs of 5nm/2011, (b) A2, B2 and C2 with Au-NPs of 5nm/2013.

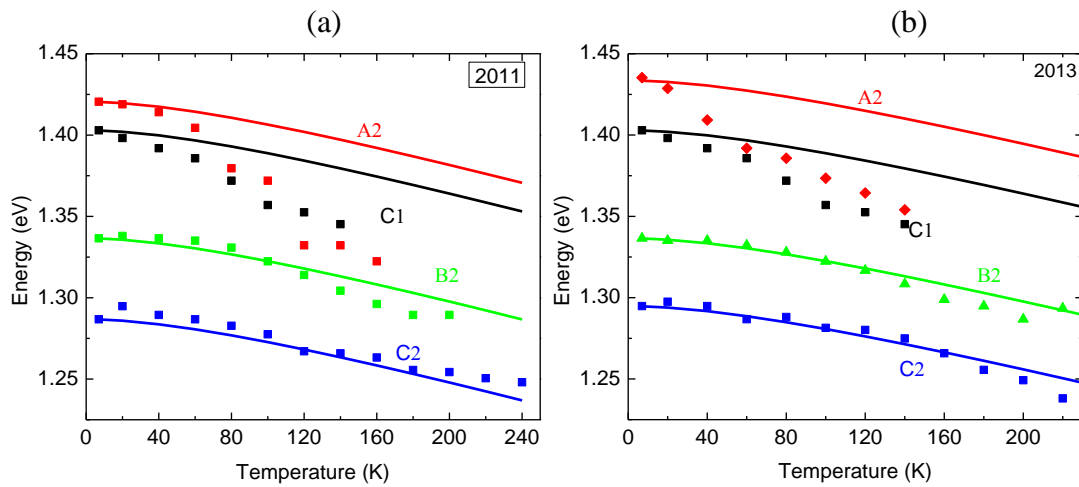


Figure 34. PL peak energy vs temperature of samples A2, B2 and C2 with (a) Au-NPs 5 nm/2011 (b) Au-NPs 5 nm/2013. The data from sample C1 were also included. The solid lines represent the theoretical Varshni's equation for InAsP and the symbols are the experimental data.

The distinct behavior of the PL spectra obtained between samples grown at 10 s and higher time samples, 20 and 40 s, can be related to the carrier dynamics and explained by the model discussed in previous section.. In heterostructures systems, where contain localized states, the carriers can be thermally activated and migrate between localized states through the continuum states. Therefore, this effect depends on the temperature and the localization energies. If the deepness of the potential well of the localized state (see Fig. 12 of previous section) is much larger than the thermal energy no carrier transference occurs, in this case, the emission band follows the band gap variation. This can be the case of the result observed in samples B2 and C2. On the other hand, if the thermal energy is larger than the localization energy deepness the carrier transference can occurs, which is the case of the samples C1 and A2. In our system, InAsP layers create localized states and the continuum states may be the InP barriers. For 10 s samples, the InAsP layer is very thin and its localized states are shallow enough to thermally excite the carriers to the continuum states of the band edge of InP barrier and suffer large red-shift of the net optical emission, more than band gap variation, as observed in C1 and A2. While for 20 and 40 s samples, the InAsP states are much deeper than the thermal energy used here, therefore, the peak position follows the band gap variation. Despite the consistence of the explanation above it is not clear if there is continuous states in InAsP layer, as in QWs, or wetting layer in self-assembled QDs systems. However, the presence of the strong localized states is corroborated by the results observed in micro-PL experiments below, where the PL spectra show sharp peaks very similar to the QD emissions observed by M. Tchernycheva et al. [9] and Tateno et al. [10].

4.3 μ -PL in Heterostructure Samples

The μ -PL experiments were performed at low temperature in a cold-finger He cryostat, excited with a solid-state laser with wavelength 532 nm, 0.5 m monochromator with 600 l/mm blaze grating coupled with a Peltier cooled CCD Si detector (Andor). The PL setup is also composed by a homemade microscope and a 50X objective lens (Mitutoyo) with a working distance of 10 mm, suitable for optical measurements with He cryostat. A schematic diagram of the experiment is shown in the Fig. 19 of previous section.

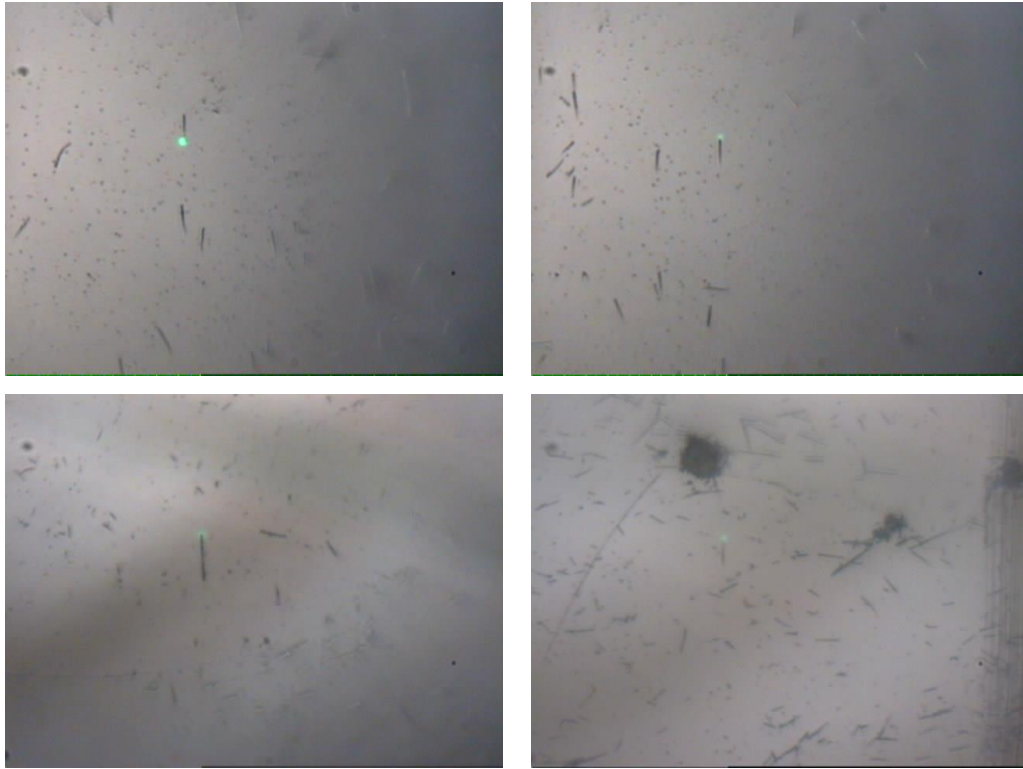


Figure 35. Typical optical microscopy images of our samples used in μ -PL experiments. The green point indicates the laser spot.

As mentioned before, in μ -PL experiments we transferred the NWs from the as-grown sample to the *Al* coated GaAs substrate. The typical optical image of the NWs on the *Al* film is shown in Fig. 35. The green color indicates the laser spot that is placed at one of edge of the analyzed NW. In each image, several NWs can be seen, they are not identical and the length can achieve over 15 μm as each step in the μ -PL is 1 μm . Considering that NWs are broken during the mechanical transference process, it is not known which side contains the InAsP layer and where it was broken. Therefore, we measured several single NWs, every one scanning along the wire to analyze the spatial distribution of the optical emission from the InAsP layer.

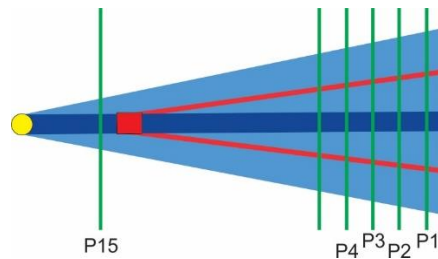


Figure 36. Schematic diagram of a single NW. The InAsP layer represented by the red color is only illustrative diagram, since the actual InAsP distribution is not known. Green solid lines represent the laser spot positions.

We used the following procedure to measure single NWs. First, we select a thick and long NW that is parallel to the X or Y direction of the translators, in order to scan along one of them, then the laser beam spot is positioned on the NW and it is focused, and optimized, following the optical image. After that, we acquire the luminescence and optimize the intensity changing the sample position, transversal and longitudinal directions (corresponding to the X and Y directions of the translators). The start position is usually at the thicker edge of the wire when it is visible. We scanned along the wire acquiring PL spectra at each 1 μm step. Figure 36 shows the illustrative diagram of a NW and the laser spot positions used here.

Due to the large acquisition time taken in each single NW, we measured only samples with large InAsP amount, i.e., above and equal 10 s of InAsP inclusion into InP, where the InAsP emission is visible with any excitation intensity. We will present firstly the first group of heterostructures (C1) and then the second ones (A2, B2 and C2).

Figures 37 shows the μ -PL spectra of four single NWs from sample C1 grown with 2 and 20 nm of Au-NPs measured at different positions along the wire with 1 μm of increment. The average spot size of the laser beam is of the order of ~ 2.5 μm diameter for 50X NIR objective. In all NWs, the PL spectra show the sharp lines around the spectral range observed in macro-PL spectra for any positions along the wire. They are attributed to the localized states created in the InAsP layer, as usually observed in QDs systems. In some NWs the D-A recombination of WZ InP (~ 1.45 eV) is also observed, mainly around the apex of the NW, where InAsP layer is absent, as shown in Fig. 36 at the position denoted by P15. Due to the lower energy of InAsP potential well than that for InP the photocreated carriers are rapidly relaxed to the well and recombine, this explains why the D-A recombination of InP is not usually observed when the sharp lines are present. Note that the same lines are observed in several consecutive spectra, because the laser beam spot size, ~ 2.5 μm , is longer than the increment size, 1 μm . Interestingly, some lines are much stronger than others, maybe they are favored by carrier transference or the cavity-like optical resonance. We have not observed any systematic change between NWs grown with 2 and 20 nm Au-NPs, therefore, the Au-NPs size dependence of the InAsP confinement effect is not clear.

Based on the growth model discussed in section 2, two regions of the InAsP layer coexist in NWs grown by VLS method, as shown in Fig. 9 or 16. One of them, denoted A, is close to the top, due to the catalyst growth of InAsP and other, denoted B, due to the lateral epitaxial growth. In the region A, since the catalyst growth rate is larger than region B, the InAsP volume

may be larger resulting lower transition energy than the region B. However, we have not observed any isolated sharp line at low energy range in all micro-PL spectra of single NWs investigated here. This suggests that the emissions from both regions are in the same range, which makes difficult to identify them. The previous works of InAsP/InP NWs show that the emission from the region A is at lower energy range than that from region B, obtaining isolated single emission as in those works [9, 10]. The discrepancy between our results and those reported in previous works can be related to the difference of the alloy composition between InAsP axial catalyst and lateral epitaxial layers. It is known that the catalyst InAsP alloy presents higher P content than lateral epitaxial growth layer, i.e., larger band gap energy for the former. In our case, it suggests that the larger gap energy and InAsP volume of the region A compensated by the smaller alloy volume of the region B, even has lower gap energy. The EDS measurements of these samples are in progress in order to address this question.

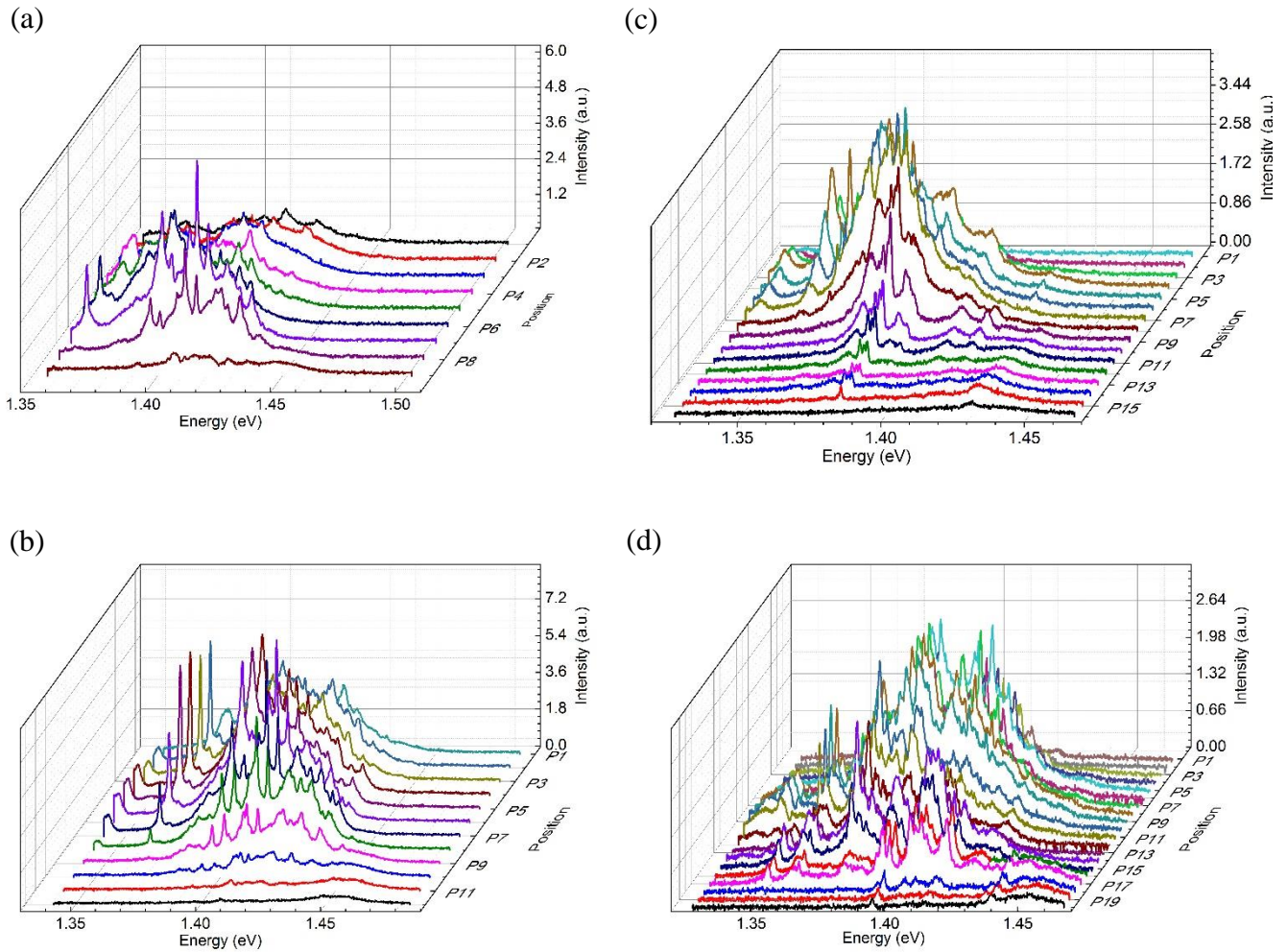


Figure 37. Spatial dependence of micro-PL spectra at 11 K and under 600 nW of excitation of four single NWs from sample C1 with Au-NPs (5 nm-2013) catalyst of (a-b) 2 nm and (c-d) 20 nm.

The μ -PL measurements of the second set of heterostructure NWs were performed in samples grown with 5 nm Au-NPs acquired in 2013. In each single NW we investigated at 3 different spectral ranges of the CCD. Figure 38 shows the typical micro-PL spectra of NWs grown with 10, 20 and 40 s of InAsP (sample A2, B2 and C2) as a function on the position along the wire. For sample A2 (Fig. 40a), the PL spectra are very similar to those shown in Fig. 37 of sample C1, since both have 10 s of InAsP, and optical emissions are only above 1.32 eV, in agreement with the ensemble PL results. For NWs of 20 s (Fig. 38b) and 40 s (Fig. 38c), as expected, the emission lines are lower energy than the A2 due to the weaker confinement effects.

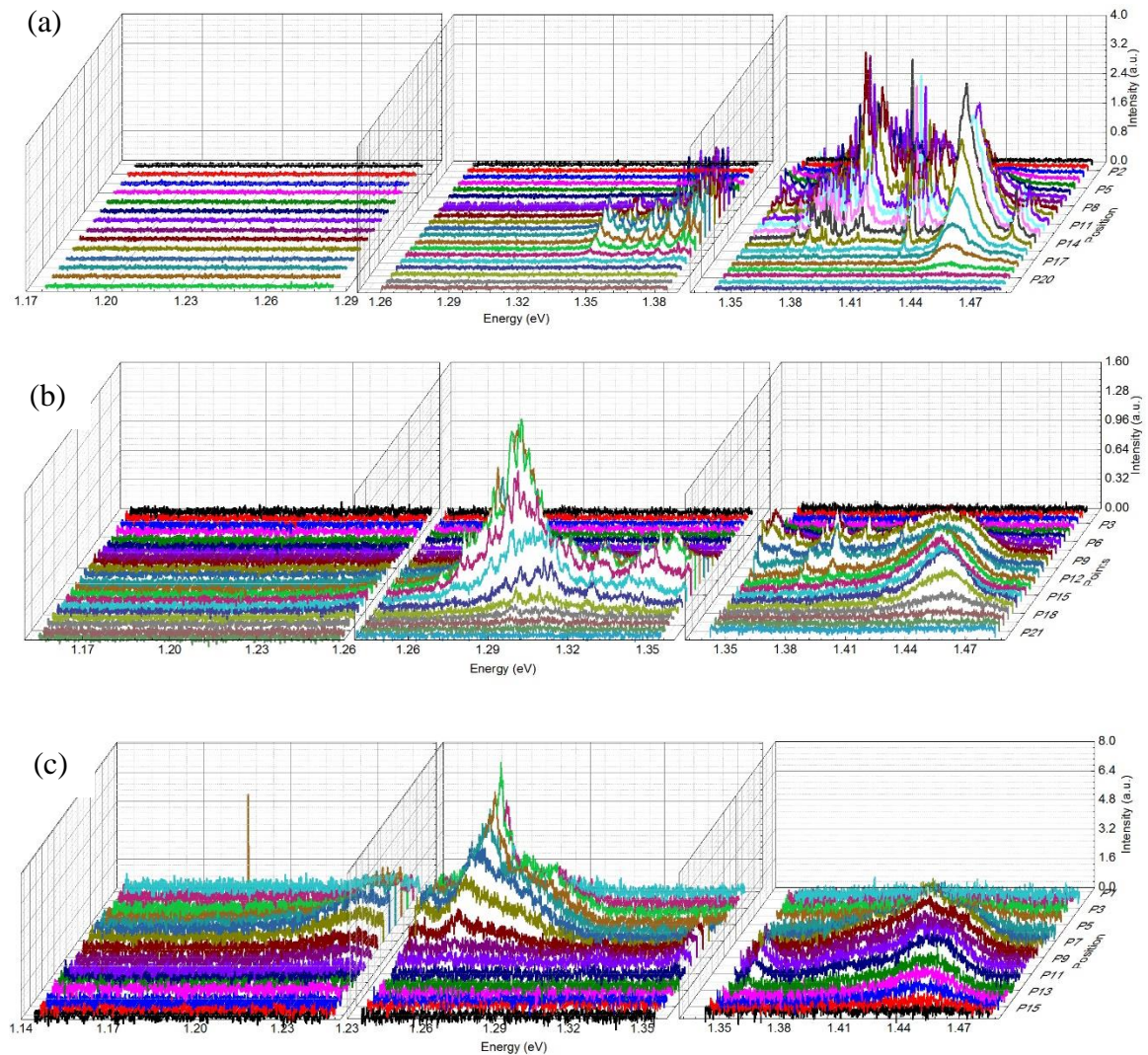


Figure 38. μ -PL spectra vs position measured of heterostructure NWs with Au-NPs catalyst of 5 nm. (a) Sample A2 at 15 K with 100 nW excitation intensity. (b) Sample B2 at 15 K with 80 nW excitation intensity. (c) Sample C2 at 11 K with 85 nW excitation intensity. The increment of the laser spot displacement is 1 μ m.

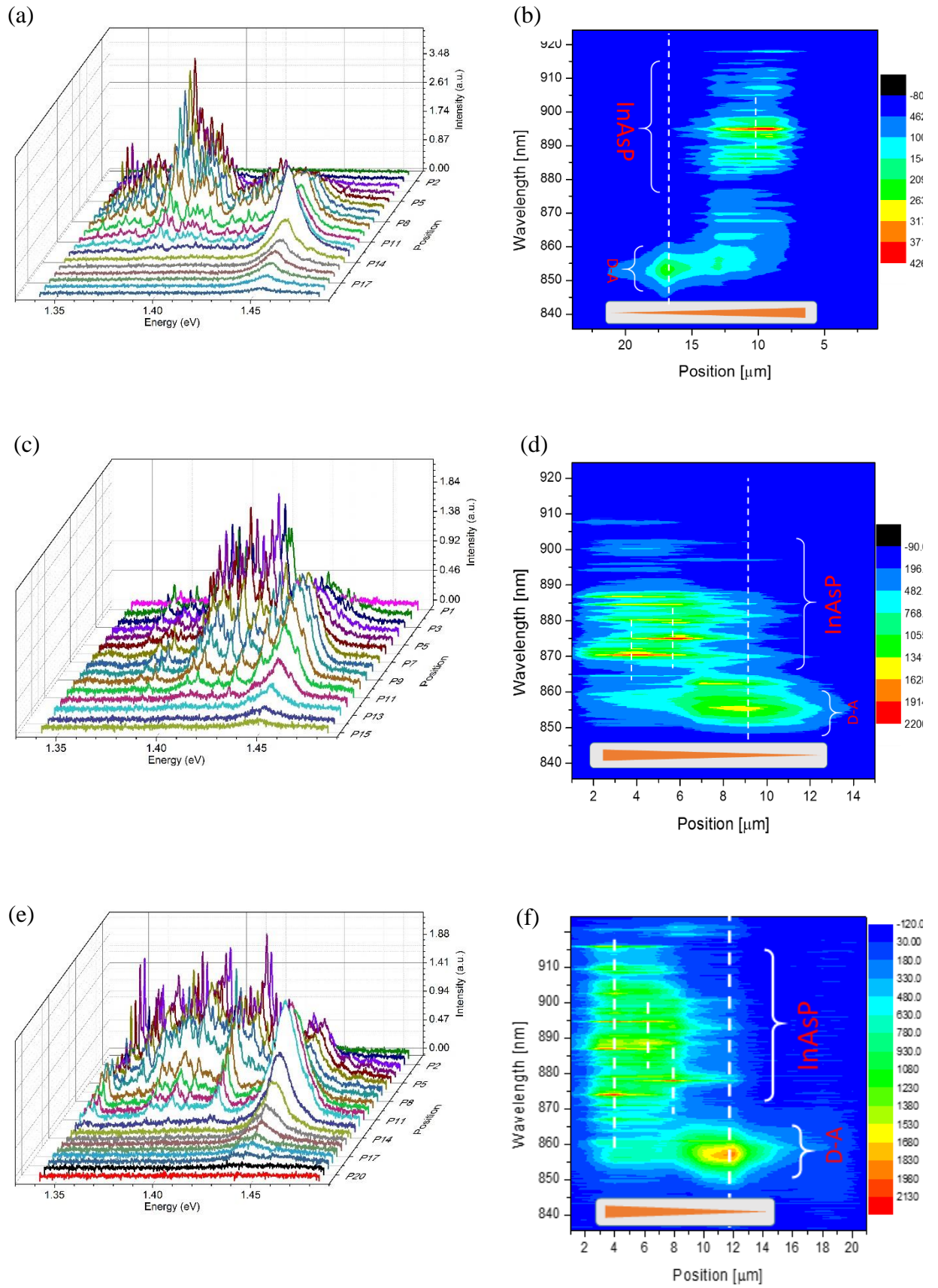


Figure 39. μ -PL spectra vs position measured at 15 K and at 80 nW of A2 (a) NW2 (c) NW3 and (d) NW 4. 2D intensity projection of (b) NW2 (d) NW3 and (f) NW4.

The D-A recombination of InP at ~ 1.448 eV is also observed and, in some cases, the sharp lines are also at the same energy of D-A band. Note that again the position where the sharp lines are dominant the D-A emission is weaker and broader, as shown in Fig. 38b. The broadening can be related to the strain effect if we consider the slight relaxation of the lattice mismatch strain the InP layer and position dependent. This strain would be tensile, decreasing the band gap energy, in agreement with the red-shift observed in fig. 38b.

In Figs. 39 – 43, we present the μ -PL spectra vs position of several NWs of samples A2, B2 and C2. Additionally, a 2D projection is presented which includes approximately the corresponding position of the NW respect to the probed PL position, their wavelength and the color scale intensity, where red tones are for higher intensities. Basically, all PL spectra of each sample present similar results and same emission energy range, indicating that the InAsP amount and the composition are very similar among the NWs, as already demonstrated by macro-PL results. The sharp lines with ≤ 0.2 meV width (same value for the system resolution) observed in all NWs are characteristic of localized state optical emissions, i.e., indication of the presence of quantum dots created likely by the roughness of InAsP layers in the region A and B of the NW, which show similar behavior of self-assembled quantum dots. A signature of the quantum dot is that the optical emissions from single and multi-exciton remain each one in the same energy independent of the number of excitons or carriers. This happens because in each optical transition of any exciton complex only a single electron-hole pair recombination occurs. In fact, when studying the PL spectra vs excitation power (not shown here) of the sharp lines, it shows the same energy as the excitation intensity increases and appears additional ones due to the exciton complexes (multi-excitons and trions). In the same time, the intensity of single exciton emission decreases, because the probability to have one exciton in a single dot reduces.

We remark that in NW3 of sample B2, in particular, only few lines are shown in the PL spectra as compared to other spectra, see Fig. 41a. This suggests that there are few quantum dots in this NW. This kind of structure can be useful for device application and appropriates for single photon emission devices. However, it only occurs in few NWs, for instance, it is one of among the 8 NWs analyzed in this work. In order to obtain NWs with few or single emission a systematic investigation of growth condition is needed.

On the other hand, it is more evident to distinguish the regions in the 2D projections shown in Fig(s). 39 – 43 where they are due to the D-A InP or the InAsP emissions. This is

indicated by red color labels InAsP and InP (corresponds to the D-A emission) in the 2D projections of Figs. 39 – 43.

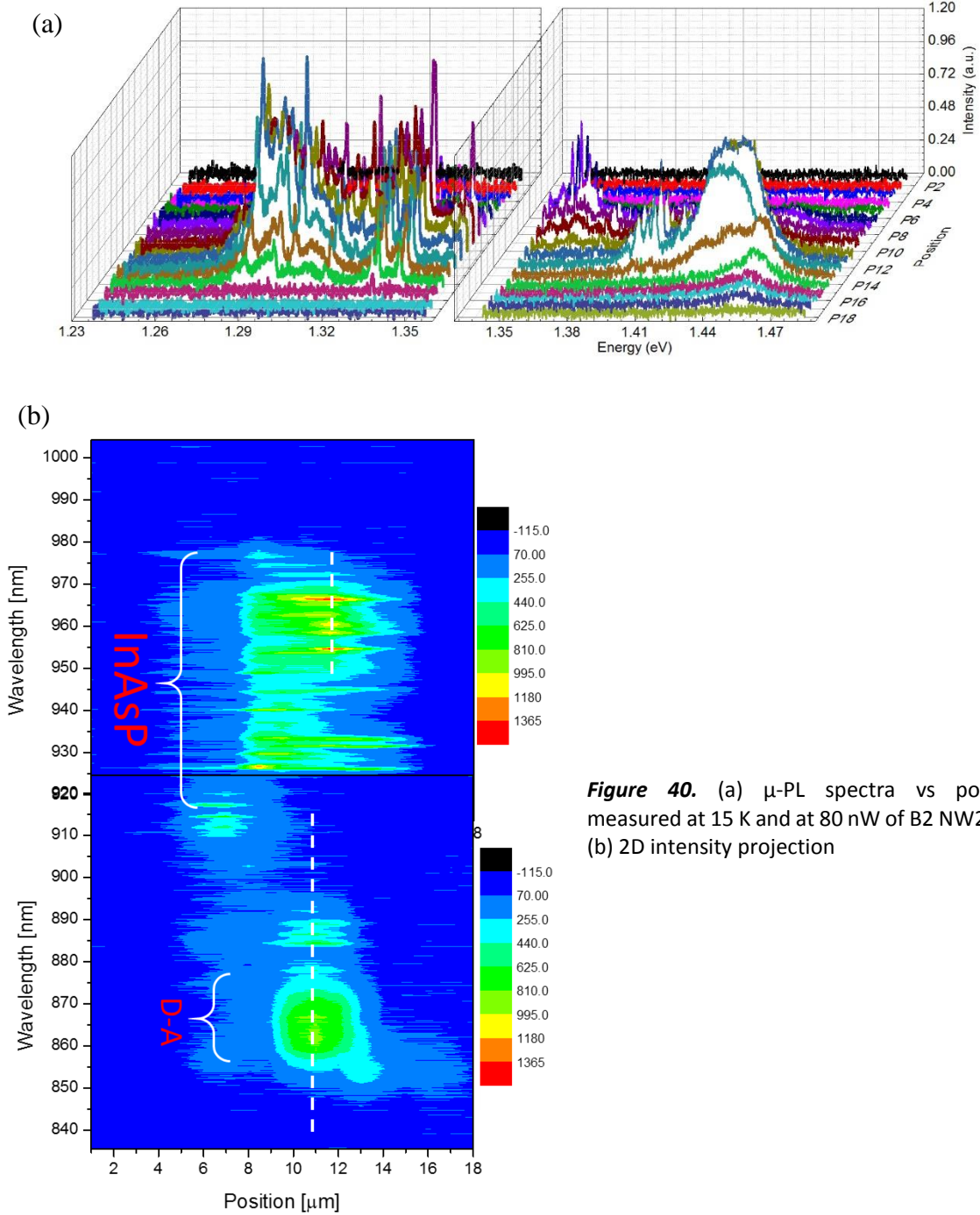
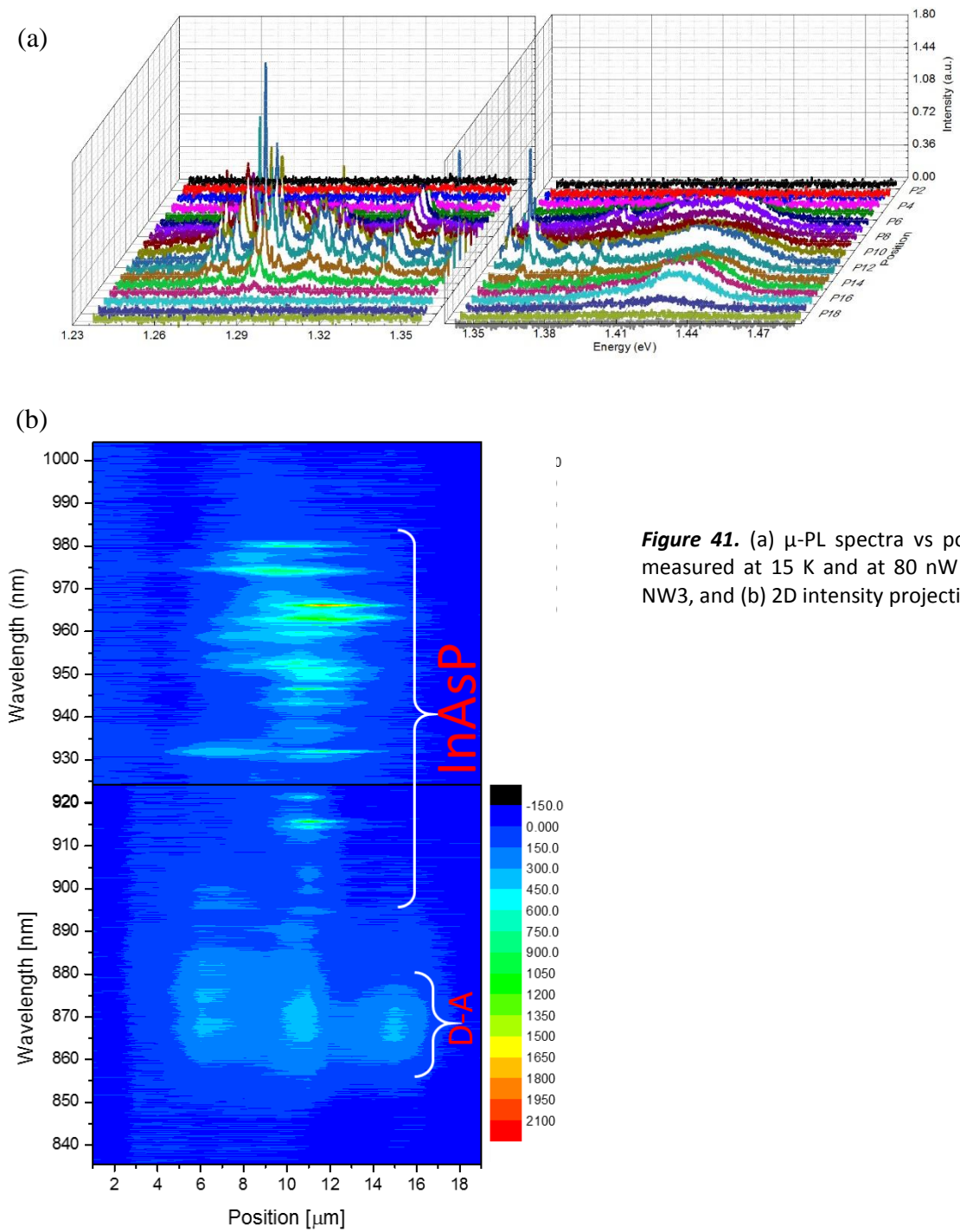


Figure 40. (a) μ -PL spectra vs position measured at 15 K and at 80 nW of B2 NW2, and (b) 2D intensity projection

For instance, in the 2D projection of Fig. 39f at the position P12 (Position 12 μ m) the emission is dominated by D-A InP, where it is broader than other sharp lines attributed to InAsP emissions, and around this spatial position the sharp lines are absent. For laser spot at the position from P12 toward the NW bottom the sharper lines start to appear below P9, which, in principle, coming from the Regions A to B, all denoted by InAsP emission. The several maxima

of these emission lines (see the vertical dashed lines, corresponding to each peaks) are at different spatial positions along the wire. This behavior is expected for region B, since the thickness of the lateral InAsP layer is randomly distributed along the wire. The main difficulty thus is to identify the emission lines corresponding to the region A. In Fig. 39f, in particular, the weak emission lines at P9 and wavelength at ~920 nm could be the emission from region A, the maximum is indeed localized close to the NW apex (close to D-A InP maximum) and above the emission line that is more right position, in the case is P8, attributed to region B. However, it is the unique case that we observe this particular condition in μ -PL measurements, where the spatial maximum of the lowest energy line is close to the D-A one. All other cases, the maximum of the lowest energy lines is at the spatial position together with other emission lines, as shown in Fig. 39.b, 39.d, 40.b, and 41.b. Therefore, in our samples in most case the emission energy from the region A is overlapped with the other emissions from the region B. In order to identify the emission from region A thus require further investigations using higher spatial resolution techniques, such as μ -PL using 100x or 200x objective or Near-Field-PL, as well as the electro-luminescence microscopy. Other alternative is to grow specific sample in a condition to increase the volume of InAsP layer of the region A and/or decrease for region B to obtain emission from region A with lower energy than that from B.

In summary, the PL spectra of NWs of InAsP alloys and InAsP/InP heterostructures grown by VLS method present high quality and show optical emissions around the near infra-red range, appropriate for telecommunication applications. The heterostructures present sharp emission lines, a typical emission from quantum dots. In contrast to the previous reported results, our optical emission from the catalyst axial InAsP quantum dot is in the same spectral range of those from the lateral InAsP layer, due to the special InAsP volume and composition of our samples. This result shows that the NWs can be improved to grow with a special condition to obtain few or single quantum dot, which can be useful for single photon sources.



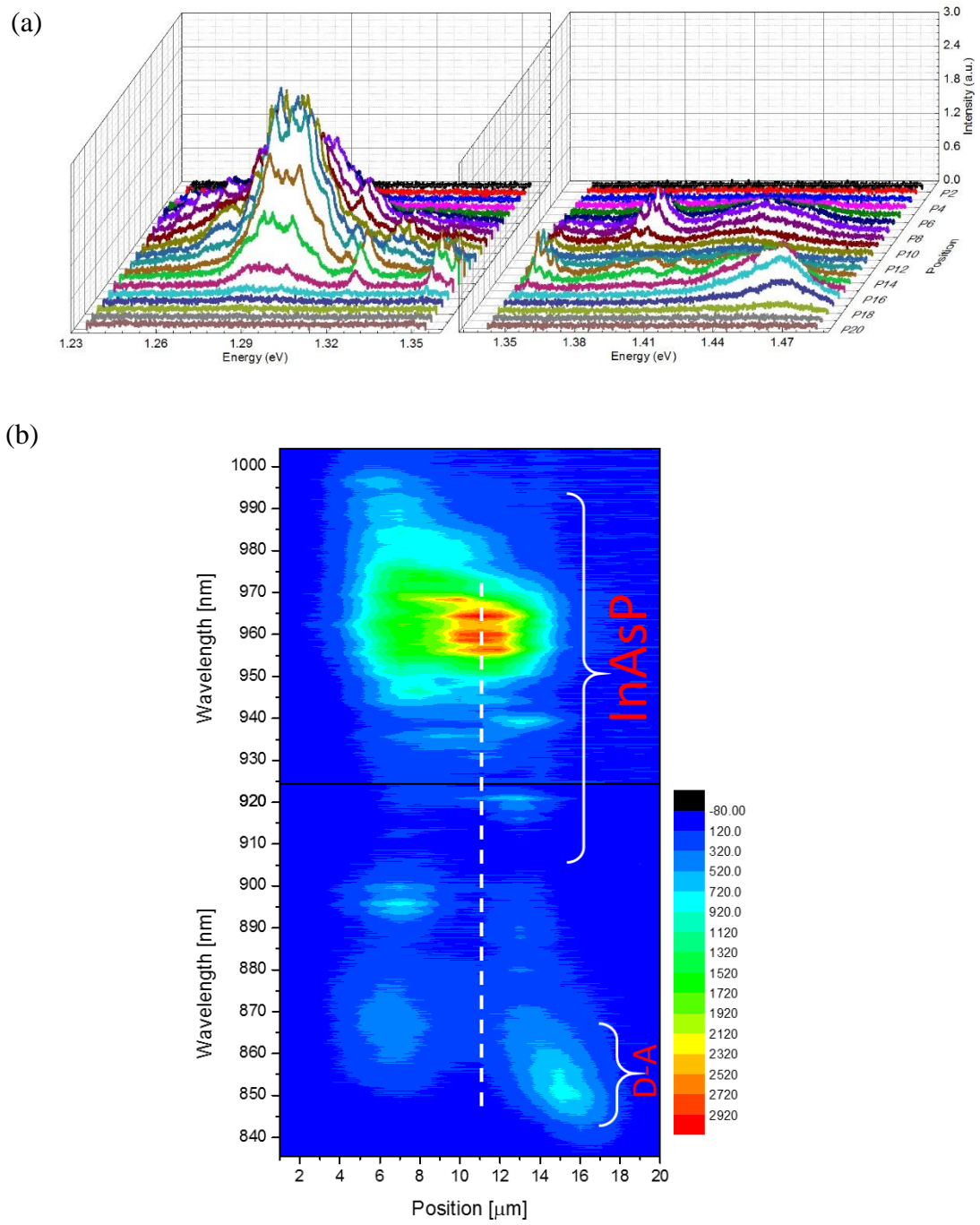


Figure 42. (a) μ -PL spectra vs position measured at 15 K and at 80 nW of C2 NW2, and (b) 2D intensity projection

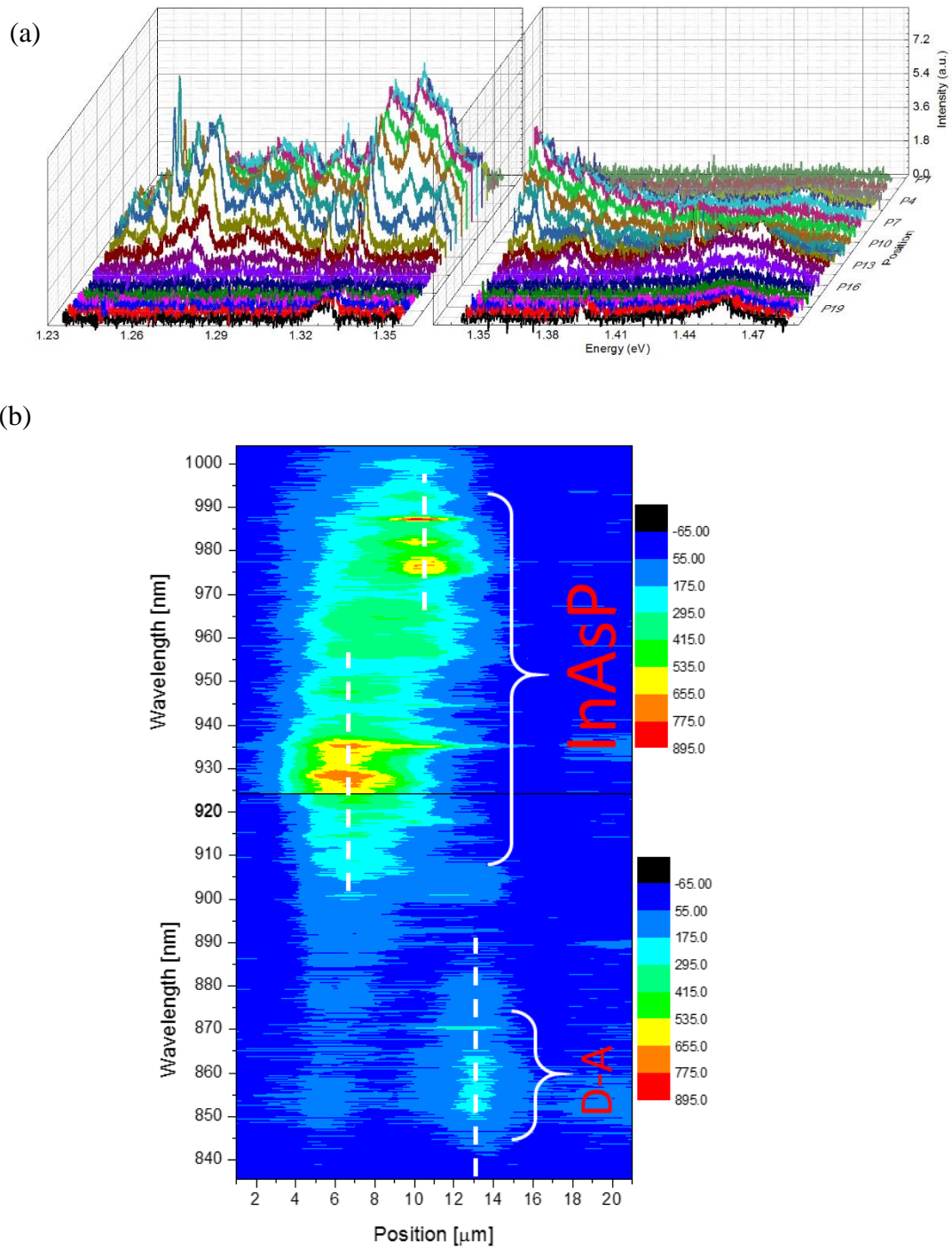


Figure 43. (a) μ -PL spectra vs position measured at 15 K and at 80 nW of C2 NW3 and (b) 2D intensity projection.

Conclusions

In this work, we present the study on the optical properties of two different NW structures in WZ phase. The first one is the InAsP alloy NWs and the second, InAsP/InP heterostructure NWs, both grown by the VLS method into a CBE system.

The photoluminescence and structural analysis of NWs with different composition of InAsP show a *P* content of around 50 %, with optical emission energy around 1.5 μm , appropriate for telecommunication devices. The NW morphology surprisingly depends on the Au-nanoparticle size, where for 2 and 5 nm NWs show tower-like shape, while, higher size, 20 nm, the usual needle-like shape.

For InAsP/InP heterostructures two set of samples were investigated. In the first set, the *InAsP* insertion time were 2, 5, and 10 s, using different Au-NPs sizes, 2, 5 and 20 nm. In the second set, the *InAsP* insertion time is longer, 10, 20 and 40 s, while the Au-NPs size was only 5 nm. The optical emission associated to InAsP layer is close to the InP gap energy, indicating thin InAsP layer and, as expected, the emission band shifts to lower energy when the amount of InAsP into InP NW increases. Analyzing single NWs, the micro-photoluminescence spectra reveal several sharp lines, an indication of strongly localized states, i.e., quantum dots created due to the roughness of the InAsP layer, perhaps similar to the self-assembled quantum dots. In our samples, the emission from two InAsP regions in the NW, from the axial catalyst InAsP layer and lateral epitaxial InAsP layer, are not distinguishable, in contrast to the reported results in previous works. The higher *P* content of the axial catalyst InAsP as compared to that lateral growth layer, i.e., higher gap energy for the former, is compensated by the smaller amount of InAsP of the lateral layer, due to its lower growth rate than catalyst growth. In order to address this point, the structural analysis, such as the size and composition distribution of InAsP layer along the wire is in progress.

One of main results of this work is that the NWs present high crystal quality and relatively strong optical emissions. This result thus motivates further investigation of InAsP/InP NWs in order to improve the heterostructure to obtain few or single optical emission from the quantum dots to tune to the optical device applications, such as, single photon source in the NIR range.

References

- [1] In-Sung Hwang, Yoon-Sung Kim, Sun-Jung Kim, Byeong-Kwon Ju, and Jong-Heun Lee, Elsevier, *Sensors and Actuators B*. **136**, 224 – 229 (2009).
- [2] Martin Heiss, Anna Dalmau-Mallorqui, and Anna Fontcuberta i Morral, SPIE Newsroom, 10.1117/2.1201307.004946 (2013).
- [3] Thelander C., Fröberg, L. E., Rehnstedt C., Samuelson L., and Wernersson L.-E., *IEEE Electron Device Lett.* **29**, 236 – 237 (2008).
- [4] Hannah J. Joyce, Qiang Gao, H. Hoe Tana, C. Jagadisha, Yong Kim, Jin Zou, Leigh M. Smith, Howard E. Jackson, Jan M. Yarrison-Rice, Patrick Parkinson, Michael B. Johnston. *Progress in Quantum Electronics*, **35**, 23 – 75 (2011).
- [5] I. Vurgaftman, J. R. Meyer, and L. R. Ram-Mohan, *Journal of Applied Physics*. **89**, 5817 – 5875, (2001).
- [6] M. Koguchi, H. Kakibayashi, M. Yasawa, K. Hiruma, and T. Katsuyama, *Jpn. J. Appl. Phys.* **31**, 2061 (1992).
- [7] Frank Glas, Jean-Christophe Harmand, and Gilles Patriarche, *Phys. Rev. Lett.* **99**, 146101 (2007).
- [8] Michele Goano, Enrico Bellotti, Enrico Ghillino, Carlo Garetto, Giovanni Ghione, and Kevin F. Brennan, *J. Appl. Phys.* **88**, 6476 (2000).
- [9] M. Tchernycheva, George E. Cirlin, Gilles Patriarche, Laurent Travers, Valery Zwiller, Umberto Perinetti, and Jean-Christophe Harmand, *Nano Lett.* Vol **7**, No. 6, 1500-1504 (2007).
- [10] Kouta Tateno, Guoqiang Zhang, Hideki Gotoh, and Tetsuomi Sogawa, *Nano Lett.* **12**, 2888 – 2893 (2012).
- [11] Kenichi Kawaguchi, Yoshiaki Nakata, Mitsuru Ekawa, Tsuyoshi Yamamoto, and Yasuhiko Arakawa, *IEEE 978-1-4673-1724-5*, 257 – 260 (2013).
- [12] V. Evoen, H. Zhou, L. Gao, M. Pozuelo, B. Liang, J. Tatebayashi, S. Kodambaka, D. L. Huffaker and R. F. Hicks, *J. Crystal Growth* **314**, 34 – 38, (2011).

-
- [13] Zwiller, V., Akopian, N., van Weert, M., van Kouwen, M. Perinetti, U. Kouwenhoven, L. Algra, R. Rivas, J. G. Bakkers, E. Patriarche, G. Liu, L. Harmand, J. –C. Kobayashi, Y. and Motohisa, J., C. R. Phys. **9**, 804. (2008).
- [14] Sköld, N., Pistol M. –E. Dick, K. A. Pryor, C. Wagner, J. B. Karlsson, and L. S. Samuelson, L. Phys. Rev. B **80**, 041312 (2009).
- [15] E. G. Gadret. G. O. Dias, L. C. O. Dacal, M. M. de Lima, Jr, C. V. R. S. Ruffo. F. Iikawa. M. J. S. P. Brasil, T. Chiaramonte. M. A. Cotta. L. H. G. Tizei, D. Ugarte, and A. Cantarero, Phys. Rev. B **82**, 125327 (2010).
- [16] E. G. Gadret, M. M. de Lima Jr., J. R. Madureira, T. Chiaramonte, M. A. Cotta, F. Iikawa, and A. Cantarero, Appl. Phys. Lett. **102**, 122101 (2013).
- [17] M. Moller, M. M. De Lima Jr., A. Cantarero, T. Chiaramonte, M. A. Cotta and F. Iikawa, Nanotechnology **23**, 375704 (2012).
- [18] M. Möller, M. M. de Lima, Jr., A. Cantarero, L. C. O. Dacal, J. R. Madureira, F. Iikawa, T. Chiaramonte, and M. A. Cotta, Phys. Rev. B **84**, 085318 (2011).
- [19] R.S. Wagner and W.C. Ellis, App. Phys. Lett. **4**, 88 – 90 (1964).
- [20] W. T. Tsang, App. Phys. Lett. **45** (11), 1234 – 1236 (1984).
- [21] A. Y. Cho and J. R. Arthur, Progress in Solid-State Chemistry **10**, 157 – 191, (1975).
- [22] Linda M. Miller and James J. Coleman, Critical Reviews in Solid State and Material Science **15**, 1, 1 – 26 (1988).
- [23] Harald Ibach and Hans Lüth, “Solid-State Physics, An Introduction To Principles of Materials Science”, Fourth Edition, Springer ISBN 978-3-540-93803-3, (2009).
- [24] A. De and Craig E. Pryor, Phys. Rev. B **81**, 155210, (2010).
- [25] Luis C. O. Dacal, and A. Cantanero, Journal of Nanophotonics, 071598 (2013).
- [26] David A. B. Miller, Rm. 4B-401, AT&T Bell Laboratories, Holmdel NJ07733-3030, (2003).
- [27] P. J. P. Tang, M. J. Pullin, and C. C. Phillips, Phys. Rev. B **55**, 4376 – 4382 (1997).
- [28] Y. P. Varshni, *Physica* **34**, 149 – 154 (1967).

-
- [29] N. M. Ravindra and V. K. Srivastava, *J. Phys. Chem. Solids* **40**, 791 – 793 (1979).
- [30] Z. M. Fang, K. Y. Ma, D. H. Jaw, R. M. Cohen, and G. B. Stringfellow, *J. Appl. Phys.* **67** (1990).
- [31] Sun Y., Thompson S., and Nishida T. Springer 978-1-4419-0551-2 (2010).
- [32] W. Q. Chen and S. K. Hark, *J. Appl. Phys.*, **77**, 5747 (1995).
- [33] C. Hajlaoui, L. Pedesseau, F. Raoua, F. B. Cheikhlarbi, J. Even, and J.-C, Jancu. *J. of Phys. D.: Appl. Phys.* **46**, (2013).
- [34] Mark Fox, “Optical Properties of Solids”, Oxford University Press ISBC 0 19 850612 0, Ch. 3 & 5, (2001).
- [35] Gerald Bastard, “Wave Mechanics applied to semiconductor heterostructures”, Les Editions de Physique, 66 – 69, (1988).
- [36] J. Trägårdh, A. I. Persson, J. B. Wagner, D. Hessman, and L. Samuelson, *J. Appl. Phys.* **101**, 123701 (2007).
- [37] S. Sanguinetti, M. Henini, M. Grassi Alessi, M. Capizzi, P. Frigeri, and S. Franchi, *Phys Ver B*, Vol **60**, No 11, 8276-8283 (1999).
- [38] O. Rubel, M. Galluppi, S.D. Baranovskii and K. Volz, L. Geelhar and H. Riechert, P. Thomas and W. Stolz, *J. Appl. Phys.* **98**, 063518 (2005).
- [39] Ibach Luth, “Solid State Physics, An introduction to Principles of Material Science”, Springer, Ch. 12, (2009).
- [40] J. Johansson, C. Patrik T. S., T. Martensson, L. Samuelson and W. Seifert, *J. Phys. Chem. B*, 109, 13567 – 13571 (2005).
- [41] I. V. Bodnar, A. I. Lukomskii, and G. F. Smirnova, *Phys. Stat. Sol. A* 37, K137 - 176 (1976).
- [42] R. L. Moon, G. A. Antypas, and L. W. James. *J. of Elec. Mat.* **3**, 635 – 643 (1974).
- [43] “Indium Phosphide and Related Materials”. Boston: Artech Hous (1992).